Imperfection Insensitive Thin Shells

Thesis by

Xin Ning

In Partial Fulfillment of the Requirements

for the Degree of

Doctor of Philosophy

California Institute of Technology

Pasadena, California

2015

(Defended May 5, 2015)

Acknowledgements

Studies of imperfection-sensitivity of thin-shell structures were pioneered by many researchers in GALCIT, including Theodore von Kármán and Hsue-Shen Tsien, who went back to China in the 1950s and became the father of the Chinese space program. The work presented in this thesis was built upon the shoulders of these giants. It has been a great honor for me to pursue a PhD in Aeronautics at Caltech.

First and foremost, I would like to express my deepest gratitude to my advisor, Professor Sergio Pellegrino, who gave me the opportunity to study in GALCIT and led me into the fascinating world of thin-shell structures. The work presented in this thesis would not have been possible without his vision, guidance, support, and encouragement. I am especially impressed by his sharp mind for simplifying a complex problem and solving it in an intuitive, elegant, and very effective way. I am particularly grateful for the huge efforts he spent on teaching us how to make excellent presentations. I have learned so much from him in the past six years, and I am sure I will forever benefit from his guidance during my PhD studies.

I am grateful for the valuable comments and suggestions from the members of my thesis committee: Professors Jim Beck, Dennis Kochmann, and Guruswami Ravichandran. I also thank Professors Ekkehard Ramm, Martin M. Mikulas, John Hutchinson, Jean-François Jullien, Petros Koumoutsakos, Chris Calladine, Paolo Ermanni, Kwang-Chun Park, Tony Waas, Paul Weaver, Katia Bertoldi, and Ryan Elliot for help and advice during the course of this study. In addition, I would like to extend my gratitude to Ted Nye and Tim Shinbara for inspiring my first research project. I thank Professor José Andrade and Ryan Hurley for their help with the high-speed camera.

I would like to thank my current and former colleagues at the Space Structures Laboratory for their constructive and helpful suggestions, comments, and discussions. My gratitude goes to Manan Arya, Melanie Delapierre, Kristina Hogstrom, Maria Sakovsky, John Steeves, Yuchen Wei, Lee Wilson, Dr. Stephen Bongiorno, Dr. Federico Bosi, Dr. Kathryn Jackson, Dr. Nicolas Lee, Dr. Ignacio Maqueda Jiménez, Dr. Keith Patterson, and Markus Schatz. I also need to particularly thank Dr. Xiaowei Deng, Dr. Francisco López Jiménez, Dr. Kawai Kwok, and Dr. Chinthaka Mallikarachchi for their help and mentorship during my first few years at Caltech.

I am thankful to Petros Arakelian for his assistance in my experimental setups. I would like to acknowledge GALCIT staff: Joe Haggerty, Kathleen Jackson, Christine Ramirez, Dimity Nelson, and Cheryl Gause for their help during the past few years. I thank Dr. Jackie Gish for her advice on my career development.

I would like to express my appreciation to the Resnick Sustainability Institute at Caltech for providing me with a graduate fellowship. The financial support for my first research project from the Northrop Grumman Aerospace Systems is also gratefully acknowledged.

I am grateful to all my friends and classmates at Caltech who have made my life much easier. They are always there to help me with any difficulties and we have shared many memorable moments together.

Finally, but most importantly, I would like to thank my parents and grandparents, who always encouraged me to pursue my dreams and supported all my decisions. Their unconditional support and love have enabled me to reach this point and will be my wealth for a lifetime.

Abstract

The buckling of axially compressed cylindrical shells and externally pressurized spherical shells is extremely sensitive to even very small geometric imperfections. In practice this issue is addressed by either using overly conservative knockdown factors, while keeping perfect axial or spherical symmetry, or adding closely and equally spaced stiffeners on shell surface. The influence of imperfection-sensitivity is mitigated, but the shells designed from these approaches are either too heavy or very expensive and are still sensitive to imperfections. Despite their drawbacks, these approaches have been used for more than half a century.

This thesis proposes a novel method to design imperfection-insensitive cylindrical shells subject to axial compression. Instead of following the classical paths, focused on axially symmetric or high-order rotationally symmetric cross-sections, the method in this thesis adopts optimal symmetry-breaking wavy cross-sections (wavy shells). The avoidance of imperfection sensitivity is achieved by searching with an evolutionary algorithm for smooth cross-sectional shapes that maximize the minimum among the buckling loads of geometrically perfect and imperfect wavy shells. It is found that the shells designed through this approach can achieve higher critical stresses and knockdown factors than any previously known monocoque cylindrical shells. It is also found that these shells have superior mass efficiency to almost all previously reported stiffened shells.

Experimental studies on a design of composite wavy shell obtained through the proposed method are presented in this thesis. A method of making composite wavy shells and a photogrametry technique of measuring full-field geometric imperfections have been developed. Numerical predictions based on the measured geometric imperfections match remarkably well with the experiments. Experimental results confirm that the wavy shells are not sensitive to imperfections and can carry axial compression with superior mass efficiency.

An efficient computational method for the buckling analysis of corrugated and stiffened cylindrical shells subject to axial compression has been developed in this thesis. This method modifies the traditional Bloch wave method based on the stiffness matrix method of rotationally periodic structures. A highly efficient algorithm has been developed to implement the modified Bloch wave method. This method is applied in buckling analyses of a series of corrugated composite cylindrical shells and a large-scale orthogonally stiffened aluminum cylindrical shell. Numerical examples show that the modified Bloch wave method can achieve very high accuracy and require much less computational time than linear and nonlinear analyses of detailed full finite element models.

This thesis presents parametric studies on a series of externally pressurized pseudo-spherical shells, i.e., polyhedral shells, including icosahedron, geodesic shells, and triambic icosahedra. Several optimization methods have been developed to further improve the performance of pseudo-spherical shells under external pressure. It has been shown that the buckling pressures of the shell designs obtained from the optimizations are much higher than the spherical shells and not sensitive to imperfections.

Contents

List of Figures

List of Tables

Chapter 1

Introduction

1.1 Overview

Cylindrical shells have been widely used over decades in many engineering fields such as civil, oil, marine, and aerospace industries, etc. For example, storage tanks, as shown in Fig. 1.1 (a), are the most commonly seen cylindrical shells, and cylindrical pipelines are key structural components in oil and natural gas industry. Due to the lightness and high load-carrying capability of cylindrical shells, they have been extensively used as aerospace structures such as airplane fuselages and rocket shells, as shown in Fig. 1.1 (b) and (c).

Figure 1.1: (a) Water storage tank (image credit: CST Industry). (b) Boeing 787 composite fuselage. (c) Space Shuttle Atlantis (image credit: NASA/KSC).

Spherical shells also have very wide structural applications in engineering. For example, spherical shells can be used as storage tanks, as seen in Fig. 1.2 (a); the spherical submarine in Fig. 1.2 (b) is a typical example of spherical shells under hydrostatic pressure. A portion of a complete spherical shell, i.e., spherical cap, is also often used. The most common applications of spherical caps are concrete roofs such as the roof of the Kresge Auditorium in Fig. 1.2 (c).

Cylindrical and spherical shells are often subject to destabilizing loads such as axial compression, bending, torsion, and external pressure. In order to achieve high mass efficiency, cylindrical and spherical shells are very thin compared to their overall structural dimensions (e.g., radius, length, and span). Therefore, buckling

Figure 1.2: (a) Spherical storage tanks (image credit: BBB Tank Services). (b) Triton submarines (image credit: Sandra Edwards/South Florida Dive Journal). (c) MIT Kresge Auditorium (from Wikipedia). Its concrete roof is one-eighth of a complete sphere.

is an important and sometimes critical consideration in designing thin cylindrical and spherical shells.

Among the destabilizing loading conditions, axial compression for cylindrical shells and external pressure for spherical shells are the most destructive ones because their buckling is extremely sensitive to geometric imperfections. Typical examples of axially compressed cylindrical shells and externally pressurized spherical shells are rocket shells under self-weight and submarine pressure hulls under hydrostatic pressure, respectively. A small geometric imperfection can drastically reduce the buckling loads of those shells, significantly impairing their mass efficiency in carrying loads. This extreme imperfection-sensitivity has been one of the major obstacles in designing axially compressed cylindrical shells and externally pressurized spherical shells.

1.1.1 Axially Compressed Cylindrical Shells

Motivated by the development of aerospace industry, axially compressed cylindrical shells have been extensively studied since the space age. Large discrepancies between theoretically predicted and experimentally measured buckling loads for axially loaded cylindrical shells were first observed in the 1930s. It was found that thin cylindrical shells under axial compression may buckle at loads as low as only 20% of the theoretically predicted buckling loads (Brush and Almroth, 1975). It was subsequently established in the 1940s that this disagreement between theories and experiments is due to the extreme imperfection-sensitivity of buckling of cylindrical shells under axial compression.

In practice an empirical lower bound of knockdown factors is used to consider the reduction in buckling loads of axially compressed cylindrical shells due to imperfections (Jones, 2006). Cylindrical shells are designed for much larger theoretical buckling loads to ensure that, when the knockdown factor is applied, they still meet their design requirements. The empirical lower bound on the knockdown factors was derived from many tests conducted over 50 years ago, and it is still currently used to design axially loaded cylindrical shells. It has been argued that the knockdown-factor method cannot provide a rational basis for modern designs and tends to produce overly conservative and heavy shells (Jones, 2006; Nemeth and Starnes, 1998). NASA Langley is currently developing new knockdown factors for the Space Launch System by performing subscale and full-scale buckling tests (Hilburger, 2012; Hilburger et al., 2012b).

Closely stiffened cylindrical shells, shells reinforced by stringers, corrugations, and rings, as shown in Fig. 1.3, are used to mitigate the severe imperfection-sensitivity. It has been found that the knockdown factors of closely stiffened shells could be between 0.7 and 0.95, indicating a much lower imperfection-sensitivity than unstiffened monocoque cylindrical shells (Card and Jones, 1966). This architecture is currently established as the premiere efficient aerospace structure (Singer et al., 2002b). However, stiffened shells are still sensitive to imperfections, although the sensitivity is not as extreme as monocoque cylindrical shells. It should also be noted that the stiffened cylindrical shells are very expensive due to their complex manufacturing processes.

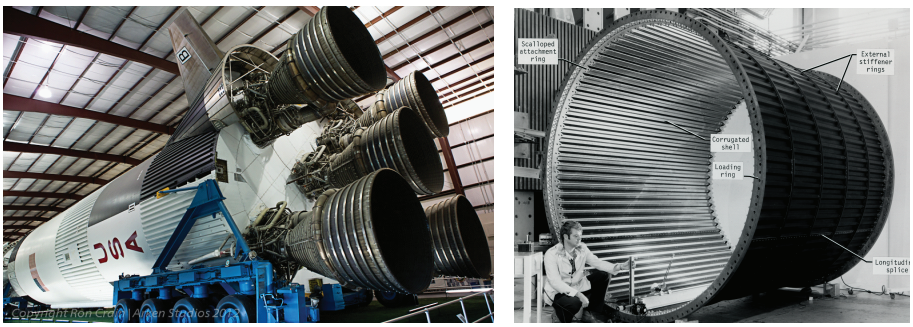

Figure 1.3: (a) Saturn V. (image credit: Ron Crain). (b) A corrugated graphite-epoxy ring-stiffened cylindrical shell (Davis, 1982).

1.1.2 Externally Pressurized Spherical Shells

The buckling behavior of spherical shells under external pressure has been extensively investigated since the 1960s. Both theoretical and experimental studies have confirmed the severe imperfection-sensitivity of externally pressurized spherical shells. The analytical predictions obtained by Hutchinson (1967) and Koga and Hoff (1969) showed that an imperfection with amplitude of half shell thickness could drastically reduce the buckling pressure by 50% to 60%. The experiments performed by Krenzke (1962) showed that the measured buckling pressure could reach only 50% to 70% of the predicted values of perfect spherical shells.

Empirical knockdown factors are used in practice to design spherical shells under external pressure; see references NASA-SP-8032 (1969) for spherical caps and Krenzke and Kiernan (1963) for complete spherical shells. Similar to the knockdown-factor method of cylindrical shells, using the empirical knockdown factors of spherical shells leads to overly conservative and heavy shells which are still very sensitive to imperfections (Nemeth and Starnes, 1998).

Stiffened spherical shells are less commonly used in engineering than stiffened cylindrical shells, and investigations on externally pressurized stiffened spherical shells, especially on complete stiffened spherical shells, are very scarce and hardly available (Singer et al., 2002b; Ventsel and Krauthammer, 2001). Krenzke and Kiernan (1963) performed experimental studies on stiffened hemispherical shells and concluded that stiffening could not be effective unless the stiffeners are closely spaced and in both circumferential and meridional

directions. The analytical and numerical studies by Öry et al. (2002) showed that stiffened spherical shells under hydrostatic pressure could still be rather sensitive to imperfections. Therefore, considerable theoretical and experimental studies are required in order to find the efficient stiffening configurations.

1.2 Objective and Scope

The two main methods of designing axially compressed cylindrical shells and externally pressurized spherical shells have drawbacks. First, the knockdown-factor method essentially provides conservative safety factors without changing the behavior of shell buckling. Second, although stiffening cylindrical shells by equally spaced stringers, rings, and corrugations can mitigate the imperfection-sensitivity, stiffened cylindrical shells are still sensitive to imperfections and are very expensive. In addition, the effects of stiffening spherical shells are not clear.

The objective of this dissertation is to propose novel methods of designing imperfection-insensitive axially compressed cylindrical shells and externally pressurized spherical shells that have high load-carrying capability. Conventional cylindrical and spherical shells have axial symmetry, high-order rotational symmetry, or spherical symmetry. The methods proposed in this dissertation use structural optimization to search for optimal symmetry-breaking shapes that maximize the critical buckling loads and at the same time reduce imperfection-sensitivity. The behavior of the novel symmetry-breaking shells designed through the proposed methods is fundamentally different from the highly symmetric shells obtained from the knockdown-factor method and stiffening method.

This dissertation is mainly focused on axially compressed cylindrical shells. The method of designing imperfection-insensitive axially compressed cylindrical shells was first developed and then used to produce several composite and metal shells. Experimental studies were preformed on a design of composite shell in order to validate the method. A fast computational method for buckling analysis of axially loaded stiffened/corrugated cylindrical shells was developed, and could be potentially used to reduce the computational costs of optimization. The idea of breaking symmetry was then applied in designing imperfection-insensitive metal spherical shells under external pressure. All the shells presented in this dissertation were assumed to be linearly elastic.

1.3 Layout of Dissertation

This dissertation consists of seven chapters. After this introductory chapter, Chapter 2 presents brief reviews on the essential background to the current study. The first part of the chapter focuses on axially compressed cylindrical shells, including the theories for buckling of cylindrical shells, details of current design methods, mass efficiency, manufacturing and testing methods, and current methods for analyzing buckling of stiffened/corrugated shells. The second part of the chapter reviews the theoretical and experimental studies of

externally pressurized spherical shells.

Chapter 3 first describes a method for obtaining imperfection-insensitive axially loaded cylindrical shells. Several symmetry-breaking shells (wavy shells) designed through the method are then presented. The results are then analyzed and compared to other alternative shells, including sinusoidally corrugated shells and Aster shell. The mass efficiency of wavy shells is then calculated and compared to currently existing stiffened shells.

Chapter 4 presents experimental studies of the best composite wavy shell obtained in Chapter 3. The chapter begins with a method of making composite wavy shells. A novel method of measuring full-field geometric imperfections is then presented. Based on measured imperfections, the experimental behavior of the wavy shells is predicted. The last part of the chapter shows the measured experimental behavior of the wavy shells.

Chapter 5 presents a highly efficient computational tool for predicting the onset of buckling of corrugated or stiffened cylindrical shells under axial compression. The computational tool is a modification of the traditional Bloch wave method for two or three dimensional infinite structures. The chapter first explains how the Bloch wave method is modified for corrugated and stiffened cylindrical shells. The numerical implementation of the modified method, including the finite element implementation and algorithm, is then described. Several numerical examples are then analyzed to validate the modified Bloch wave method. The results and computational time of the modified Bloch wave method are then compared to linear and nonlinear finite element analyses based on full detailed finite element models.

Chapter 6 presents parametric studies on several pseudo-spherical shells, i.e., polyhedral shells. Several optimization methods of design imperfection-insensitive pseudo-spherical shells under external pressure are then described. Chapter 7 concludes the dissertation.

Chapter 2

Background and Literature Review

This chapter consists of two parts: literature reviews of axially compressed cylindrical shells and externally pressurized spherical shells. There is a huge body of literature on the buckling of linear-elastic thin cylindrical and spherical shells. This chapter is focused on the essential background to the present study. The interested reader is referred to the extensive reviews compiled by Brush and Almroth (1975), Elishakoff (2012), Hutchinson and Koiter (1970), Jones (2006), Singer et al. (2002a), Singer et al. (2002b), and Bushnell (1985).

2.1 Reviews of Axially Compressed Cylindrical Shells

2.1.1 Theories and Design Methods

2.1.1.1 Effects of Imperfections on Cylindrical Shells

The first major contribution to the present understanding of the effects of initial imperfections on the buckling of circular cylindrical shells was made by Von Kármán and Tsien (1941), who analyzed the postbuckling equilibrium of axially compressed cylindrical shells. Donnell and Wan (1950) analyzed initially imperfect cylindrical shells and obtained equilibrium paths as sketched by the dash line in Fig. 2.1, where P and P_{cl} are the compressive load and the classical bifurcation buckling load, respectively. Figure 2.1 shows a sharply dropping second equilibrium path and thus indicates that an initially imperfect shell buckles at the limit point B instead of reaching the bifurcation point A. Koiter (1963) analyzed the influence of axisymmetric imperfections coinciding with the axisymmetric buckling mode of a perfect cylindrical shell. His results, summarized in Fig. 2.2, show that imperfections with even a small amplitude can dramatically reduce the buckling load.

A more general analysis of the influence of initial imperfections (Koiter, 1945) was based on an analysis of the potential energy of the loaded structure in a general buckled equilibrium configuration. This analysis is applicable to asymmetric imperfections and shells of arbitrary shape (Brush and Almroth, 1975), and provides an approximate solution to the secondary equilibrium path for a perfect structure, with a single

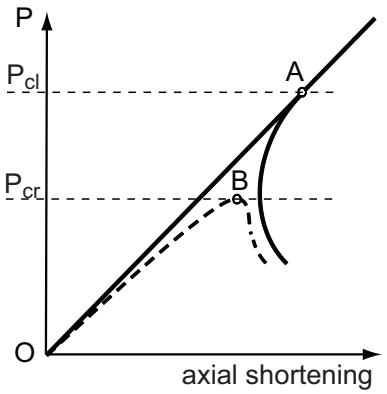

Figure 2.1: Sketch of equilibrium paths for axially compressed, geometrically perfect cylindrical shells (solid line, from Von Kármán and Tsien (1941)) and imperfect cylindrical shells (dash line, from Donnell and Wan (1950)).

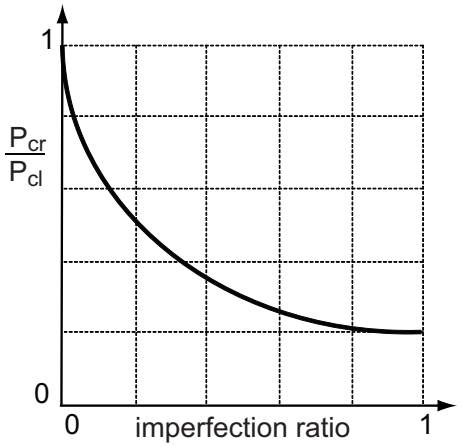

Figure 2.2: Sketch of influence of imperfection amplitude (ratio of imperfection amplitude to shell thickness) on buckling load P_{cr} of imperfect shells, based on Koiter (1963).

buckling mode associated with the first bifurcation point:

$$\lambda_0 \equiv \frac{P}{P_{cl}} = 1 + a_1\delta + a_2\delta^2 + ..., \tag{2.1}$$

where a_1, a_2, ... are constants and δ is a measure of the lateral displacement amplitude. This solution is shown by means of solid lines in Fig. 2.3. In case I $a_1 \neq 0$ and for small values of δ the secondary equilibrium path is approximated by a straight line. For the other two cases $a_1 = 0$, resulting in quadratic secondary equilibrium paths: $a_2 < 0$ for case II and $a_2 > 0$ for case III.

The corresponding equilibrium paths for imperfect structures are shown by dash lines in the figure. $\lambda_\pm$ are ratios between the buckling loads of imperfect structures with positive/negative imperfections and the perfect structure. Cases I and II represent structures that are *sensitive to imperfections*, because the buckling loads of the imperfect structures (λ_- for case I and $\lambda_\pm$ for case II) are lower than 1. In case I different signs of imperfections lead to different types of imperfection-sensitivity.

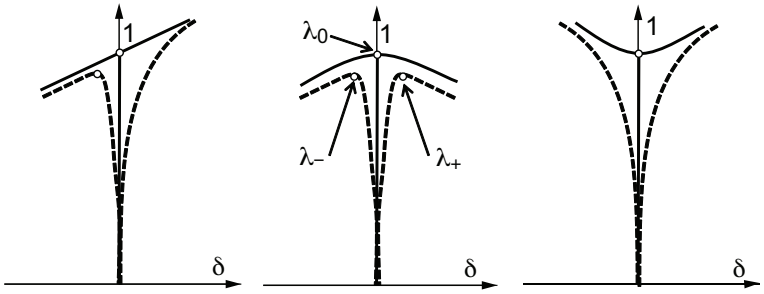

Figure 2.3: Three types of post-buckling equilibrium paths for perfect and imperfect structures, from Brush and Almroth (1975) and Koiter (1945).

2.1.1.2 Design of Cylindrical Shells Against Buckling

The current approach for the design of axially compressed monocoque cylindrical shells against buckling accounts for buckling load reductions due to imperfections through the *knockdown-factor method*. The actual buckling load of a cylindrical shell is estimated from:

$$P_{cr} = \gamma P_{cl} \tag{2.2}$$

where γ is the knockdown factor and P_{cl} is given by (Brush and Almroth, 1975):

$$P_{cl} = \frac{2\pi E t^2}{\sqrt{3(1-\nu^2)}}, \tag{2.3}$$

where E, ν, and t are the Young's modulus, Poisson's ratio, and shell thickness, respectively.

A widely used expression for γ is the empirical curve provided in NASA SP-8007 (Peterson et al., 1965) and shown in Fig. 2.4. Given a radius to thickness ratio R/t, this curve provides a lower bound to a large

dataset of experimentally derived knockdown factors and hence can be used to predict the buckling load using Eq. 2.2.

Designs obtained from the knockdown factor method are required to achieve a theoretical buckling load P_{cl} high enough that the reduced buckling load P_{cr} obtained from Eq. 2.2 satisfies the design requirements. Fundamentally, the knockdown-factor design method accepts highly imperfection-sensitive shell designs, but limits the maximum load that can be applied to keep them safe.

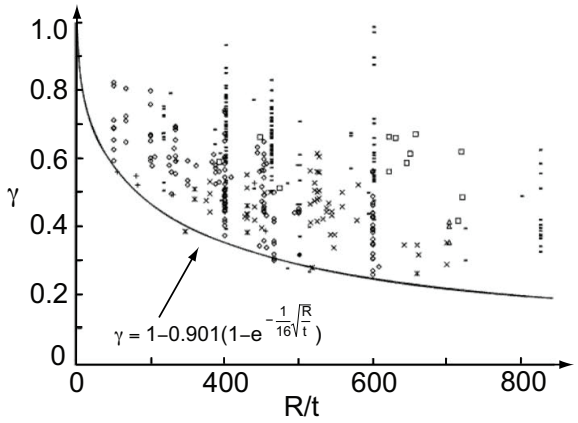

Figure 2.4: Experimentally measured values of knockdown factor and empirically defined lower bound curve, as a function of the radius to thickness ratio (Jones, 2006).

An alternative structural form to the imperfection-sensitive monocoque cylinder is the *stiffened* cylindrical shell. Although it is difficult to make a general comparison, as there are many different potential configurations for the stiffeners, as an example it can be noted that experiments on 12 longitudinally stiffened cylindrical shells with internal or external, integral or Z-stiffeners provided knockdown factors in the range 0.7 to 0.95, indicating a much lower imperfection-sensitivity than monocoque cylindrical shells (Card and Jones, 1966).

2.1.1.3 Manufacturing Imperfection Signature Method

The empirically derived lower bound on the knockdown factor in Fig. 2.4 was derived from many tests conducted over a long period of time and recently it has been argued that the manufacturing, loading, and boundary conditions for this large set of shells are not sufficiently well-known to provide a rational basis for modern design. Also, most data points correspond to metallic shells, whereas fiber-reinforced composite shells are not well represented (Jones, 2006; Nemeth and Starnes, 1998). Hence, it has been argued by several authors that the knockdown-factor approach tends to provide overly conservative designs because it allows for the worst possible imperfections, which is not a reasonable assumption for modern, precision-made shells.

An emerging alternative design approach is based on the "signature" of the manufacturing imperfection, which is a statistical representation of geometric imperfections based on measurements (Rotter et al., 1992; Teng, 1996; Hilburger and Starnes Jr, 2001; Hilburger et al., 2006; Jones, 2006). This imperfection signature

is then applied in the analysis to accurately predict the actual buckling load. Hilburger et al. (2006) obtained the buckling loads of six graphite-epoxy cylindrical shells subject to combined axial compression and torsion by using five imperfection shapes, including the actual measured imperfections of test specimens, mean imperfection shape, mean imperfection shape plus or minus one standard deviation, and the critical-buckling-mode imperfection shape. The predicted and measured buckling loads of a composite shell with an axially-stiff laminate $[\pm 45/0_2]_s$ are summarized in Fig. 2.5, where it should be noted that the measured amplitude of imperfection was in the range $+1.27t$ to $-1.54t$.

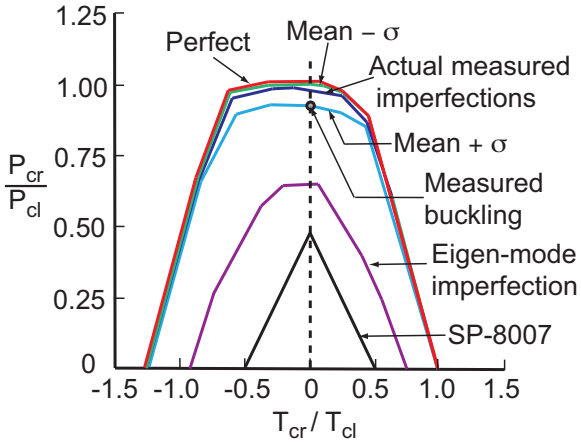

Figure 2.5: Predicted buckling loads for axially stiff shells under combined axial compression and torsion (Hilburger et al., 2006). P_{cr} and T_{cr} are the axial and torsional buckling loads of imperfect shells; P_{cl} and T_{cl} are the corresponding bifurcation buckling loads of perfect shells; σ is the standard deviation of the imperfection.

Figure 2.5 shows that the buckling loads predicted using an imperfection based on the critical eigenmode, or using the SP-8007 data (Peterson et al., 1965) are both much lower than the measured buckling load, indicating that using these two approaches can lead to rather conservative designs. Note that the buckling load predicted with the imperfection-signature approach closely matches the measurements.

2.1.1.4 Alternative Approaches: Aster Shell, Pseudo-Cylindrical Shell, and Ramm's Method

Jullien and Araar proposed an intuitive design for imperfection-insensitive cylindrical shells (Jullien and Araar, 1991; Araar, 1990; Araar et al., 1998). Having noted that in a cylindrical shell under axial compression the inward imperfections become amplified, whereas the outward imperfections maintain a constant amplitude, these authors considered a cross-sectional shape that is everywhere convex apart from symmetrically distributed, localized kinks. This cross-sectional shape, shown in Fig. 2.6, is obtained from the critical eigenmode of the shell, by taking the mirror image of all concave arcs. The resulting fluted shell, called the "Aster" shell, is a precursor of the solution proposed in this thesis. A knockdown factor of 0.77 was experimentally demonstrated for an Aster shell with $R = 75$ mm, $t = 153$ μm, and a deviation of $+2.3$ mm from the circle.

Figure 2.6: Cross-sections of dominant eigenmode of circular shell (solid and dashed arcs) and Aster shell (solid line) with $R/t = 490$.

Following Yoshimura (1951), Knapp (1974, 1977) proposed another intuitive shell design, pseudo-cylindrical shell, which approximates the buckled pattern under axial compressing by using flat polyhedral elements, as shown in Fig. 2.7. This concept is based on the assumption that, if a cylindrical shell is fabricated following the pattern in Fig. 2.7, it is more stable than the imperfection-sensitive circular geometry. However, Knapp did not study the imperfection-sensitivity of pseudo-cylindrical shells. Simulations carried by the author of this thesis show that the pseudo-cylindrical shell has a high knockdown factor of 0.9 and its buckling load is 30% lower than the perfect circular shell with the same radius, length, and material.

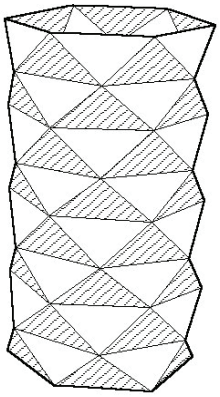

Figure 2.7: A buckled pattern approximated by flat polyhedral elements (from Yoshimura (1951)).

A general shape optimization method for thin shell structures was proposed by Reitinger et al. (1994) and Reitinger and Ramm (1995). Instead of considering only the buckling loads of perfect candidate structures, as in conventional structural optimization, these authors considered both perfect and imperfect structures in the evaluation of the objective function. This fundamental difference avoids convergence towards highly imperfection-sensitive designs.

The method consists of four steps linked in an optimization loop. First, the buckling load of the perfect structure, P_0, and the corresponding eigenmode, Φ, are computed. Second, the eigenmode is scaled by a prescribed amplitude and is adopted as imperfection shape; it is then superposed to the perfect geometry to define an imperfect shape. Third, the critical buckling load, P_{cr}, for the imperfect structure is calculated.

Finally, the minimum among P_0 and P_{cr} is chosen as the value of the objective function.

Applications of this method to the design of concrete shell roofs, stiffened panels, and free-form shells were presented by Reitinger and Ramm (1995); Ramm and Wall (2004).

2.1.1.5 Efficiency Chart

Quantitative comparisons of different structural designs require the use of suitable metrics. In the present case, the buckling performance of monocoque, stiffened, or any other kinds of cylindrical shells can be compared by considering the weight and load indices (Peterson, 1967; Agarwal and Sobel, 1977; Nemeth and Mikulas, 2009), which are defined as follows:

$$\begin{aligned} &\text{Weight index :} \quad \frac{W}{AR} \\ &\text{Load index :} \quad \frac{N_x}{R} \end{aligned} \tag{2.4}$$

Here W, A, and R are the total weight of the shell, the surface area, and radius of the cylinder, respectively, and

$$N_x = \frac{P_{cr}}{2\pi R} \tag{2.5}$$

denotes the (axial) critical buckling stress resultant. The surface area of the shell is $A = 2\pi RL$, where L is the length of the cylinder. Note that the weight and load indices are dimensional, this is the form commonly used by shell designers.

For circular monocoque cylindrical shells, the relation between weight and load indices can be found as follows. Begin by substituting $W = \rho At$ into the weight index expression, which gives

$$\frac{W}{AR} = \frac{\rho t}{R} \tag{2.6}$$

Then, solve Eq. 2.3 for t to obtain:

$$t = \sqrt{\frac{P_{cl}\sqrt{3(1-\nu^2)}}{2\pi E}} \tag{2.7}$$

Then, substitute Eq. 2.7 into Eq. 2.6 and replace P_{cr}/γ for P_{cl}, from Eq. 2.2, to obtain:

$$\frac{W}{AR} = \frac{\rho}{R}\sqrt{\frac{P_{cr}\sqrt{3(1-\nu^2)}}{2\gamma\pi E}} \tag{2.8}$$

Further substitution of $2\pi RN_x$ for P_{cr} , from Eq. 2.5, and simplification gives:

$$\frac{W}{AR} = \rho\sqrt{\frac{\sqrt{3(1-\nu^2)}}{\gamma E}\frac{N_x}{R}} \tag{2.9}$$

Figure 2.8 shows a plot of W/AR vs. N_x/R. The inclined straight line in the figure represents perfect ($\gamma = 1$) monocoque aluminum shells; the horizontal line corresponds to lightly-loaded shells which are subject to a minimum thickness constraint. The data points included in the plot represent (a) shells with integral-orthogonal stiffeners under axial compression (Katz, 1965), (b) z- and integrally-longitudinally stiffened shells under axial compression (Card, 1964a), (c) a corrugated graphite-epoxy ring-stiffened cylinder under bending (Davis, 1982), (d) ring-stiffened corrugated cylinders under axial compression (Peterson, 1967), and (e) z-stiffened shells subject to bending (Card, 1964b). Note that for structures subjected to bending the critical axial stress resultant used in the calculation of the load index was the peak axial stress resultant due to the critical bending moment, obtained from simple bending theory.

Shells closer to the right-bottom corner of the chart are the most efficient, as they can carry larger loads using less material. The chart shows that most stiffened cylindrical shells have higher efficiency than even perfect monocoque circular cylindrical shells. However, it should be noted that the reduced imperfection-sensitivity of stiffened cylindrical shells is countered by their complex manufacturing process. Machining from thicker stock and special forgings are the main manufacturing methods for metallic shells (Singer et al., 2002b). In 1986 the cost of a 320 mm diameter steel shell stiffened in one direction was on the order of \$3,500, and of \$15,000 for a similar, orthogonally stiffened shell (Scott et al., 1987; Singer et al., 2002b).

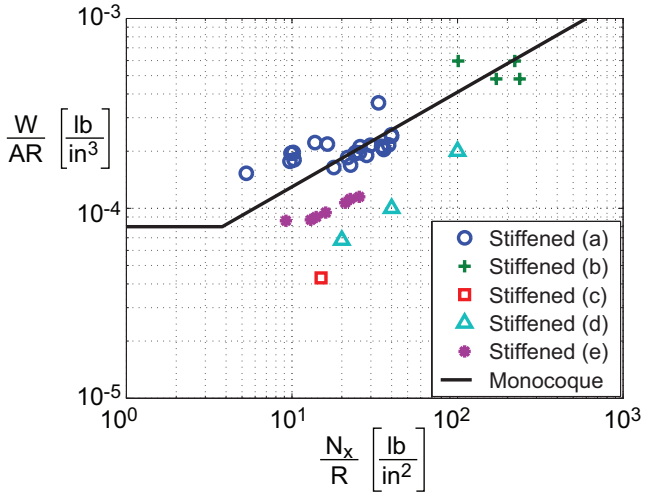

Figure 2.8: Performance chart for stiffened cylindrical shells described in Section 2.1.1.5 (data provided by Dr. M.M. Mikulas) and including plot of Eq. 2.9 for perfect ($\gamma = 1$) monocoque cylinders.

2.1.2 Experimental Methods

2.1.2.1 Manufacture of Cylindrical Shells for Research

Electroforming was one of the main methods of making monocoque metal cylindrical shells for research in the 1960s; see for examples Almroth et al. (1964); Arbocz and Babcock Jr (1968); Babcock (1962); Sendelbeck (1964). Electroformed shells were usually plated on wax mandrels sprayed with a thin layer of

conductive paint in electrolyte baths. The shells were removed from mandrels by melting the wax after plating. Extreme care was required to avoid damaging or warping the shells because the wax significantly expanded when it was heated to the melting point (Babcock, 1962). Electroformed shells usually have large imperfections due to the initial stresses generated in the plating processes (Singer et al., 2002b). In the 1980s and 90s, Jullien and his co-workers (Jullien and Araar, 1991; Araar, 1990) significantly improved the quality of electroformed shells by plating cooper or nickel on accurately machined duraluminum mandrels which were then chemically dissolved for separation of shells. Despite those improvements, it has been warned by Singer et al. (2002b) that electroforming remains a very difficult method that requires high skill and experience to produce consistently good specimens.

Machining from thicker stock and special forgings is usually used to make monocoque metal cylindrical shells when high accuracy is required and it is also the primary method to make high-quality integrally stiffened cylindrical shells (Singer et al., 2002b). For non-integrally stiffened cylindrical shells, stiffeners are welded or riveted to unstiffened cylindrical shells or flat plates which are then rolled onto a cylindrical mandrel; see for example Dowling and Harding (1982) and Card and Jones (1966). The fabrication processes of stiffened shells are very expensive. In 1986 the cost of a 320 mm diameter steel shell stiffened in one direction was on the order of $3,500, and of $15,000 for a similar, orthogonally stiffened shell (Scott et al., 1987; Singer et al., 2002b).

Composite materials have been increasingly used in aerospace structures because of their high stiffness, high strength, and low density. The fabrication procedure of composite cylindrical shells for research usually consists of a laminate lay-up process and an autoclave curing process. Graphite-epoxy shells made by Hilburger et al. (2006) are typical examples of small-scale monocoque composite cylindrical shells, which were laid up on a cylindrical mandrel, vacuum bagged and cured in an autoclave. Large composite shells can also be assembled from cylindrical panels which are warped from initially flat panels. For example, the 3-meter-diameter graphite-epoxy corrugated cylindrical shell in Johnson (1978) was assembled from three segments which were laid up and cured on a flat corrugated mold and then wrapped to the cylindrical shape. This approach is feasible for fabricating composite shells with flexible thin walls and a relatively large radius (Johnson, 1978).

2.1.2.2 Methods of Measuring Imperfections

The three-dimensional survey is currently the main method of measuring shell imperfections. A typical 3D survey instrument consists of a scanning rig and a data recording system (Verduyn and Elishakoff, 1982; Singer et al., 2002b). In a 3D survey procedure a shell surface is scanned by a probe, and the axial and circumferential positions of the probe tip are recorded. The probe moves along the axial direction of a shell, and the shell rotates around its axis so that the shell surface can be fully surveyed. For some 3D survey systems the scanning probe also moves in the circumferential direction of a shell which is fixed on the rig; see for example Arbocz and Williams (1977).

Shell imperfections are calculated by comparing the scanned shell surface to an imaginary perfect cylinder. The position of the perfect cylinder is determined by finding the best-fit cylinder to the measured data (Singer et al., 2002b). The method of least squares is usually used to minimize the sum of the squares of the normal distances from the measured points to the imaginary perfect cylinder by varying the rigid-body translations and rotations of the perfect cylinder (Arbocz and Babcock Jr, 1968; Cartalas et al., 1990; Hilburger et al., 2006). The solution of the minimization problem is the position of the best-fit perfect cylinder. The radial deviations of the measured surface with respect to the best-fit perfect imaginary cylinder are computed as imperfections.

Measured imperfections can be represented by Fourier series in order to analyze and compare the components of different imperfections. A commonly used form of Fourier series for decomposing initial imperfections is the half-wave cosine Fourier expansion (Arbocz and Babcock Jr, 1968; Singer et al., 2002b):

$$\omega(x,\theta) = t_{nom} \sum_{k=0}^{M} \sum_{l=0}^{M} cos(\frac{k\pi x}{L})[A_{kl} cos(l\theta) + B_{kl} sin(l\theta)] \tag{2.10}$$

where L and t_{nom} are the shell length and nominal thickness, respectively. x and θ denote the axial and circumferential coordinates. k and l are the wave numbers of axial half-cosine waves and circumferential full-waves, respectively. The Fourier coefficients are given by Cartalas et al. (1990):

$$\begin{aligned}
A_{00} &= \frac{1}{2\pi L t_{nom}} \int_0^L \int_0^{2\pi} \omega(x,\theta)\ dx\ d\theta \\
A_{k0} &= \frac{1}{\pi L t_{nom}} \int_0^L \int_0^{2\pi} \omega(x,\theta)\ cos(\frac{k\pi x}{L})\ dx\ d\theta, \qquad k > 0 \\
A_{0l} &= \frac{1}{\pi L t_{nom}} \int_0^L \int_0^{2\pi} \omega(x,\theta)\ cos(l\theta)\ dx\ d\theta, \qquad l > 0 \\
A_{kl} &= \frac{2}{\pi L t_{nom}} \int_0^L \int_0^{2\pi} \omega(x,\theta)\ cos(\frac{k\pi x}{L})\ cos(l\theta)\ dx\ d\theta, \qquad k > 0,\ l > 0 \\
B_{k0} &= 0, \qquad k \geq 0 \\
B_{0l} &= \frac{1}{\pi L t_{nom}} \int_0^L \int_0^{2\pi} \omega(x,\theta)\ sin(l\theta)\ dx\ d\theta, \qquad l > 0 \\
B_{kl} &= \frac{2}{\pi L t_{nom}} \int_0^L \int_0^{2\pi} \omega(x,\theta)\ cos(\frac{k\pi x}{L})\ sin(l\theta)\ dx\ d\theta, \qquad k > 0,\ l > 0
\end{aligned} \tag{2.11}$$

The amplitude of a component of an imperfection can be computed by:

$$\xi_{k,l} = \sqrt{A_{kl}^2 + B_{kl}^2} \tag{2.12}$$

2.1.2.3 Measurement of Shell Deformation and Recording of Buckling Behavior

Three-dimensional survey systems were commonly used for measuring shell prebuckling and postbuckling deformations in early shell buckling experiments; see for examples Arbocz and Babcock Jr (1968); Yamaki

and Otomo (1973); Araar (1990); Limam et al. (1991). The loads in those experiments were incrementally increased and stopped at each value of interest so as to scan the shell surface. Strain gages were usually used to measure shell strains. Recently, three-dimensional digital image correlation (DIC) systems have been utilized to measure shell deformations in buckling experiments of both small-scale (Wu et al., 2013) and large-scale shells (Hilburger et al., 2012a). The DIC is a non-contact technique that can measure shell deformations and strains without interrupting the testings. They can also provide full-field high-resolution measurements at a much higher speed than three-dimensional survey systems.

High-speed photography is required in order to record the behavior of shells during buckling because buckling is a very short dynamic procedure. So far most of the high-speed photography recordings for shell buckling experiments used film speeds of 1500 to 8000 frames per second (Singer et al., 2002b). Although modern high-speed cameras can operate at a very high film speed, the corresponding total recording time is very short. For example, the Phantom V310 high-speed camera (Vision Research, 2014) can only record for approximately 2 seconds at the film speed of 6000 frames per second with a resolution of 0.5 megapixels. Thus the timing for triggering high-speed cameras is very challenging and requires extreme care to capture the onset of buckling. However, if the shells can buckle at virtually the same load, the high-speed camera can be synchronized with the initiation of buckling (Singer et al., 2002b).

2.1.3 Computational Methods

2.1.3.1 Overview on Methods for Buckling Analysis of Corrugated/Stiffened Cylindrical Shells

Although current commercial finite element codes allow us to analyze the buckling behavior of corrugated and stiffened cylindrical shells, detailed simulations are computationally intensive. Typically, the overall dimensions of a cylindrical shell are much larger than the space between stiffeners or the wavelength and amplitude of corrugations. For example, a corrugated shell designed by Johnson (1978) had a diameter of 3 m, with a corrugation wavelength and amplitude of only 11.4 and 1.1 cm, respectively. Therefore, it would be necessary to use very small shell elements to accurately mesh the shell geometry and hence to obtain accurate results, leading to lengthy computations. This high computational effort has been the major constraint on the use of finite element analysis in the optimization of corrugated/stiffened shells (Bisagni and Vescovini, 2009).

A variety of methods have been introduced to reduce the computational effort required for the buckling analysis of corrugated and stiffened shells. A common approach is to replace their actual shell cross-section with a smooth shell surface that has equivalent stiffness properties. The smeared-out method is a simple method to compute the equivalent properties, and it has been used in the buckling analysis of both corrugated and stiffened shells since the 1960's (Block et al., 1965; Amazigo and Hutchinson, 1967; Simitses, 1971; Johnson, 1978). In this method discrete stiffeners or corrugations are distributed over the original shell surface by adding an equivalent continuous layer, and then the analysis is performed on a uniform but

anisotropic shell (Calladine, 1989).

Motivated by recent studies on corrugated morphing wings, various homogenization methods have been developed to obtain more rigorous equivalent stiffness properties than those provided by the smeared-out method, see Refs.Yokozeki et al. (2006); Thill et al. (2010); Briassoulis (1989); Liew et al. (2007); Xia et al. (2012); Ye et al. (2014). In the homogenization methods strains and curvatures are applied independently on a single corrugation (unit cell) and, exploiting the periodicity of corrugated shells, the corresponding reaction forces and moments at the boundaries of the unit cell are computed either analytically or numerically. The equivalent stiffness properties are then calculated through the load-displacement relations.

Both the smeared-out and homogenization methods are effective in reducing significantly the computational effort required by a finite element analysis because a much coarser mesh can be utilized, due to the simple geometry of the equivalent shells. However, these two methods are valid only when the buckling of the shell is global, i.e., only if the wavelength of the buckling mode is much larger than the wavelength of the corrugations or the space between stiffeners (Calladine, 1989; Bisagni and Vescovini, 2009). These methods cannot be used to capture local skin or stiffener buckling or to calculate stresses in the shell (Lamberti et al., 2003).

An alternative approach to the buckling and vibration analysis of corrugated and stiffened shells was developed in the 1980s by Williams and co-workers. These authors developed a stiffness matrix method that treated a shell as an assemblage of flat plates connected along their common longitudinal edges (Wittrick and Williams, 1974; Anderson et al., 1983; Williams and Anderson, 1983; Williams et al., 1990). In this method, the stiffness matrix for each plate is computed from the flat plate theory, and the buckling loads and modes are obtained by solving an eigenproblem. The program VIPASA was developed based on the stiffness matrix method, and it was found that VIPASA was much more efficient than general-purpose finite element programs (Singer et al., 2002b; Williams et al., 1990). VIPASA can analyze both flat and cylindrical corrugated and stiffened shells.

A unique feature of the stiffness matrix method is that, based on the periodicity of corrugated or stiffened shells, the buckling mode of a repeating portion can be expressed as a product of a complex-valued exponential term times the buckling mode of any repeating portion (Williams, 1986a,b). This relation makes it possible to condense the full stiffness matrix of the whole shell into a smaller matrix related to only a single repeating portion. However, this method can only analyze corrugated/stiffened shells consisting of flat plates. Shells with curved walls, e.g., sinusoidally corrugated shells, must be approximated by a series of flat panels. In addition, it should be noted that the buckling modes are assumed to vary sinusoidally along the corrugations/stiffeners in this method. Therefore, this method could provide inaccurate results if the shells are short and/or clamped in the longitudinal direction.

Another alternative approach of exploiting structural periodicity was the Bloch wave method for predicting the onset of buckling of infinitely periodic two ro three dimensional structures, which was developed in the 1990s by Triantafyllidis and co-workers (Geymonat et al., 1993; Triantafyllidis and Schnaidt, 1993;

Triantafyllidis and Schraad, 1998). Their method has been one of the major tools for the buckling analysis of cellular structures such as honeycombs (Lpez Jimnez and Triantafyllidis, 2013), porous solids (Bertoldi et al., 2008), and foams (Gong et al., 2005). The Bloch wave method is based on the fact that the buckling modes of an infinitely periodic structure follow the form of the Bloch wave propagation, which is the product of a complex-valued plane wave exponential term times a function with the periodicity of one repetitive unit cell (Kittel and McEuen, 1976). The buckling loads and corresponding eigenmodes can be computed by performing eigenvalue analyses on a single unit cell whose boundaries are coupled by the Bloch relations rather on the whole structure, resulting in a significant reduction of computational effort.

2.1.3.2 Stiffness Matrix Method

A buckling problem can be expressed as an eigenvalue problem:

$$K_c(\lambda_c)\tilde{U}_c = 0 \tag{2.13}$$

where K_c is the tangent stiffness matrix of the complete structure, $\tilde{U}_c$ is its eigenvector, which is also the buckling mode of the structure, and λ_c is the buckling load corresponding to the buckling mode $\tilde{U}_c$.

For a rotationally periodic structure, such as the ones shown in Fig. 2.9, with N repeating portions, $\tilde{U}_c$ can be partitioned into N subsets:

$$\tilde{U}_c = [\tilde{U}_1, \tilde{U}_2, \tilde{U}_3, ..., \tilde{U}_N]^T \tag{2.14}$$

where $\tilde{U}_q$ is the eigenvector of the q^{th} portion of the structure. The stiffness matrix of a rotational periodic structure has the following form (Williams, 1986a):

$$K_c = \begin{bmatrix} K_1 & K_2 & K_3 & \dots & K_N \\ K_N & K_1 & K_2 & \dots & K_{N-1} \\ K_{N-1} & K_N & K_1 & \dots & K_{N-2} \\ \vdots & \vdots & \vdots & \vdots & \vdots \\ K_2 & K_3 & K_4 & \dots & K_1 \end{bmatrix} \tag{2.15}$$

where K_q is the stiffness matrix corresponding to the q^{th} portion of the structure. Let the number of degrees of freedom of each repeating portion be J, then K_q is a $J \times J$ matrix.

Hence, Eq. 2.13 can be written as a set of m equations:

$$\Sigma_{q=1}^{N} K_q \tilde{U}_{m+q-1} = 0, \quad m = 1, 2, 3, ...N \tag{2.16}$$

where

$$\tilde{U}_{q+N} = \tilde{U}_q \tag{2.17}$$

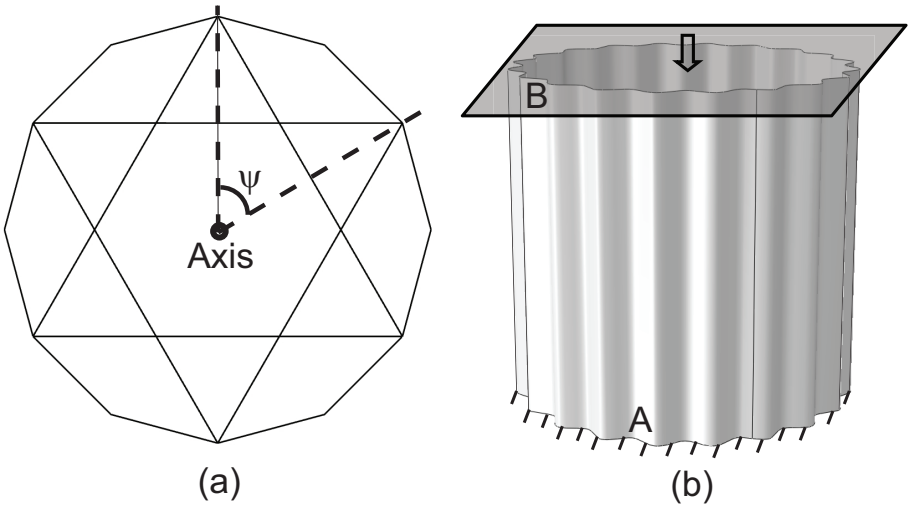

Figure 2.9: (a) Rotationally periodic 2D truss structure with 6 repeating portions, $\psi = 2\pi/6$ is the angle subtended by the repeating portion. (Williams, 1986b) (b) Rotationally periodic corrugated shell subject to axial compression. The top edge "B" is clamped to a rigid plate. The boundary conditions on all nodes along edges "A" or "B" are identical.

The most general solution to Eqs. 2.16 and 2.17 is (Williams, 1986a)

$$\tilde{U}_q = \tilde{U}_1 \exp[i(q-1)n\psi], \qquad n = 0, 1, 2, 3, ...N \tag{2.18}$$

with $i = \sqrt{-1}$, $n = 0, 1, 2, ..., N$, and $\psi = 2\pi/N$. Substituting Eq. 2.18 into Eq. 2.16 and dividing it by $\exp[imn\psi]$, we can formally reduce the set of m equations to the single equation:

$$(\Sigma_{q=1}^{N} K_q \exp[i(q-1)n\psi])\tilde{U}_1 = 0, \qquad n = 0, 1, 2, 3, ...N \tag{2.19}$$

which still needs to be solved to for each value of n in order to find the smallest value of λ_c.

It should also be noted that, because it is equivalent to define the buckling modes in either an anti-clockwise or clockwise sense around the structure,

$$\exp[i(q-1)(N-n)\psi] = \exp[-i(q-1)n\psi] \tag{2.20}$$

n and $N-n$ are not independent and the range of n can be reduced to $n = 1, 2, 3, ...\{N/2\}$, where $\{N/2\}$ is the largest integer no larger than $N/2$.

Thus it has been shown that the eigenvalue problem in Eq. 2.13, posed in terms of the tangent stiffness matrix of the complete structure, K_c, is equivalent to $\{N/2\}+1$ J-dimensional eigenvalue problems posed in terms of the $\Sigma_{q=1}^{N} K_q(\lambda_c) \exp[i(q-1)n\psi]$, where J is the size of the stiffness matrix for the repeating portion of the structure.

However, note that the displacement vector $\tilde{U}_i$ is complex-valued and hence in general both the real and

imaginary parts of $\tilde{U}_i$ are possible buckling modes. When $n = 0$ or $n = N/2$ for even N, the exponential term in Eq. 2.18 is a real value and hence there is only one buckling mode corresponding to these two cases. The critical buckling load is the lowest one among the buckling loads for all n's.

$$\lambda_{crit} = \min_{n=0,1,\ldots,\{N/2\}} (\lambda_c(n)) \tag{2.21}$$

It is common for rotationally periodic structures to have "axis nodes", i.e., nodes shared by all the repeating portions or have the same translational and rotational deformation with respect to the axis. For example, stiffened or corrugated cylindrical shells subject to axial uniform end-shortening have "axis nodes" on their two ends, as shown in Fig. 2.9 (b). Let $\tilde{U}_{Zq}$ be the displacement w.r.t axis Z of the "axis nodes" of the q^{th} portion, and substitute it into Eq. 2.18:

$$\tilde{U}_{Zq} = \tilde{U}_{Z1} \exp[i(q-1)n\psi], \qquad n = 0, 1, 2, 3, \ldots\{N/2\} \tag{2.22}$$

Because the nodes are "axis nodes", $\tilde{U}_{Zq}$ must satisfy $\tilde{U}_{Zq} = \tilde{U}_{Z1}$. Therefore, $\tilde{U}_{Zq}$ is always zero for $n > 0$.

2.1.3.3 Bloch Wave Method

The Bloch wave method is a robust and efficient way of predicting the onset of buckling for 2-dimensional and 3-dimensional infinitely periodic structures (Geymonat et al., 1993; Triantafyllidis and Schnaidt, 1993; Triantafyllidis and Schraad, 1998; Gong et al., 2005; Lpez Jimnez and Triantafyllidis, 2013; Bertoldi et al., 2008). In this section we use a two-dimensional, infinitely periodic structure, as shown in Fig. 2.10, to briefly review the Bloch wave method.

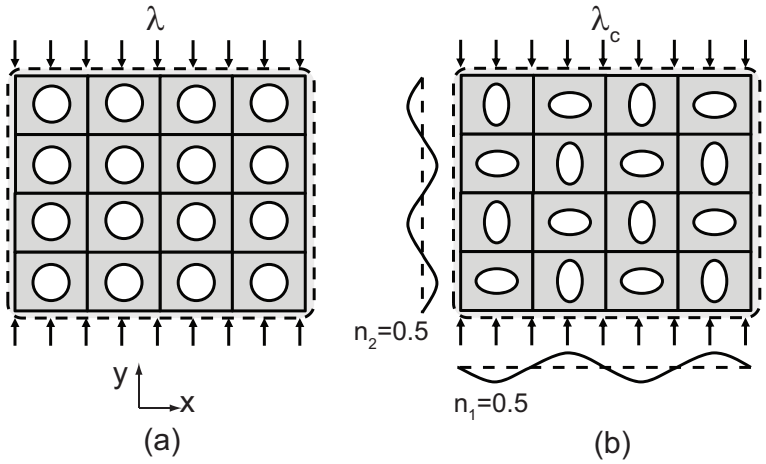

Figure 2.10: (a) Schematic of a 2D infinitely periodic porous structure subject to compression in y-direction. (b) A buckling mode and its corresponding buckling load λ_c.

When the compressive load λ is smaller than the buckling load, the periodicity of the structure is still one unit cell in both x- and y-directions, as shown in Fig. 2.10 (a). If the compressive load reaches the buckling

load λ_c, the original periodicity could be broken and the new repeating pattern could involve several unit cells. Fig. 2.10 (b) shows a buckling mode with a periodicity of 2 unit cells in both x- and y-directions. It has been proved that the buckling modes of a 2-dimensional infinite periodic structure have the following form (Geymonat et al., 1993; Triantafyllidis and Schnaidt, 1993; Triantafyllidis and Schraad, 1998):

$$\tilde{U}_c(x,y) = P_u(x,y)\exp[2\pi i(\frac{n_1}{L_1}x + \frac{n_2}{L_2}y)] \tag{2.23}$$

where L_j and n_j, $j = 1, 2$ are respectively the lengths of the unit cell and the wave numbers. $\tilde{U}_c$ denotes the displacement of the complete infinite structure. $P_u(x,y)$ is a periodic function with a periodicity of one unit cell:

$$P_u(x,y) = P_u(x + m_1L_1, y + m_2L_2) \tag{2.24}$$

where m_1 and m_2 are integers. Note that both P_u and $\tilde{U}_c$ are complex-valued functions.

The exponential term in Eq. 2.23 is essentially a wave propagation term that controls the propagation of P_u. For example, if $n_1 = 0.5$ and $n_2 = 0.5$, the imaginary part of the exponential term follows the sinusoidal waves, as shown in Fig. 2.10 (b), whose wavelength is 2 unit cells in both x- and y-directions. Since the periodicity of P_u is one unit cell, the buckling mode corresponding to $n_1 = n_2 = 0.5$ has a periodicity of two unit cells in both x- and y-directions. Therefore, each value for the wave number n_1 or n_2 represents a buckling mode for the structure in Fig. 2.10 (a). Eq. 2.23 is also called the Bloch wave propagation function and is what the Bloch wave method is named after.

The buckling problem of the complete infinite structure can be written as an eigenvalue problem:

$$K_c(\lambda_c)\tilde{U}_c = 0 \tag{2.25}$$

where K_c is the tangent stiffness matrix of the complete structure and λ_c is the buckling load. The above eigenvalue problem cannot be solved due to the infinity of the structure. However, the condition of buckling corresponding to a single unit cell in Fig. 2.11 can be separated from Eq. 2.25 and written as:

$$K(\lambda_c)\tilde{U} = \tilde{F} \tag{2.26}$$

where $\tilde{U}$ and $\tilde{F}$ are respectively a buckling mode and force vector of a unit cell. $K(\lambda_c)$ denotes the tangent stiffness matrix of the unit cell corresponding to the buckling load λ_c. It should be noted in the present case that $\tilde{F}$ is not zero because we are considering only a piece of the structure, and hence non-zero nodal forces need to be applied at the periodic boundaries. Eq. 2.26 is not an eigenvalue problem and it cannot be directly solved.

According to the buckling mode in Eq. 2.23, the displacements in regions “a” and “b” are not independent.

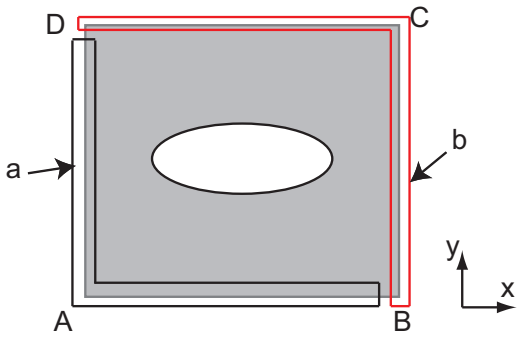

Figure 2.11: Schematic of a buckled unit cell of a 2D infinitely periodic porous structure. A, B, C, and D are four points on the corners of the unit cell. Region "a" includes edges AD, AB, and point A; region "b" includes edges CD, BC, and points B, C, and D.

For example, the displacements on edges AD and BC are coupled by the following relation:

$$\tilde{U}_{BC} = \exp[2\pi i n_1]\tilde{U}_{AD} \tag{2.27}$$

Edges AB and CD also follows the similar coupling relation. Eq. 2.27 is called displacement Bloch relation. The force vector in Eq. 2.26 also follows the Bloch wave propagation function (Geymonat et al., 1993; Triantafyllidis and Schnaidt, 1993; Triantafyllidis and Schraad, 1998):

$$\tilde{F}_c(x,y) = P_f(x,y)\exp[2\pi i(\frac{n_1}{L_1}x + \frac{n_2}{L_2}y)]. \tag{2.28}$$

where $P_f(x,y)$ is a periodic function with the periodicity of one unit cell. Therefore, the force vectors on edges AD and BC are also coupled:

$$\tilde{F}_{BC} = -\exp[2\pi i n_1]\tilde{F}_{AD} \tag{2.29}$$

The negative sign is because the reaction forces on edges AD and BC are in opposite directions. Eq. 2.29 is the force Bloch relation. The details of the Bloch relations are presented in Appendix A.

The dependent displacements can be eliminated by defining a coupling matrix Q:

$$\tilde{U} = Q[\tilde{U}_i, \tilde{U}_a]^T \tag{2.30}$$

where i and a denote the internal nodes and nodes in region "a" , respectively, as shown in Fig. 2.11. Q contains the exponential terms in the Bloch relations, and hence it is a function of the wave numbers n_1 and n_2. The derivation of Q is presented in Appendix A.

Substituting Eq. 2.30 into Eq. 2.26 and pre-multiplying by Q^T, we obtain:

$$Q^T K(\lambda_c) Q[\tilde{U}_i, \tilde{U}_a]^T = Q^T \tilde{F} \tag{2.31}$$

It can be shown that the right-hand-side of Eq. 2.31 is zero because of the conditions enforced by the force Bloch relations. Hence, we can define the reduced stiffness matrix:

$$\hat{K}(n_1, n_2, \lambda_c) = Q^T K(\lambda_c) Q \tag{2.32}$$

and write Eq. 2.31 as

$$\hat{K}(n_1, n_2, \lambda_c)[\tilde{U}_i, \tilde{U}_a]^T = 0 \tag{2.33}$$

Therefore, the buckling load and mode can be obtained by solving the eigenvalue problem of matrix $\hat{K}$. It should be noted that $\hat{K}$ also depends on n_1 and n_2; hence, the buckling load factor λ_c is a function of n_1 and n_2. The critical buckling load is obtained by finding the lowest λ_c for all possible n_1 and n_2:

$$\lambda_{crit} = \min_{n_1, n_2}(\lambda_c(n_1, n_2)) \tag{2.34}$$

There are infinite values of n_1 and n_2 for an infinite structure. Therefore, the Bloch wave method is used to find the buckling loads corresponding to the modes with short wavelength. For infinite periodic structures, the buckling modes with very large wavelength are usually analyzed by homogenization method.

Note that the Bloch wave relations and the displacement vectors are complex-valued functions. However, most finite element packages, including Abaqus, cannot handle complex-valued fields. Many authors have formulated the stiffness matrices K and $\hat{K}$ analytically, and had to carry out lengthy derivations or develop special purpose software.

Gong et al. (2005) generated K with the finite element package Abaqus and then obtained $\hat{K}$ from algebraic manipulations. Aberg and Gudmundson (1997) proposed an alternative technique for studying the wave dispersion relations of infinite periodic structures that used two identical meshes in Abaqus to split the complex-valued fields into real and imaginary parts. The boundaries of the two meshes were coupled in order to satisfy the Bloch relations. Following Aberg and Gudmundson (1997), Bertoldi et al. (2008); Shim et al. (2013) introduced this technique in the buckling analysis of porous periodic elastomeric structures.

Recently, the Bloch wave method was introduced in the buckling analysis of stiffened cylindrical shells by Wang and Abdalla (2015). These authors used the Bloch wave method to find the local buckling loads and modes of stiffened shells (the global buckling modes were analyzed through a homogenized stiffness model). The Bloch wave method for 2-dimensional infinite periodic structures was used without considering the boundary conditions for the shell, hence assuming the shell to be infinitely long. The constraints of rotational periodicity on the buckling mode were also neglected.

2.1.3.4 Comparison between Stiffness Matrix Method and Bloch Wave Method

The stiffness matrix method for rotationally periodic structures and the Bloch wave method for infinitely periodic structures have similar features. First, both methods achieve significant reductions in computational

effort by partitioning the eigenproblem for the whole structure into a series of smaller eigenproblems that involve stiffness matrices with the same dimension as the matrix of a single unit cell. Second, the assumed buckling mode relations among repeating portions of the structure in the stiffness matrix method (Eq. 2.18) are essentially the same as the Bloch wave relations in Eq. 2.27.

However, these two methods formulate the eigenproblems in different ways. The stiffness matrix method involves the stiffness matrices of all the repetitive portions of a rotationally periodic structure, as shown in Eq. 2.19. The stiffness matrix in the Bloch wave method involves only a single unit cell, and the boundaries of the unit cell are coupled by the Bloch wave relations to transform the buckling condition (Eq. 2.26) for a unit cell into an eigenproblem, as seen in Eq. 2.33.

2.2 Reviews of Externally Pressurized Spherical Shells

This section briefly reviews the theoretical and experimental studies on the imperfection-sensitivity of complete spherical shells under external pressure. Extensive reviews can be found in references Bushnell (1985), Kaplan (1974), and Singer et al. (2002b).

2.2.1 Analytical and Numerical Studies

The first contribution to the understanding of the discrepancies between measured and theoretically predicted buckling pressures of spherical shells under external pressure was also made by Von Kármán and Tsien (Von Kármán and Tsien, 1939; Tsien, 1942). They assumed the buckling mode of an externally pressured sphere was a localized dimple. Instead of only considering infinitesimal deformations, they introduced nonlinear finite displacements in their analyses and found that the postbuckling equilibrium path dropped sharply, which was similar to the postbuckling path of a cylindrical shell subject to axial compression. Their work suggested that the buckling of externally pressurized spherical shells were sensitive to imperfections. Later, Thompson included initial imperfections in his analyses and confirmed the imperfection-sensitivity (Thompson, 1962, 1964a,b).

Several authors have investigated the influence of initial geometric imperfections on the buckling pressure of spherical shells under external pressure. Sabir (1964) assumed that the effect of an initial imperfection was equivalent to that of a concentrated load causing that imperfection. Based on this assumption, Sabir calculated the relation between the critical buckling pressure and imperfection amplitude. Hutchinson (1967) investigated the imperfection-sensitivity based on Koiter's initial postbuckling theory. He used shallow shell theory, so he considered a shallow region and neglected the continuity with the rest of the sphere (Kaplan, 1974). Koiter (1969) modified the analyses by Hutchinson and conducted extensive investigations on complete spherical shells with several radius to thickness ratios. Bushnell (1967) investigated the influence of imperfections with local radius of curvature of up to 6 times of shell radius. Koga and Hoff (1969) used a nonlinear shell theory in the deflected region of a sphere and a linear theory in the undeformed region.

Two types of imperfections, dimpled imperfection and flattened imperfection similar to Bushnell (1967), were investigated in his study. The relations between buckling pressures and amplitudes of imperfection obtained in the above analyses are summarized in Fig. 2.12. Although the results of these studies are different due to the differences in assumptions, theories, and shapes of imperfections, it can be found that the imperfection-sensitivity of externally pressurized spherical shells is very high.

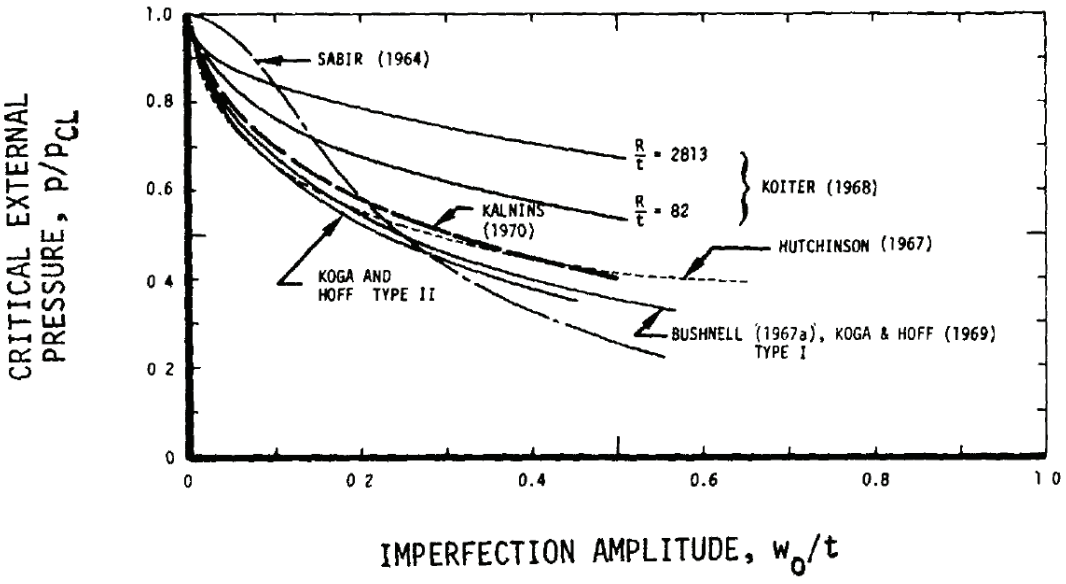

Figure 2.12: Imperfection-sensitivity of complete spherical shells (from Kaplan (1974)).

2.2.2 Experimental Studies

The experimental buckling behavior of complete spherical shells under external pressure has been extensively investigated since the 1960s. Comprehensive reviews on the experiments can be found in references Kaplan (1974) and Singer et al. (2002b). Here only brief reviews of experiments performed by Krenzke (1962) are provided because they proposed an empirical equation to estimate the buckling pressures of imperfect spherical shells and the equation is still being used (Pan and Cui, 2010).

Krenzke (1962) preformed tests on 26 carefully machined hemispheres. Krenzke simulated the behavior of complete spherical shells by supporting the hemispherical shells on ring-stiffened cylindrical shells which provided membrane boundary conditions. Based on the measured buckling pressures, he assumed that the elastic buckling pressure was approximately 70% of the classical value, i.e.:

$$P_E = 0.7P_{cl} \tag{2.35}$$

where P_E and P_{cl} are estimated and classical buckling pressures, respectively. P_{cl} can be obtained by a linear elastic buckling analysis and has the following form (Timoshenko and Gere, 1961):

$$P_{cl} = \frac{2E}{\sqrt{3(1-\nu^2)}}(\frac{t}{R})^2 \tag{2.36}$$

where E, ν, t, and R are respectively the Young's modulus, Poisson's ratio, thickness and radius of spherical shell. Therefore, Eq. 2.35 can be written as:

$$P_E = 0.84E(\frac{t}{R})^2 \tag{2.37}$$

Krenzke also included the effect of plasticity and modified the above equation to consider the reduction of buckling pressure due to plasticity:

$$P_E = 0.84\sqrt{E_s E_t}(\frac{t}{R})^2 \tag{2.38}$$

where E_s and E_t are the secant and tangent moduli, respectively.

Krenzke and Kiernan (1963) performed exploratory experimental studies on stiffened hemispherical shells and concluded that stiffening could not be effective unless the stiffeners are closely spaced and in both hoop and meridional directions of the shell. They found that the buckling pressures of stiffened spherical shells were not as great as those of unstiffened spherical shells with the same weights. Therefore, they argued that considerable theoretical and experimental investigations were required in order to find the efficient configurations of stiffened spherical shells.

Chapter 3

Design of Imperfection-Insensitive Cylindrical Shells

This chapter presents a method for designing imperfection-insensitive axially compressed cylindrical shells and some designs that are produced through this method. These designs are compared to each other and to some alternative shell designs. The mass efficiency of the designed shells and the effects of shell length are also discussed.

It is assumed that the material of the shells in this chapter is linearly elastic; hence, the strength of the material is not considered. It is also assumed that the shells in this chapter collapse due to buckling. However, structural collapse due to material failure will be considered in the experimental validations in the next chapter.

3.1 Methodology

We have adopted the method of Ramm and co-workers (Reitinger et al., 1994; Reitinger and Ramm, 1995) to search for the cross-sectional shape of imperfection-insensitive monocoque linear-elastic cylindrical shells with maximal buckling load. This section presents the methodology to parameterize the shape of the cross-section and to formulate the design problem; the implementation of the design process is also presented.

3.1.1 Parametrization of Cross-Section

The improved buckling load and decreased sensitivity to imperfections of the Aster shell motivated us to explore corrugated shells with general cross-sectional shapes and to introduce the concept of the *wavy shell*, shown in Fig. 3.1.

The cross-section of the wavy shell is defined by a set of control points, with a NURBS (Non-Uniform Rational B-Spline) interpolation creating a smooth curve through the control points. The NURBS is given

by (Hughes et al., 2009):

$$C(\xi) = \sum_{i=1}^{n} N_{i,p}(\xi) B_i, \tag{3.1}$$

where $N_{i,p}$ is a piecewise base function and B_i is a vector of control points. ξ, p, and n denote a parametric coordinate, the order of NURBS, and the number of base functions, respectively. The base functions are recursively defined as (Hughes et al., 2009):

$$N_{i,p}(\xi) = \frac{\xi - \xi_i}{\xi_{i+p} - \xi_i} N_{i,p-1}(\xi) + \frac{\xi_{i+p+1} - \xi}{\xi_{i+p+1} - \xi_{i+1}} N_{i+1,p-1}(\xi). \tag{3.2}$$

For $p = 0$:

$$N_{i,0}(\xi) = \begin{cases} 1 & \text{if } \xi_i \leq \xi \leq \xi_{i+1}, \\ 0 & \text{otherwise} \end{cases} \tag{3.3}$$

where ξ_i is the i^{th} knot in the knot vector $\Xi = (\xi_1,\ \xi_2,\ ..., \xi_{n+p+1})$. In the present study, 3^{rd} degree NURBS with uniform knots, i.e., $\Xi = (1,\ 2,\ ...,\ n+4)$, were chosen. These base functions are periodic, which guarantees that the closed cross-section generated by this NURBS has smooth slope and curvature everywhere.

The wavy shell is defined to be axially uniform, so that the longitudinal stress resultant is the dominant one. A varying cross-section would induce shear and possibly even bending when the shell is loaded under axial compression, resulting in a decrease in the axial stiffness of the shell and its buckling load.

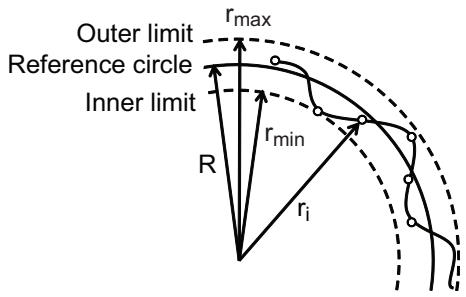

Figure 3.1: Definition of wavy shell geometry showing also several control points.

Two main geometric constraints were introduced to narrow down the design space. First, the control points were defined to be circumferentially equally spaced and radially within a distance Δr from a reference circle of radius R, see Fig. 3.1. This radial limit avoids excessive curvature of the wavy cross-section. The circumferential position of the i^{th} control point in the first quadrant, $\theta_{1,i}$, is given by

$$\theta_{1,i} = \frac{\pi(i-1)}{2(N-1)}, \tag{3.4}$$

where N is the total number of control points in the first quadrant, including any control points lying on the x- and y-semi-axes.

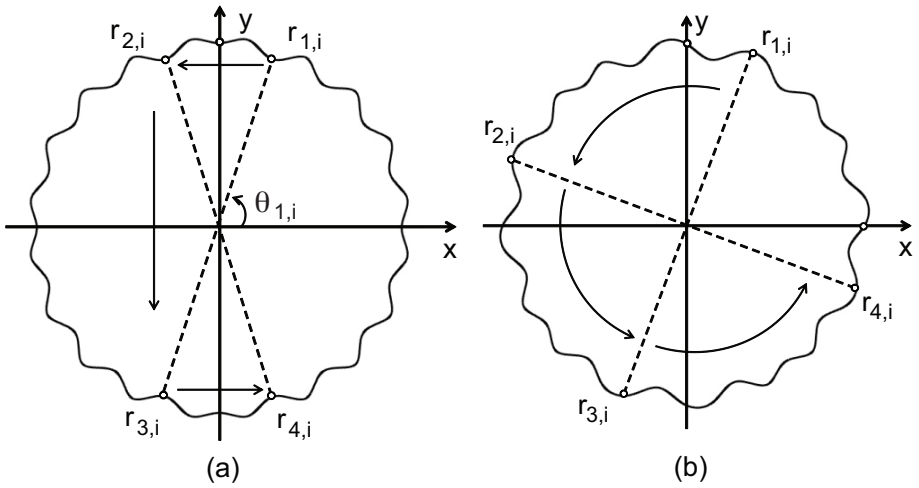

Figure 3.2: Cross sections with (a) mirror-symmetry and (b) 4-fold symmetry. $r_{q,i}$ denotes the radial position of the i^{th} control point in the q^{th} quadrant.

Second, to further narrow down the design space, the wavy section was assumed to be either mirror-symmetric with respect to the x- and y-axes, as shown in Fig. 3.2 (a), or 4-fold rotationally symmetric as shown in Fig. 3.2 (b). In the first case there are only N control points in the first quadrant (of which two lie on the x and y-axes) that divide it into $N-1$ sectors subtending equal angles. In the second case only $N-1$ control points are needed (of which one lies on the axis) and all other points are obtained by rotation operations. Note that the two symmetry schemes with N and $N-1$ control points result in the same spatial resolution for the wavy cross-section.

Thus, the cross-section is defined by:

$$C = \begin{cases} C(r_{1,1},\ r_{1,2},\ ...,\ r_{1,N}) & \text{mirror-symmetry,} \\ C(r_{1,1},\ r_{1,2},\ ...,\ r_{1,N-1}) & \text{4-fold symmetry} \end{cases} \tag{3.5}$$

3.1.2 Formulation of Optimization Problem

For every candidate cross section, C, the objective function is defined as the minimum among the following three buckling loads:

- the bifurcation buckling load, P_0, of the geometrically perfect structure;
- the buckling load, P_+, of a geometrically imperfect structure obtained by superposing an imperfection of positive sign onto the perfect structure; and
- the buckling load, P_-, of a structure with an imperfection of negative sign.

The imperfection shape was chosen as the first (critical) buckling mode, for the following reasons. First, finding the actual imperfection shape that leads to the lowest buckling load is, after many years of research,

still an open issue; a widely used approach is to use the critical buckling mode; see for example Ramm and Wall (2004), Hilburger et al. (2006) and Jones (2006). Second, tests and analyses carried out by Hilburger et al. (2006) and reviewed in Section 2.1.1.3 have shown that the critical-mode imperfection leads to lower buckling load predictions than the actual values, indicating that it is a conservative choice that provides a lower bound on the buckling loads that can be expected in practice. Third, we have carried out a detailed optimization study of wavy cylinders in which the first four critical modes were used to define the imperfection shape. Compared with the designs obtained using only the first critical mode, the reduction in the buckling loads with the additional imperfections was only 3%. In conclusion, the critical buckling mode is adequate for the present study. Figure 3.3 shows the geometrically perfect structure and one of the two imperfect structures that were analyzed at one step of the optimization process.

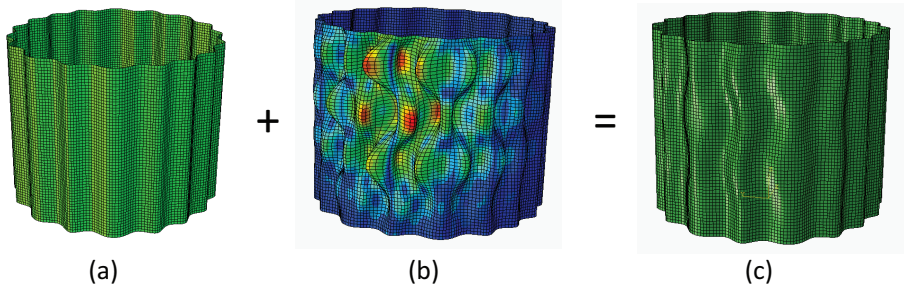

Figure 3.3: (a) Wavy shell with perfect geometry, $C_0(r_{1,1},\ r_{1,2},\ ...)$; (b) imperfection shape based on critical buckling mode, $\mu\Phi$, with $\mu = 10t$ for clarity; (c) imperfect wavy shell, $C_+ = C_0(r_{1,1},\ r_{1,2},\ ...) + \mu\Phi$.

The imperfection amplitude was set equal to the shell thickness. According to Fig. 2.2 this amplitude will cause a five-fold decrease in the buckling load and hence provide a significant challenge for the present search for imperfection-insensitive designs. Of course, the actual amplitude of the imperfections depends on the manufacturing processes that are adopted; the effects of imperfection amplitudes larger than t are analyzed in Section 3.3.3.

Regarding the sign of the imperfections, both positive and negative imperfection signs need to be considered in order to capture the different types of imperfection-sensitivity discussed in Section 2.1.1.1.

In summary, the optimization problem was formulated as follows:

$$
\begin{aligned}
&\text{Maximize :} \quad \min\ (P_0, P_+, P_-) \\
&\text{among all wavy shells with either mirror-symmetric or 4-fold symmetric} \\
&\text{cross-sections, defined by the control variables:} \\
&r_{1,i},\ i = 1,\ 2,\ 3,\ ... \\
&\text{that are subject to :} \\
&|r_{1,i} - R| \ \leq\ \Delta r,\ i = 1,\ 2,\ 3,\ ....
\end{aligned}
\tag{3.6}
$$

where:

- P_0, P_+, and P_- are respectively the buckling loads of wavy shells with perfect geometry, imperfect geometry with positive imperfection, and imperfect geometry with negative imperfection;
- the positive imperfection is $+t\Phi$ and the negative imperfection is $-t\Phi$, where Φ is the critical-mode imperfection.

3.1.3 Numerical Implementation

Our implementation of the design optimization problem was based on existing software, including commercial computer-aided design (CAD) and finite-element analysis (FEA) software, and an open-source optimizer, all run by a Matlab script. This section describes the three softwares that were used and how they were interfaced.

The NURBS-based CAD software Rhino 3D (version 5.0) was used to create CAD models of the cross-sections of the perfect wavy shells. The NURBS interpolation solver embedded in Rhino 3D was used to read a text file containing the positions of the control points and to create the cross-section geometry, which was then exported as an Initial Graphics Exchange Specification (.IGS) file. This process was automated by means of a Python script. This Python scripting interface has been successfully used in the papers by the present author (Ning and Pellegrino, 2012, 2013, 2015a,b).

The optimization process requires FEA software that can be automated through a scripting interface to set up analysis models and run non-linear buckling analyses. There exists some very efficient finite element formulations for axisymmetric shells, such as shell elements based on Fourier analysis for the buckling analysis of cooling towers (Combescure and Pernette, 1989). This formulation can also be used to analyze the influence of Fourier mode imperfections on the non-linear buckling behavior of an axisymmetric shell; however, it is not applicable to the present situation.

The general purpose package Abaqus 6.11 was chosen. Abaqus/CAE was used to read the .IGS file, set up three structural models (the first model with the perfect geometry and the two others with imperfect geometries based on either positive or negative imperfections), and compute the buckling load for each model.

For each candidate design, a Python script set up an Abaqus/Standard model of the shell with perfect geometry. A linear eigenvalue buckling analysis was carried out on this initial model to compute the critical eigenmode, Φ. Next, the displacements of the nodes according to the first eigenmode were extracted from the Abaqus/Standard output file and were scaled with the maximum transverse displacement equal to the shell thickness.

Two FEA models of imperfect shells were obtained by superposing the scaled displacements on the mesh of the perfect shell. For the perfect geometry and also for each of the imperfect geometries, the critical buckling load was computed by carrying out a load-displacement arc-length incrementation non-linear analysis, using the Riks solver in Abaqus/Standard.

Figure 3.4 shows plots of the relationship between axial load vs. axial displacement, obtained from non-

linear analyses of the perfect shell and both imperfect shells. In each load-displacement curve, the first limit load has been taken as the buckling load. The Abaqus/Standard Riks solver may turn back at the first limit load and fail to compute the post-buckling behavior. This was not an issue in the present case, since only the buckling load value is of interest. The increments in the arc-length were automatically determined by the solver, and the first limit loads were usually reached after 10 to 30 increments. The maximum number of increments was set to 50, which was sufficient to reach the first limit load in all examples presented in this thesis.

The results of our simulations were checked by changing the maximum allowed increments from a large value (typically, 1 kN) down to a small value (100 N); the differences between these two cases were found to be within 1%. It should be noted that Abaqus automatically reduce the increment as the non-linearity of the response increases. It was found that a typical increment was less than 5 N when the applied loads are close to the bifurcation points.

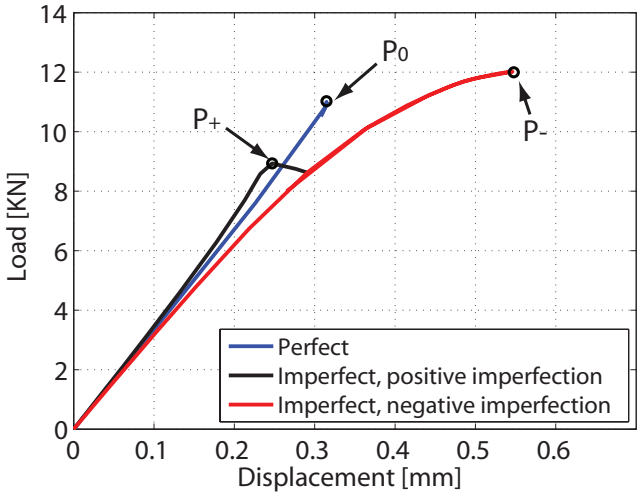

Figure 3.4: Schematic of equilibrium diagrams for geometrically perfect and imperfect shells, showing definition of limit loads. In the example shown the load-displacement curves for the perfect shell and the imperfect shell with negative imperfection turn back at the first limit load.

Fully-integrated quadrilateral thin-shell elements (element S4) were used for all the Abaqus models in this chapter. In order to obtain mesh sensitivity, we performed buckling analyses on a perfect composite sinusoidal shell with 40 waves using various sizes of elements and the simulation techniques described above. The geometry, material, and boundary conditions of this sinusoidal shell can be found in Section 3.4.1. The buckling loads and computational time are summarized in Table 3.1. The analyses were run on a Xeon X5680 server with 12 CPUs on a single motherboard, and all the 12 CPUs were used for each simulation. The buckling load converged to 14.70 kN as the size of elements decreased. The computational time increased significantly when the element size was reduced to 0.5 mm from 1 mm. Therefore, the element size of 1 mm was chosen because it provided sufficient accuracy at a low computational cost.

Lastly, the Evolution Strategy with Covariance Matrix Adaption (CMA-ES) (Hansen et al., 2003) and

Table 3.1: Buckling loads and computational time obtained from Abaqus models with various element sizes.

Element size [mm]	3	2.5	2	1.5	1	0.5
P_0 [kN]	15.54	15.36	15.21	14.82	14.69	14.70
Time [minutes]	4	4	4	9	12	20

Hansen (2011) open source algorithm (Hansen, 2012) was used as the optimizer. The background to this choice is that the optimization problem in Eq. 3.6 does not have an explicit mathematical expression and, due to the highly non-linear relationship between shape and buckling loads, the objective function is expected to be non-convex. Therefore, evolutionary optimizers were evaluated and CMA-ES was selected for its efficiency, see Bäck (1996) for a review of basic concepts.

An initial population of eight wavy shells was randomly chosen. Shells with higher $min(P_0, P_+, P_-)$ were ranked higher. The top 4 designs in the population of each generation were selected as parents and their design variables were recombined and mutated to create 8 offspring structures for the next generation. The critical loads, P_0, P_+, and P_-, of the best design in each generation were recorded. After running the optimization for a set number of iterations, typically 150, the structure with maximal $min(P_0, P_+, P_-)$ was taken as the final solution.

The simulations were run on a Xeon X5680 server with 12 CPUs on a single motherboard. Tests showed that simultaneously running 4 jobs on 3 CPUs for each job minimized the average simulation time. A population size that is a multiple of 4 can best use this computational resource and, due to the small number of design variables considered in the present study, the population size was chosen as 8. The total simulation time to evaluate (P_0, P_+, P_-) for a population of 8 structures was about 1 hour.

3.2 Wavy Shell Designs

Four imperfection-insensitive carbon-fiber composite shells with a common set of dimensions and material properties, loaded under axial compression and clamped at both ends are presented.

3.2.1 Dimensions and Material Properties

Typical applications of cylindrical shells under axial compression are intertanks and interstages of rockets. Although rockets are long compared to their diameter, they consist of several short fuel tanks and stages that are connected by short intertanks or interstages. For example, the length-to-diameter ratios of the intertanks/interstages of Saturn V, the external tank of the Space Shuttle, Ares V Heavy, and Delta IV are 0.66, 0.82, 1.35, and 1.80, respectively (NASA, 1968; Lockheed Martin Company, 2009; Sleight et al., 2011; United Launch Alliance, 2009). Recently, the NASA Shell Buckling Knockdown Factor project performed buckling tests on three full-scale cylindrical shells with length-to-diameter ratios of 0.75 and 0.73 in order

to obtain new knockdown factors for the Space Launch System (Hilburger, 2012; Hilburger et al., 2012b). Therefore, many practical cylindrical shells under axial compression have length-to-diameter ratios ranging approximately from 0.6 to 2. The length-to-diameter ratio is commonly chosen to be one for small-scale shells for research; see for example Arbocz and Babcock Jr (1968), Davis (1982), and Hilburger et al. (2006). The length-to-diameter ratio is one for most shells in the present study. Longer shells will also be briefly discussed in Section 3.6.

The dimensions presented in Table 3.2 were chosen, for practical considerations. More details for the reasons of choosing the following these dimensions will be presented in Chapter 4.

Table 3.2: Dimensions of wavy shell designs

Thickness, t	180 μm
Radius, R	35 mm
Length L	70 mm
Maximum deviation from circle, Δr	1.5 mm

A symmetric six-ply laminate, $[+60°, -60°, 0°]_s$ was adopted, where the 0° direction of the laminate is in the axial direction of the shell. It consisted of 30 μm thick unidirectional laminae of T800 carbon fibers and ThinPreg 120EPHTg-402 epoxy, provided by the North Thin Ply Technology company, with a fiber volume fraction of approximately 50%. The following lamina properties were measured: $E_1 = 127.9$ GPa, $E_2 = 6.49$ GPa, $G_{12} = 7.62$ GPa, and $\nu_{12} = 0.354$, where E_1 is the modulus along the fiber direction.

The stiffness of a composite plate or shallow shell can be described by the "ABD" matrix (Daniel and Ishai, 2006):

$$\left(\begin{bmatrix} A_{xx} & A_{xy} & A_{xs} & B_{xx} & B_{xy} & B_{xs} \\ A_{yx} & A_{yy} & A_{ys} & B_{yx} & B_{yy} & B_{ys} \\ A_{sx} & A_{sy} & A_{ss} & B_{sx} & B_{sy} & B_{ss} \\ B_{xx} & B_{xy} & B_{xs} & D_{xx} & D_{xy} & D_{xs} \\ B_{yx} & B_{yy} & B_{ys} & D_{yx} & D_{yy} & D_{ys} \\ B_{sx} & B_{sy} & B_{ss} & D_{sx} & D_{sy} & D_{ss} \end{bmatrix}\right) \begin{bmatrix} \epsilon_x^o \\ \epsilon_y^o \\ \gamma_s^o \\ \kappa_x \\ \kappa_y \\ \kappa_s \end{bmatrix} = \begin{bmatrix} N_x \\ N_y \\ N_s \\ M_x \\ M_y \\ M_s \end{bmatrix}, \tag{3.7}$$

or, in brief,

$$\left(\begin{bmatrix} A & B \\ B & D \end{bmatrix}\right) \begin{bmatrix} \epsilon^o \\ \kappa \end{bmatrix} = \begin{bmatrix} N \\ M \end{bmatrix}, \tag{3.8}$$

where ϵ^o and κ are the mid-plane strains and curvatures, respectively. N and M denote the mid-plane forces per unit length and the moments per unit length. The A matrix is the extensional stiffness matrix, relating in-plane loads to in-plane strains; the D matrix is the bending stiffness matrix, relating moments to curvatures. The B matrix couples the curvatures to the in-plane forces and the in-plane strains to the moments. Using the classical lamination theory (Daniel and Ishai, 2006), the ABD matrix of the laminate

was calculated:

$$ABD = \begin{pmatrix} 9.919 \times 10^6 & 2.670 \times 10^6 & 0 & 0 & 0 & 0 \\ 2.670 \times 10^6 & 9.919 \times 10^6 & 0 & 0 & 0 & 0 \\ 0 & 0 & 3.625 \times 10^6 & 0 & 0 & 0 \\ 0 & 0 & 0 & 0.0108 & 0.0099 & 0.0034 \\ 0 & 0 & 0 & 0.0099 & 0.0373 & 0.0081 \\ 0 & 0 & 0 & 0.0034 & 0.0081 & 0.0125 \end{pmatrix}, \tag{3.9}$$

where the units of the A and D matrices are N/m and Nm, respectively.

3.2.2 Reference Cylindrical Shell

A buckling analysis of a reference circular shell, made from the laminate selected in Section 3.2.1 and with the geometric properties defined in Table 3.2, was carried out. The assumed geometric imperfection was based on the critical buckling mode, shown in Fig. 3.5, with amplitude $\mu = t$. The buckling loads were 4.153, 1.137, and 1.137 kN, respectively, for the geometrically perfect shell and the shell with positive and negative imperfections.

The knockdown factor is calculated from

$$\gamma = \frac{\min(P_+, P_-)}{P_0} \tag{3.10}$$

which gives 0.274. The critical stress is calculated from:

$$\sigma_{cr} = \frac{\min(P_0, P_+, P_-)}{l_p t}, \tag{3.11}$$

where l_p and t are the arclength of the (wavy) center line and the thickness of the shell. Its value is 28.724 MPa.

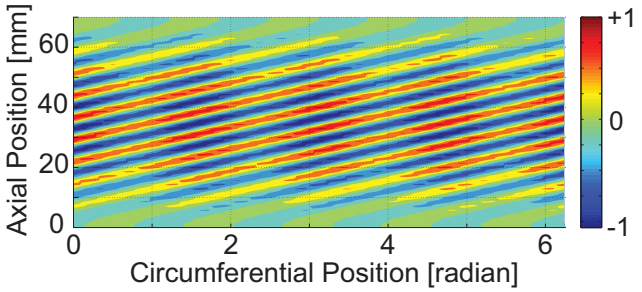

Figure 3.5: Critical buckling mode of reference (circular) cylindrical shell.

3.2.3 Mirror-Symmetric Shells

Two mirror-symmetric wavy shells with $N = 11, 16$ were designed. The optimization was first run for the case $N = 16$ and, since this initial run had converged long before the 150th generation, all other optimizations were also run for 150 generations. The evolution of the buckling loads (divided by the buckling load of the perfect, reference cylindrical shell) for the perfect and imperfect candidate designs for these two cases is shown in Fig. 3.6. An optimum design for the case $N = 11$ occurred at the 66th generation, with buckling loads of 11.017, 10.145, and 11.420 kN, respectively, for the perfect shell and the imperfect shells with positive and negative imperfections. The optimum for the case $N = 16$ occurred at the 126th generation, with buckling loads of 14.981, 14.908, and 14.897 kN, respectively.

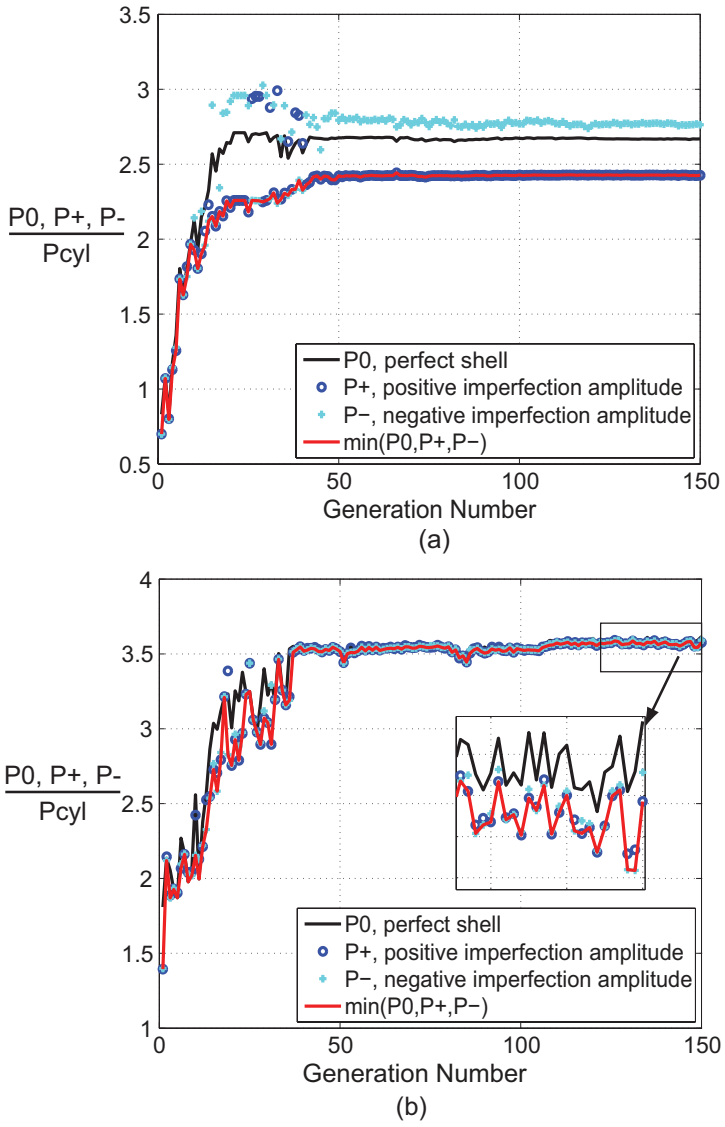

Figure 3.6: Evolution of buckling loads for mirror-symmetric wavy shells with (a) $N = 11$ and (b) $N = 16$. The loads are normalized by the buckling load of the perfect, reference cylindrical shell.

Note that in Fig. 3.6(a) P_- is almost always larger than P_0, which is in turn larger than P_+, suggesting that the majority of candidate designs considered during this optimization behave according to Case I in Fig. 2.3. Also note in the enlargement of Fig. 3.6(b) that after the 37th generation the candidate designs have slightly lower buckling loads for the imperfect cases than for the perfect shell, indicating that in this case the candidate designs behave according to Case II.

The cross-sections obtained for the two cases are shown in Fig. 3.7, and the optimal radial positions of the control points are presented in Table 3.3.

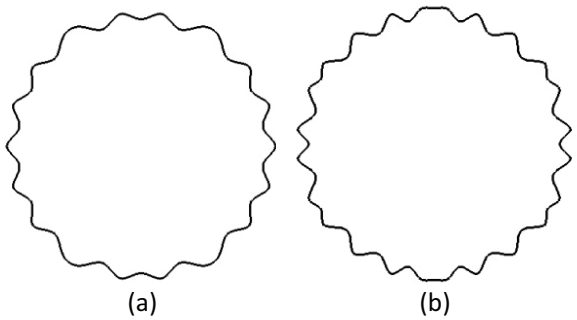

Figure 3.7: Cross-sections of mirror-symmetric wavy shells with (a) $N = 11$ and (b) $N = 16$.

Table 3.3: Radial deviations, $r_i - R$, (in mm) of control points of mirror-symmetric shells.

Point	1	2	3	4	5	6	7	8	9	10	11	12	13	14	15	16
N=11	1.5	-1.5	1.5	-1.5	1.5	-1.5	1.5	1.5	-1.5	1.5	0					
N=16	-1.5	1.5	-1.5	-1.5	1.5	0	1.5	-1.5	-1.5	1.4	-1.5	-1.2	1.5	-1.5	1.1	1.4

The knockdown factor is calculated from Eq. 3.10, which gives 0.921 and 0.994 for the cases $N = 11, 16$, respectively. The critical stress is calculated from Eq. 3.11, which gives 224.639 and 310.494 MPa, respectively, for $N = 11, 16$.

3.2.4 4-Fold Symmetric Shells

4-fold symmetric wavy shells were also designed. These designs are also denoted as $N = 11, 16$, although the actual numbers of independent control points used in the optimization were in fact $10, 15$, respectively, as explained in Section 3.1.1.

The evolution of the buckling loads is plotted in Fig. 3.8 where it can be seen that both cases converge to the Case II buckling. The best design for the case $N = 11$ was obtained at the 49th generation, with buckling loads of 10.587, 9.325, and 9.310 kN for the perfect shell and for imperfect shells with positive and negative imperfections, respectively. The best design for the case $N = 16$ was obtained at the 127th generation, with buckling loads of 13.609, 13.534, and 13.536 kN, respectively. The knockdown factors for the two cases were 0.879 and 0.994 and the corresponding critical stresses 208.224 and 281.712 MPa.

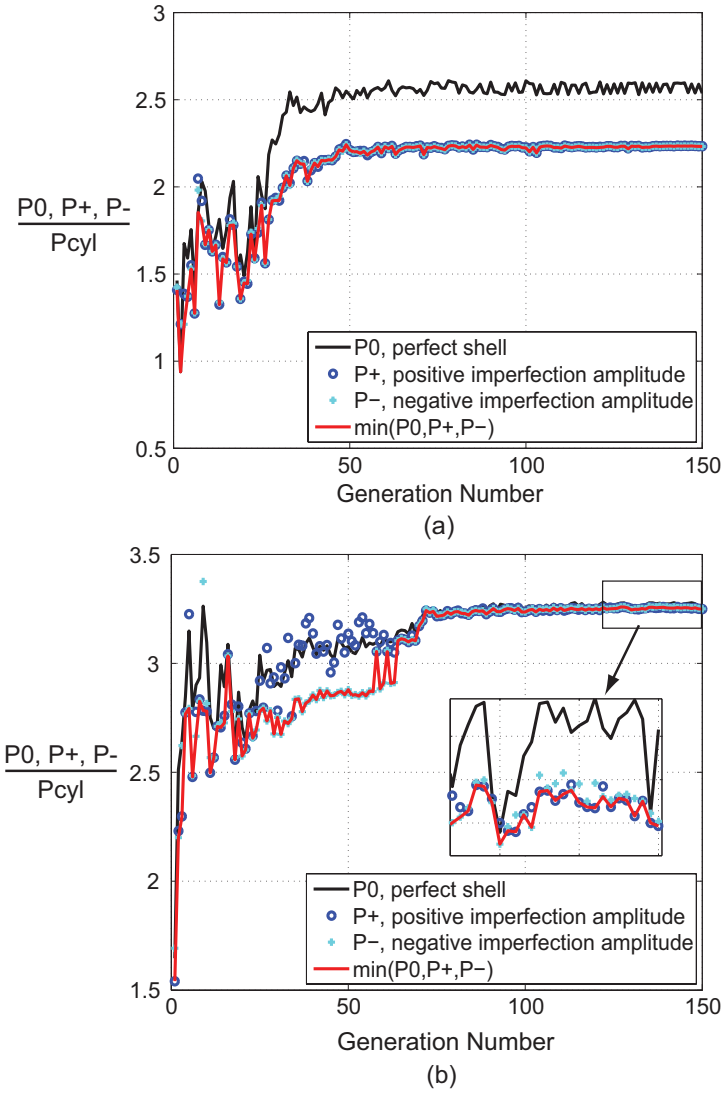

Figure 3.8: Evolution of buckling loads for 4-fold symmetric wavy shells with (a) $N = 11$ and (b) $N = 16$. For the case $N = 16$ $P_{\pm}$ is slightly lower than P_0 after the 72nd generation. The loads are normalized by the buckling load of the perfect, reference cylindrical shell.

Figure 3.9 shows the cross-sections of the two 4-fold symmetric cross-sections obtained from this study. The optimal radial deviations of the control points from the reference circle are presented in Table 3.4.

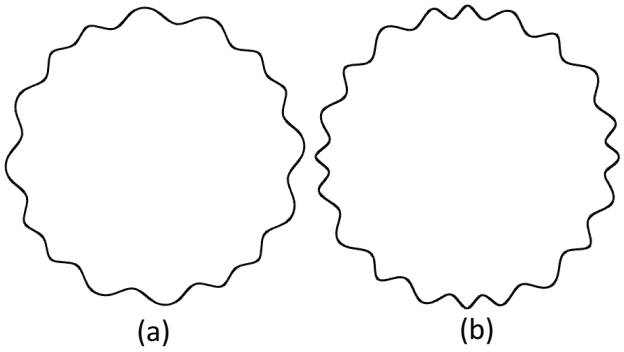

Figure 3.9: Cross-sections of 4-fold symmetric wavy shells with (a) $N = 11$ and (b) $N = 16$.

Table 3.4: Radial deviations of control points, $r_i - R$, (in mm) of 4-fold symmetric shells.

Point	1	2	3	4	5	6	7	8	9	10	11	12	13	14	15	16
N=11	1.5	1.5	-1.5	1.5	0	1.5	-1.5	1.5	1.3	-1.5	1.5					
N=16	1.5	-1.5	1.5	0	-1.5	1.4	1.5	-1.5	-1.5	1.4	-1.5	-1.5	1.5	0	-1.5	1.5

3.3 Comparison and Analysis of Wavy Shell Designs

Starting with a comparison of the predicted performance of the four shell designs obtained in the previous section, a deeper insight into the proposed approach is then obtained by considering the component wavelengths of each design. Also, an analysis of the effects of increasing the amplitude of imperfections in wavy cylinders confirms the robustness of the present approach.

3.3.1 Comparison

The knockdown factor and the critical stress for each wavy shell design presented in Sections 3.2.3-3.2.4, calculated from Eqs. 3.10-3.11, are presented in Table 3.5.

Table 3.5: Length of center line, knockdown factor, and critical stress for 180 μm thick carbon-fiber composite shells with reference radius of 35 mm.

Symmetry	N	l_p [mm]	γ	σ_{cr} [MPa]
Mirror	11	250.897	0.921	224.639
	16	266.547	0.994	310.494
4-Fold	11	248.373	0.879	208.244
	16	266.900	0.994	281.712
Circular	N/A	219.911	0.274	28.724

Note that the knockdown factor and the critical stress of the mirror-symmetric shell with $N = 16$ are

respectively 7.9% and 38.2% higher than for the shell with $N = 11$ and the same type of symmetry; for 4-fold symmetric shells, these values increase respectively by 13.1% and 35.3% when N is increased from 11 to 16. These results show that increasing the number of control points leads to decreased imperfection-sensitivity and improved critical stresses. Compared with mirror-symmetric wavy shells, 4-fold symmetric wavy shells have lower critical stresses and smaller or equal knockdown factors, suggesting that mirror symmetry is a better choice.

Compared to the reference circular shell presented in Section 3.2.2, the critical stress of the best wavy shell design ($N = 16$ and mirror-symmetric) is 981% higher and the knockdown factor is 263% higher. This result indicates that the introduction of wavy cross-sections has dramatically reduced imperfection-sensitivity, and the critical stress has also been significantly improved.

3.3.2 Analysis of Shell Cross-Sections

A better understanding of the wavy shell designs generated in Sections 3.2.3-3.2.4 can be obtained by decomposing each cross-section profile into a series of periodic waveforms. We used the Fast Fourier Transform function in Matlab to compute these components, to obtain the coefficients of the decomposition:

$$A(k) = \sum_{n=0}^{m-1} a_n e^{-i2\pi k \frac{n}{m}}, \ k = 0, 1, \ 2, \ ..., \ m-1 \tag{3.12}$$

where k is the wave number and m is the number of sampling points, chosen as 1000. a_n is the radial deviation of the n^{th} sample point from the reference circle:

$$a_n = r_n - R. \tag{3.13}$$

The results are plotted in Figs 3.10-3.11, for the range $k = 0, 1, \ldots, 49$.

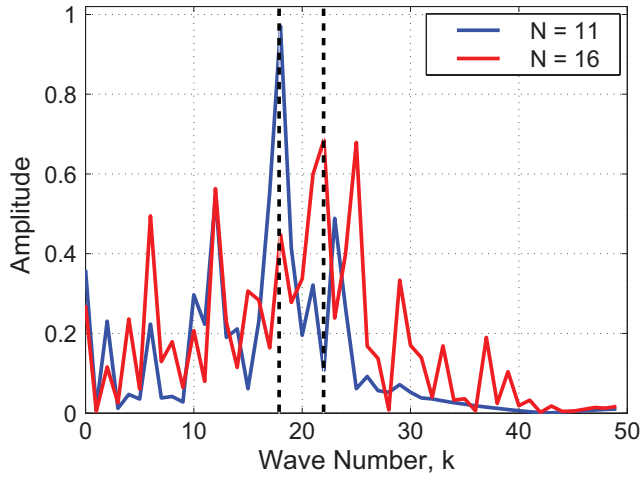

Figure 3.10: Components of mirror-symmetric wavy shells.

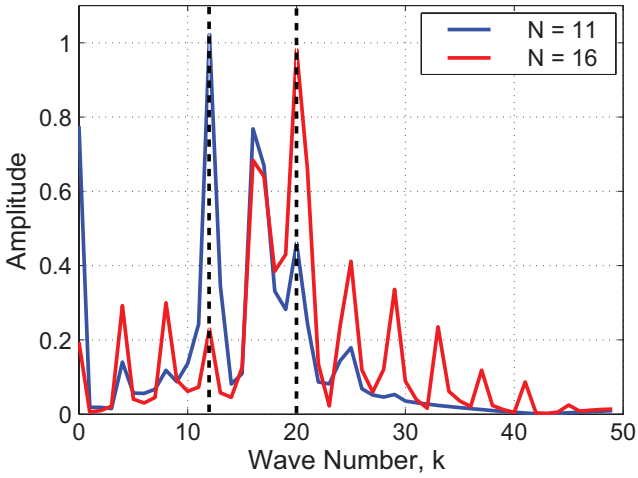

Figure 3.11: Components of 4-fold symmetric wavy shells.

Comparisons between different designs can be made more easily if we define the *peak wave number*, equal to the wave number k corresponding to the maximum amplitude $A(k)$, and the *bandwidth* of the distribution. equal to the maximum wave number whose amplitude is no less than 10% of the amplitude of the peak component. It can be noted in Figs 3.10-3.11 that both the peak wave number and the bandwidth increase as the number of control points is increased from $N = 11$ to $N = 16$.

The peak wave number and the bandwidth of all wavy shells obtained in the present study are presented in Table 3.6. These results, along with the knockdown factors and the critical stresses in Table 3.5, indicate that higher peak wave numbers and wider bandwidths tend to lead to higher critical stresses and knockdown factors. The spatial component distributions for each particular type of symmetry show that the shell designs with the largest knockdown factor and critical stress tend to have several components with large amplitudes rather than a single peak, suggesting that an optimal combination of several different components is desirable.

Table 3.6: Peak wave number and bandwidth of wavy cylinder designs.

Symmetry	N	Peak Wave Number	Bandwidth
Mirror	11	18	23
	16	22	39
4-Fold	11	12	25
	16	20	37

3.3.3 Effects of Imperfection Amplitude

In the previous optimization study the amplitude of the imperfections was assumed to be equal to one shell thickness. Because there are many factors that affect this parameter (Singer et al., 2002b), and even recent studies (Hilburger et al., 2006) have reported imperfections larger than t, it is desirable to study the effects of a range of imperfection amplitudes.

Instead of re-running the optimization study with different imperfection amplitudes, we took the wavy shell geometries obtained in Section 3.2, superposed the critical-buckling-mode imperfection with amplitudes of $\pm 0.5t$, $\pm 2t$ on the perfect geometry, and calculated the corresponding buckling loads, $P_{\pm}$, using the Riks solver in Abaqus/Standard. Equation 3.10 was then applied to calculate the knockdown factors for these shells and the results are presented in Table 3.7. The general data shown by the data is that the knockdown factor decreases when μ increases. The reduction is largest for the mirror-symmetric shell with $N = 11$ for which the knockdown factor decreases by 11.13% for μ increasing from $0.5t$ to $2t$, so this particular design is rather sensitive to the imperfection amplitude. However, for the other three designs the reduction is quite small. In particular, note that both designs with $N = 16$ show a reduction of only 2% for μ increasing from $0.5t$ to $2t$.

Table 3.7: Sensitivity of knockdown factors to imperfection amplitude.

Symmetry	N	$\mu = 0.5t$	$\mu = t$	$\mu = 2t$	Overall Reduction %
Mirror	11	0.952	0.921	0.846	11.13
	16	0.999	0.994	0.979	2.00
4-Fold	11	0.908	0.879	0.854	5.95
	16	0.997	0.994	0.977	2.01

3.4 Comparison to Alternative Shell Designs

Here we compare the symmetry-breaking cross-section designs obtained in Section 3.2 with alternative designs, based either on a sinusoidally corrugated shape or on the fluted shape of the Aster shell.

3.4.1 Sinusoidally Corrugated Shells

Shells with a periodic cross-section were obtained by superposing a sinusoidal wave on the reference circle:

$$r(\theta) = R + \Delta r \sin(k\theta), \tag{3.14}$$

where k is the total number of waves and Δr their amplitude. The dimensions and material properties of the shell were unchanged from Section 3.2.

The buckling loads of sinusoidally corrugated shells with three different amplitudes of the corrugation, Δr, and a *perfect geometry* are plotted in Fig. 3.12. The trend is that the buckling load increases as the wave amplitude increases beyond a transition number of waves, k, and the transition occurs at smaller values of k for larger Δr's.

Both *perfect and imperfect* sinusoidally corrugated shells were also analyzed for the case $\Delta r = 1.5$ mm, which coincides with the maximum deviation from the reference circle allowed in Section 3.2. As in Sec-

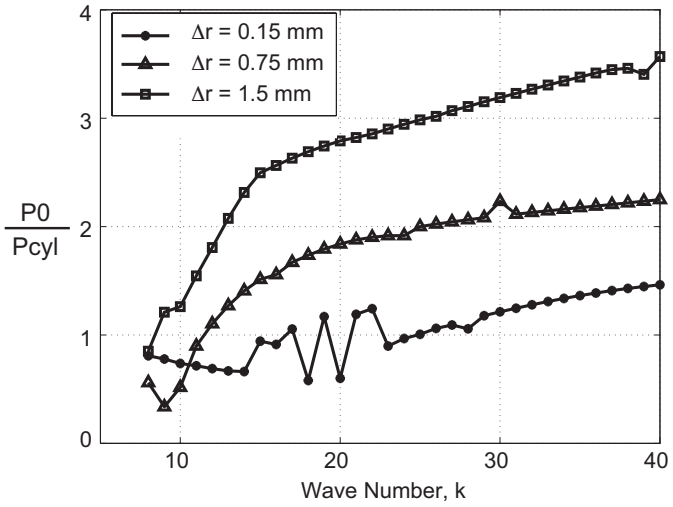

Figure 3.12: Buckling loads of geometrically perfect sinusoidally corrugated shells with corrugations of three different amplitudes.

tion 3.2, the geometry of the imperfect shells was obtained by superposing the scaled critical buckling mode on the perfect geometry:

$$C_{\pm}(k) = C_0(k) \pm \mu\Phi, \tag{3.15}$$

where $C_0(k)$ and $C_{\pm}(k)$ are the shapes of the perfect and imperfect shells, respectively; Φ is the critical eigenmode obtained from a linear eigenvalue analysis, and the amplitude of the imperfection $\mu = t$. The buckling loads of the perfect and imperfect shells, P_0 and $P_{\pm}$, were obtained, as before, from non-linear arc-length controlled simulations, for sinusoidal shells with $k = 8, \ldots, 40$.

Then the knockdown factor and the critical stress for each value of k were calculated from Eqs 3.10-3.11; their values are plotted in Fig. 3.13. The plot of knockdown factors, Fig. 3.13(a), shows an initial region of rapid increase as k increases from 8 to ≈ 10, followed by a dip and a region of much less rapid increase for $k > 15$. The plot of critical stress, Fig. 3.13(b), shows a rapid increase in the range $k = (8, 15)$, followed by an asymptotic increase toward 220 MPa. Together, these plots indicate that, for the specific case $R = 35$ mm that is being considered, sinusoidally corrugated shells with around 10 corrugations are effective in decreasing the imperfection sensitivity; however, there is a diminishing return for further increasing the number of corrugations. In fact, it will be seen in Section 3.5 that the mass efficiency actually begins to slightly decrease beyond $k \approx 15$.

The knockdown factor and the critical stress of the wavy shells in Section 3.2 are also plotted in Fig. 3.13, using in each case the peak wave number as the characteristic value of k. These plots show that the wavy shell designs are significantly more effective in increasing both values. However, it should be noted that the sinusoidal shells require only two design variables (wave number and amplitude), leading to simpler designs and potential simplification in manufacturing than the proposed wavy shells. Figure 3.13(b) shows a significant increase in the critical stress as the number of control points is increased from 11 to 16. It would

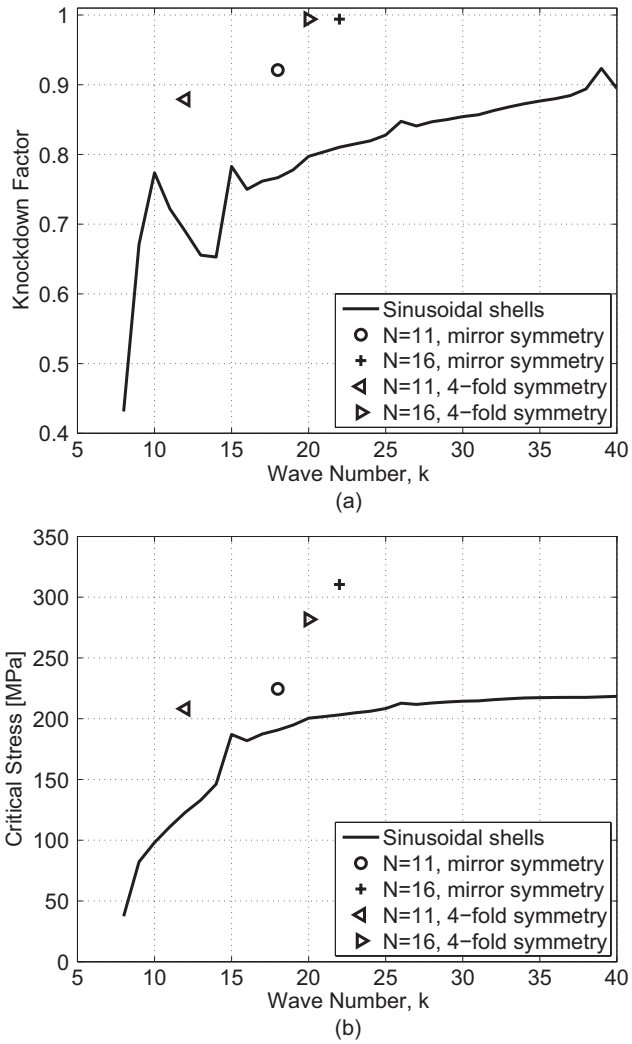

Figure 3.13: Comparison of (a) knockdown factor and (b) critical stress of sinusoidally-corrugated shells and wavy shell designs obtained in Sections 3.2.3-3.2.4.

be interesting to further explore this trend and establish at what value of N a limit may be reached.

A comparison of the critical buckling modes of the different shell designs that have been considered provides further insights. At $k = 15$ the critical mode of sinusoidally corrugated shells switches from a helical sequence of inward and outward dimples (Fig. 3.14(a)) to much larger, circumferentially arranged inward dimples with axial wavelength equal to the length of the shell (Fig. 3.14(b)). This switch marks the change in behavior that has been highlighted by the two different trends seen in Fig. 3.13.

Figure 3.15 shows the critical buckling mode of the mirror-symmetric wavy shell with $N = 16$. In this case the mode is localized along a narrow axial strip.

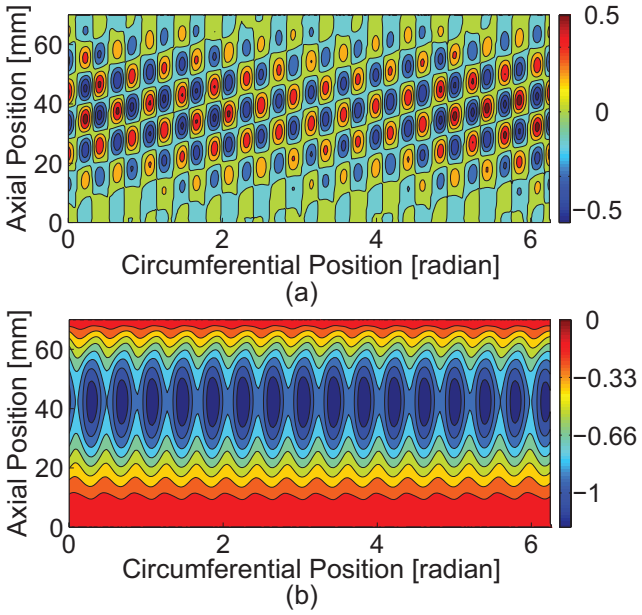

Figure 3.14: Typical critical buckling modes of sinusoidally corrugated shells with (a) $k \leq 15$ and (b) $k > 15$.

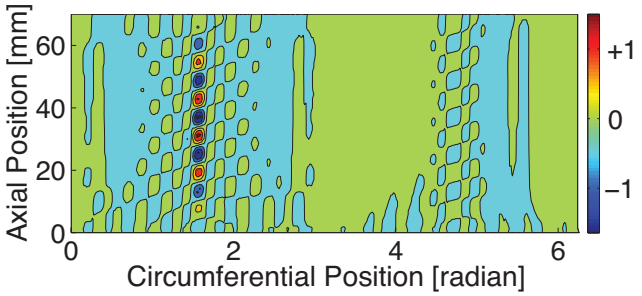

Figure 3.15: Critical buckling mode of mirror-symmetric wavy shell with $N = 16$.

These results suggest that the optimized behavior achieved in our best designs is related to the symmetry-breaking feature of the wavy cross-sections, which delays the transition of local buckling modes into global modes.

3.4.2 Aster Shell

The Aster shell, described in Section 2.1.1.4, was the first imperfection-insensitive corrugated shell design to be tested experimentally. Jullien and Araar (1991) designed, built, and tested a nickel shell with 22 corrugations and radius, length, and thickness given by R=75 mm, L=120 mm, and t=153 μm. A reference circular cylindrical shell with thickness of 150 μm was also built and tested. The values of the modulus and Poisson's ratio of these nickel shells, provided in Araar (1990), are $E = 162$ GPa, $\nu = 0.3$. Both shells were clamped at the ends and tested under axial compression; the measured buckling loads were 14.2 kN and 11.0 kN, respectively, for the Aster shell and the circular shell.

A study of the buckling loads of both structures was carried out using the same approach used throughout this thesis: namely, an imperfection based on the critical buckling mode scaled to an amplitude of one thickness was applied in a geometrically non-linear, arc-length controlled simulation to estimate the limit load. In this way, estimates were obtained for the buckling loads of the geometrically perfect structures, and also for imperfect structures with imperfections of both positive and negative signs. The resulting sets of values were 18.328, 16.405, and 16.418 kN for the Aster shell and 14.606, 5.295, and 5.294 kN for the circular cylinder; these values were used to estimate the theoretical knockdown factor from Eq. 3.10 and the theoretical critical stress from Eq. 3.11. The values obtained in this way are presented in Table 3.8. Note that the "simulation" results were obtained by the author of the thesis and the "Test" results were obtained by Jullien and Araar (1991).

A competing wavy cylinder design with a mirror-symmetric cross-section with $N = 11$ control points was obtained, considering the best set of P_0, P_+, and P_-. The maximum allowed deviation from the reference circle was $\Delta r = 3$ mm. The CMA-ES algorithm was run with 8 individuals in each generation and, the analysis was run for 150 generations. The knockdown factors and critical stresses for this new design are shown in Table 3.8, in the column labelled "Simulation". This design was not tested experimentally and hence in the table there is no corresponding value under "Test".

Table 3.8: Knockdown factors and critical stresses for circular shell, Aster shell, and wavy shell, all made of nickel.

Shells	Knockdown Factor		Critical Stress [MPa]	
	Simulation	Test	Simulation	Test
Circular	0.362	0.753	74.895	155.618
Aster	0.895	0.774	216.174	187.118
Wavy	0.948	N/A	246.146	N/A

The critical stress values presented in Table 3.8 require some explanation. First, it can be seen that the "Test" value of the knockdown factor for the circular shell is unusually high, and in fact much higher than our estimate in the "Simulation" column. This suggests that the cylindrical shell was built very accurately, as confirmed by the measured imperfection amplitude of $0.1t$ (Araar, 1990). Second, the "Test" value of the knockdown factor for the Aster shell was 14% lower than the expected value in the "Simulation" column.

This suggests that that there were significant imperfections in the as-built Aster shell, which is confirmed by the measured imperfection amplitude of $\sim 3t$ (Araar, 1990). Third, a comparison of the "Simulation" values of the knockdown factor for the Aster shell and our wavy shell design shows a 6% increase, even for a wavy shell design with only $N = 11$. In conclusion, this comparison indicates that Aster shells are difficult to build accurately and in any case our present design approach has even greater potential of eliminating imperfection sensitivity.

3.5 Mass Efficiency

A rational comparison between different architectures for cylindrical shell structures can be made in terms of the weight and load indices introduced in Section 2.1.1.5. For circular cylinders the relationship between weight index and load index is provided by Eq. 2.9. For general cylindrical shells subject to axial compression, the relationship has the form:

$$\frac{W}{AR} = \frac{1}{\sqrt{\eta}}\sqrt{\frac{N_x}{R}} \tag{3.16}$$

where η is defined as the *efficiency factor* of the shell. Note that a larger value of η results in a higher load index for the same weight index.

The efficiency factor for monocoque cylindrical shells is obtained by comparing Eq. 3.16 with Eq. 2.9, and hence is given by:

$$\eta = \frac{\gamma E}{\rho^2\sqrt{3(1-\nu^2)}} \tag{3.17}$$

Equation 3.16 plots as a straight line of slope 0.5 in the log-log plot of weight index vs. load index, first shown in Fig. 2.8. Shells of equal efficiency lie on the same line, and therefore lines of slope 0.5 in this plot are called *iso-efficiency lines*.

Figure 3.16 is a revised version of Fig. 2.8 that shows, in addition to the original data, several results of the present study. The mirror-symmetric wavy shell with $N = 16$, which is the most efficient wavy shell design obtained so far, is shown in this plot together with its (dotted) iso-efficiency line. The mass of this wavy shell is 5.1 grams, which is computed based on the measured density of the composite material, 1,510 kg/m^3. The efficiency factor for this design is 4.05 times that of perfect aluminum monocoque shells, and it can be seen in the plot that there are only three data points to the right of this line. Therefore, there are only three stiffened shells that beat the design $N = 16$: the fact that this design has higher efficiency than most existing stiffened shells is remarkable.

Several sinusoidally corrugated shells have also been included in Fig. 3.16. It is interesting to note that the data points corresponding to $k = 8, 10, 15$ go horizontally from left to right, but points corresponding to larger values of k lie on an iso-efficiency line and points corresponding to even larger values of N are further away from the line. It was already observed in Section 3.4.1 that there is a diminishing return in increasing

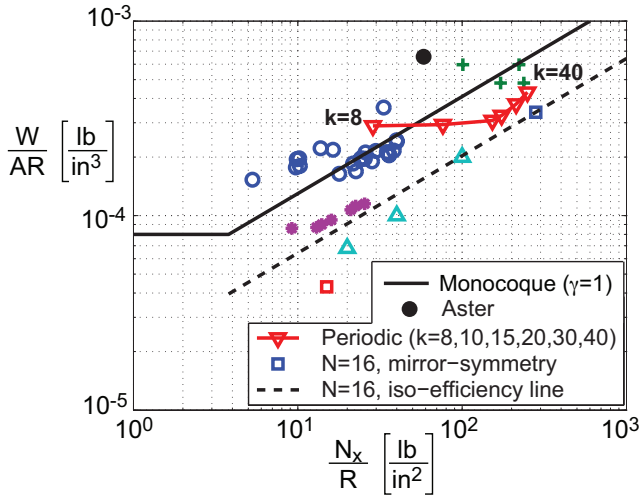

Figure 3.16: Revised version of Fig. 2.8 showing additional data points corresponding to mirror-symmetric wavy shell design with $N = 16$, sinusoidally corrugated shells, and Aster shell.

k beyond 15, but it has now been shown that beyond $k = 15$ the mass efficiency actually begins to decrease.

3.6 Effects of Shell Length

In the previous sections the length-to-diameter ratios of the composite and nickel wavy shells were 1 and 0.8, respectively, i.e., the shells were short. This section investigates the influence of shell length on the buckling loads, modes, and knockdown factors of the wavy shells. This section is focused on composite shells. First, parametric studies of shell lengths were performed on the wavy composite shells with the optimal cross-section in Fig. 3.7 (b). Second, the method described in Section 3.1 was used to obtain an optimal composite wavy shell with length-to-diameter ratio of two.

3.6.1 Parametric Studies on Shell Lengths

The wavy cross-section in Fig. 3.7 was mirror-symmetric and obtained from an optimization with $N = 16$ control points. It was found that it was the best composite wavy shell with the length-to-diameter ratio of one in the present study. In the parametric studies the shell cross-section was unchanged and only the shell length was varied. These shells have the same material and boundary conditions as those in Section 3.2.

We used the same simulation technique as that described in Section 3.2 to obtain the buckling loads of perfect wavy shells and imperfect wavy shells with positive and negative amplitudes. The shape of imperfection was chosen to be the critical buckling mode. The buckling loads and knockdown factors are summarized in Table 3.9. The knockdown factors were computed by Eq. 3.10. In general, the buckling loads of the perfect and imperfect shells and the knockdown factors decrease as the shell length increases.

The buckling modes are shown in Fig. 3.17. The buckling mode is highly localized for the shell with L/D

Table 3.9: Buckling loads and knockdown factors of composite wavy shells with various lengths.

L/D	1	1.1	1.2	1.3	1.4	1.5	2
P_0	14.981	12.353	11.191	10.225	9.413	9.691	7.967
$\min(P_+,P_-)$	14.897	12.359	10.223	9.665	9.151	8.395	5.642
Knockdown factor	0.994	1.000	0.914	0.945	0.972	0.866	0.708

of 1.1. However, the buckling modes switch to global modes as the shell length increases, and the buckling loads and knockdown factors decrease in general. These observations conform with the previous ones in Section 3.4 that local buckling modes are more favorable than global modes.

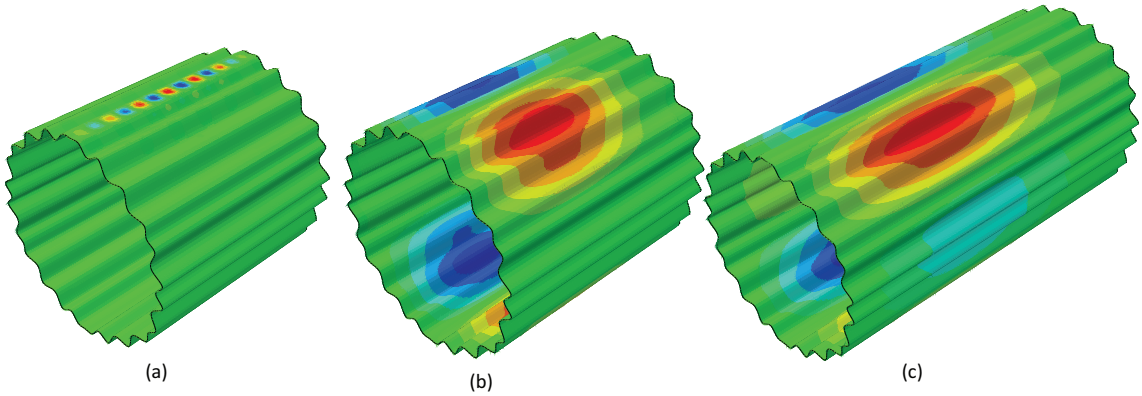

Figure 3.17: Critical buckling modes of shells with L/D of (a) 1.1, (b) 1.2, and (c) 2.

3.6.2 Optimization of Composite Shell with Length-to-Diameter Ratio of Two

In the parametric studies of the previous section the cross-section was unchanged and chosen to be the one that was optimal for the length-to-diameter ratio of one. In this section we used the method described in Section 3.1 to find the optimal cross-section for the composite shell with length-to-diameter ratio of two.

We used mirror symmetry and 16 control points to formulate shell cross-sections. The material, boundary condition, and radius in this optimization were the same as those in Section 3.2. The maximum displacement of the control points is also 1.5 mm. The shell length is twice of the diameter, i.e., $L = 140$ mm for the shells in this optimization.

The optimization was run for 125 generations and it was found that it has converged. The evolution of buckling loads during the optimization is plotted in Fig. 3.18. The optimal design was found at the 23rd generation. The buckling loads of the optimal design are 8.636 kN, 8.576 kN, and 8.577 kN for the perfect geometry, imperfect geometry with positive and negative imperfections, respectively. The knockdown factor of the optimal design is 0.993.

A reference circular cylindrical shell with the same length, diameter, material and boundary conditions as the optimal wavy shell was also analyzed. The buckling loads for the reference shell are 4.128 kN, 1.663 kN, and 1.663 kN, respectively for the perfect geometry and imperfect geometry with positive and negative

imperfections. The knockdown factor of the reference circular shell is 0.403.

The buckling load of the optimal wavy shell ($min(P_+, P_-)$) is 107.8% and 415.7% higher than the perfect and imperfect buckling loads of the reference circular shell, respectively. The knockdown factor of the optimal wavy shell is 146.4% higher than the reference circular shell. The cross-section and critical buckling mode of the optimal wavy shell are shown in Fig. 3.19. The buckling mode of the optimal design is highly localized, also confirming with the observations in the previous sections that local buckling modes are more desirable.

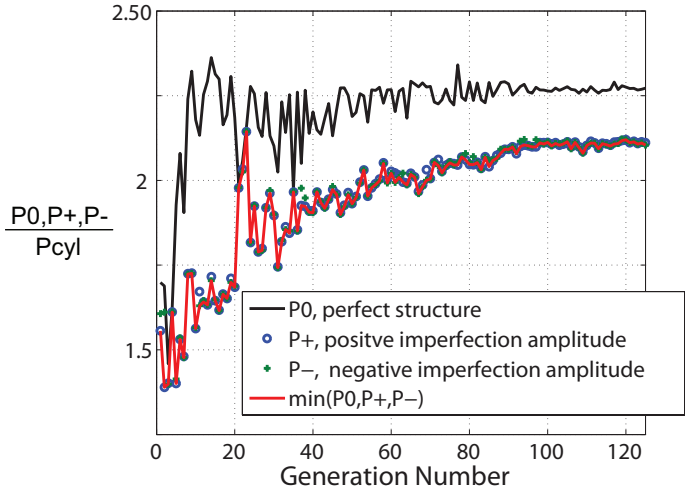

Figure 3.18: Evolution of buckling loads for mirror-symmetric shells with $N = 16$ and $L/D = 2$. The loads are normalized by the buckling load of the perfect, reference circular cylindrical shell with $L/D = 2$.

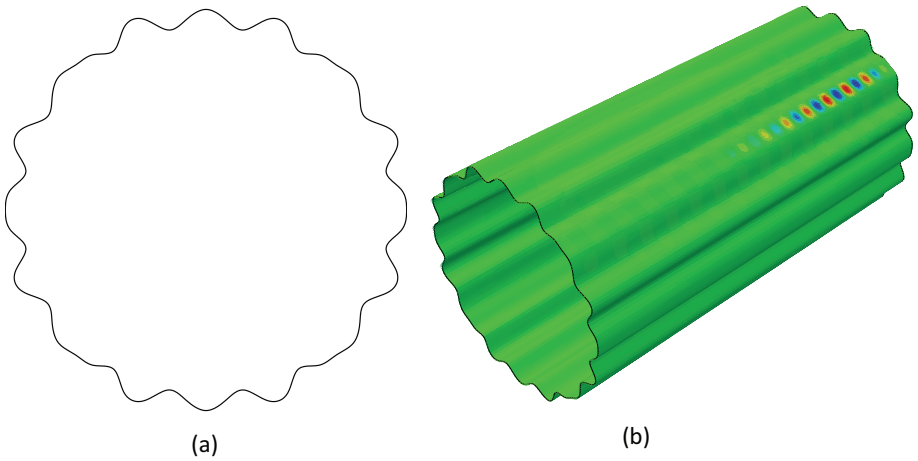

Figure 3.19: (a) Cross-section of optimal design. (b) Critical buckling mode of optimal design.

3.7 Discussion

A novel symmetry-breaking structural form for cylindrical shells subject to axial compression has been proposed and an optimization technique to obtain geometric shapes that maximize the minimum between the buckling loads of the geometrically perfect structure and geometrically imperfect structures with positive and negative imperfections has been implemented. It has been shown that shell designs developed with this approach can achieve very high critical stress while also being practically insensitive to geometric imperfections.

Note that, because the critical buckling stress of an axially loaded cylindrical panel is inversely proportional to its radius of curvature, R, through $\sigma_{cl} \approx 0.6Et/R$, the large increase in the critical buckling stress that has been achieved by changing the cross-section of the shell from circular to either wavy or sinusoidally corrugated can be simply explained by the achieved reduction in the local radius curvature of the new designs.

A highlight of the present results is our design for a mirror-symmetric composite wavy shell with 16 independent control points, which has a knockdown factor 3.6 times that of a circular cylindrical shell with the same material properties and dimensions, and a critical buckling stress 10.8 times that of the circular cylindrical shell. Another highlight is that the present approach was able to generate a wavy nickel cylinder design with knockdown factor and critical stress, respectively, 1.06 and 1.14 times those of a theoretical Aster shell based on Jullien and Araar (1991). It has also been shown that designs based on the present approach are comparable to the most efficient stiffened shell designs that have been developed during the past decades. These results appear very promising and justify further development of the proposed concept.

The composite and nickel wavy shells in this thesis show that our method is applicable for both anisotropic and isotropic materials. The composite material in the present study was chosen due to the availability of material and practical considerations of experiments. The laminate configuration, $[+60°, -60°, 0°]_s$, was fixed for all the optimizations. However, the properties of composite material can be tailored by varying the angles of fibers, offering us more design freedom. It would be interesting to add the properties of composite material in the design variables for optimizations in the future.

A comparison between the critical buckling modes of shell designs obtained from the present approach with the buckling modes of periodically corrugated shells has shown that optimized wavy cross-section designs are tuned to achieve highly localized modes, and this feature leads to superior performance. Our Fourier decompositions of each optimized cross-section into a series of periodic components indicate that wavy shells with better performance have both higher peak frequency and wider bandwidth, as well as more frequency components with larger amplitude. These results suggest that a systematic study of shell designs with increasing numbers of control points may be justified. It may lead to general trends in behavior that relate the relative magnitudes of the components with different wave numbers of the cross-section deviation from the reference circle to optimal or semi-optimal performance. These further development could then be exploited to develop future designs without going through a detailed optimization. Such follow-on work

may also be advantageous in developing scaling techniques for shells with larger diameters, and particularly those with larger values of R/t.

A challenge associated with shells with larger diameters is that they will require cross-sections with a larger number of corrugations, in order to fully achieve their efficiency potential. It is possible, of course, to apply the present analysis technique to such structures, but the number of nodes in the finite element analysis will scale linearly with the shell diameter, if the component wavelengths incorporated in the shell cross-section designs are not increased.

Two last points should be noted. First, due to the non-convexity and lack of a mathematical expression for the present optimization problem, there is no guarantee that even a state of art optimizer for non-convex problems will converge to a global minimum. We have confirmed that our optimal design for a mirror-symmetric wavy shell with $N = 16$ is a local minimum by carrying out an additional gradient-based optimization with the *fmincon* function in MATLAB that used the CMA-ES optimum as an initial value. The improvement in the buckling load was less than 0.04%. Using a larger population size for the CMA-ES could increase the probability of obtaining global minima, but at the cost of increasing the computational time. A potential method to avoid a prohibitive increase in computations is to reduce the number of parameters needed to define the shape of the cross-section. Instead of using a NURBS interpolation through N control points, the cross-section could alternatively be described in terms of its Fourier spatial components, which would require fewer parameters than the 11 or 16 control points in the present study. As a result, the number of design variables in the optimization would be reduced and the probability of finding the global optimum would be increased, without increasing the population size.

Second, the present study has made an intuitive assumption that shells with non-straight walls along axial direction were less efficient than those with uniform cross-sections in axial direction. It would be interesting to further investigate this assumption and to study shells with corrugations in both circumferential and axial directions.

Chapter 4

Validation Experiments: Imperfection-Insensitive Cylindrical Shells

This chapter presents the experimental studies on the wavy shell in Fig. 3.7 (b), which is the best composite shell obtained from the method proposed in the previous chapter. This chapter begins with a method for making composite wavy shells, followed by a method for measuring geometric imperfections. The predicted and measured experimental behavior of wavy shells under axial compression is then presented.

In the previous chapter only structural buckling was used in formulating the method for designing imperfection-insensitive cylindrical shells. This chapter considers the strength of the material in order to predict structural collapse.

4.1 Manufacture

This section presents the fabrication technique developed for wavy shells, followed by a potting technique that provides clamped boundary conditions for the wavy shells. Three composite wavy shells and two composite circular shells were made.

4.1.1 Fabrication

As discussed in Section 2.1.2.1, a composite cylindrical shell can be made from a single piece of laminate or by assembling several segments. The latter method is suitable for large shells. Therefore, the shells in the present study were made from a single piece of laminate. The wavy cross-section was obtained by laying the composite material on a wavy steel mandrel (shown in Fig. 4.1) and curing in an autoclave. The steel mandrel was made on a wire-cut EDM machine.

One of the main difficulties in making wavy shells, compared to circular cylindrical shell, was the separation of cured shells from the mandrel. To facilitate the separation, we added a layer of 12.5-micron thick

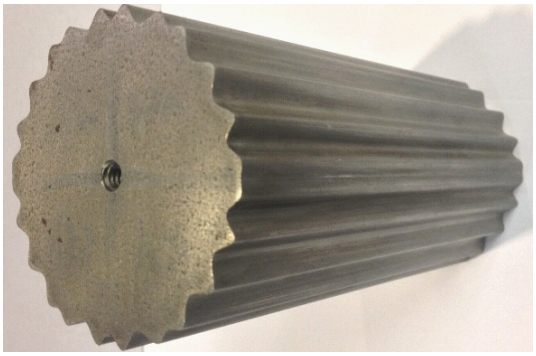

Figure 4.1: Mandrel made on a wire-cut machine.

Kapton film on the laminate, as shown in Fig. 4.2. The Kapton film remained bonded to the shell after curing; however, it was much thinner and softer than the composite material. Calculations showed that the change of buckling loads due to the Kapton film was less than 0.1%. Therefore, the influence of the Kapton film was ignored. The blue film in Fig. 4.2 was a perforated release film that helped release excessive epoxy during curing.

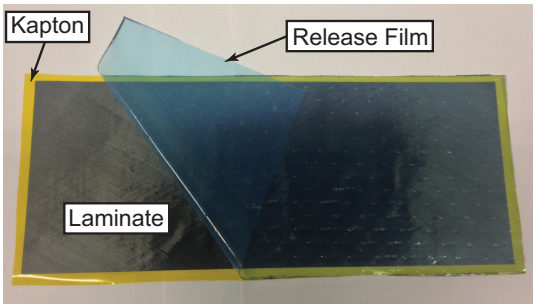

Figure 4.2: Laminate and films that facilitate release of cured shell.

We used pressure-sensitive tape to keep the laminate on the mandrel during lay-up and curing, as shown in Fig. 4.3. The complete lay-up is shown in Fig. 4.4. The mandrel, Kapton film, laminate, and release film were then covered with a breather blanket. The laminate, mandrel, and all wrapping materials were then put in a vacuum bag and cured in an autoclave. The laminate was held under vacuum through the entire curing process. Before separating the shell from the mandrel after curing, we used blade and sand paper to trim and grind the two ends of the shell to ensure that they were as flat as the two ends of the mandrel. This made the ends of the shell flat and parallel to each other. Three wavy shells were made by using this method. We also made two circular cylindrical shells that had the same length ($L = 70$ mm), radius ($R = 35$ mm), and material as the wavy shells. The composite wavy and circular shells are shown in Fig. 4.5.

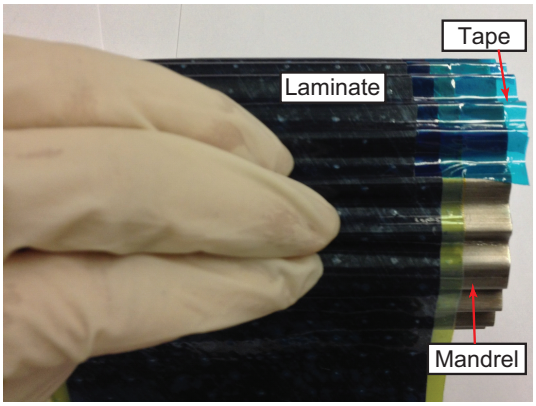

Figure 4.3: Lay-up.

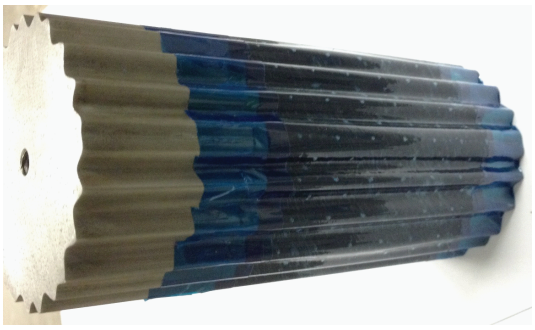

Figure 4.4: The laminate is laid up on the mandrel. This figure shows that the laminate is kept on the mandrel surface by the tape.

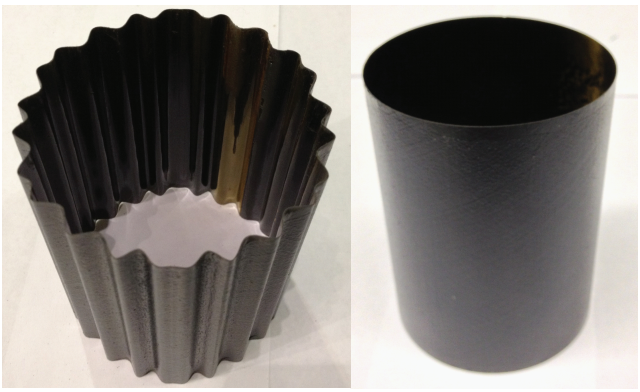

Figure 4.5: Cured composite (a) wavy shell and (b) circular shell.

4.1.2 Potting

Clamped boundary conditions were obtained by potting the shells into room temperature cured epoxy. We developed a potting technique to obtain flat and parallel potted ends to ensure proper boundary and loading conditions.

The epoxy was poured into a plastic cup with open ends held on a piece of flat glass, as shown in Fig. 4.6. The glass guaranteed that the cured epoxy has a flat bottom surface. Tapes were used to fix the plastic cup on the glass and to prevent leakage of the epoxy. The glass was covered by a layer of Frekote release agent to facilitate the removal of cured epoxy. The epoxy used was EpoxAcast 650, a mineral filled general purpose casting epoxy made by Smooth-On, Inc. It has a low shrinkage and a low mixed viscosity for minimal bubble entrapment.

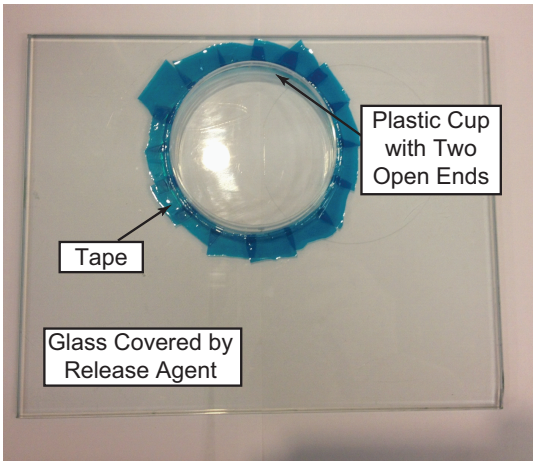

Figure 4.6: Glass and plastic cup for potting.

To avoid deformations of the shells during potting, we used a fixture consisting of a base, supporting structure, shaft, and arm (shown in Fig. 4.7), to facilitate potting. The mandrel with the shell was connect to the arm by a screw. We put the glass on the base and adjusted the glass to the horizontal position. The bottom surface of the mandrel was also adjusted to be horizontal to ensure that the axis of the mandrel and shell is perpendicular to the cured epoxy end.

The epoxy was poured into the plastic cup until its depth reached the 10 mm marker on the plastic cup. The shell was then slowly slid down into the epoxy while keeping the mandrel unmoved. This can guarantee that the shell was not deformed during the potting so that large imperfections can be avoided. It took about 6 hours for the epoxy to completely cure. After removing the shell from the mandrel, the cured epoxy base was separated from the glass and the plastic cup was also removed from the epoxy base.

Potting on the second end was done without using the mandrel. A hole was drilled on the first epoxy base so as to release the air inside the shell when potting the second end. Similar to the previous step, the glass covered by a layer of release agent was put on the fixture base, and the epoxy was poured into the plastic cup until it reached the 10 mm marker. The shell was then slowly put into the epoxy. Since both

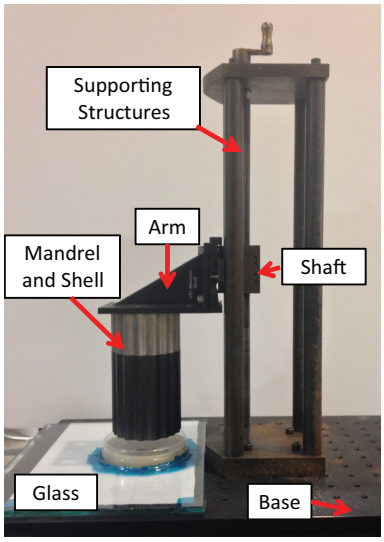

Figure 4.7: Fixture with mandrel, composite shell, flat glass, and plastic cup for potting. The epoxy has been poured in the plastic cup.

ends of the shell were trimmed and polished to be flat and parallel, the second end of the epoxy base was guaranteed to be parallel to the first end. The two circular cylindrical shells were also potted by using the above method. The shells with the two potted end are shown in Fig. 4.8.

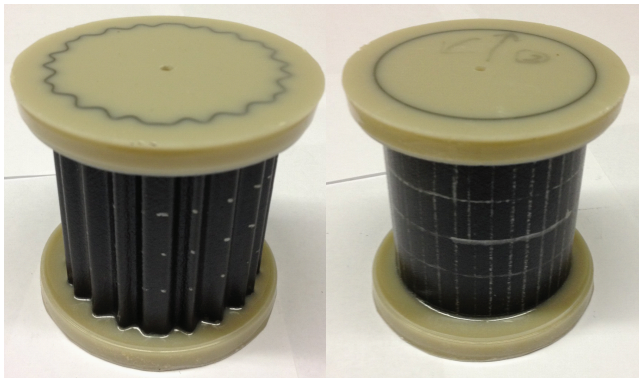

Figure 4.8: (a) Wavy shell and (b) circular shell with potted ends.

4.2 Imperfection Measurement

Although the three-dimensional survey technique is currently the main method for measuring shell imperfections, it is not feasible for our wavy shells due to two reasons. First, since our shells are very small and there are small corrugations on the surfaces, a very small scanning probe is required in order to scan the complete shell surface. Second, the pressure applied by the probe may introduce deformations, resulting in inaccurate measurements. Therefore, we have developed a non-contact photogrammetry technique to measure the shell

imperfections. This section presents the methods and results of imperfection measurements.

4.2.1 Method of Imperfection Measurement

The commercial photogrammetry software Photomodeler 6 EosSystems (2004) was used with two types of targets. Coded targets are black circular spots surrounded by black segments of rings, as seen in Fig. 4.9. The shape of these rings was non-repetitive such that each coded target can be uniquely detected by the software. The coded targets were attached to the top and lateral surfaces of the cured epoxy base. Non-coded targets were regular dots projected onto the shell surface by means of an LCD projector. A very thin layer of white paint was sprayed on the shell surface to facilitate the detection of the non-coded targets.

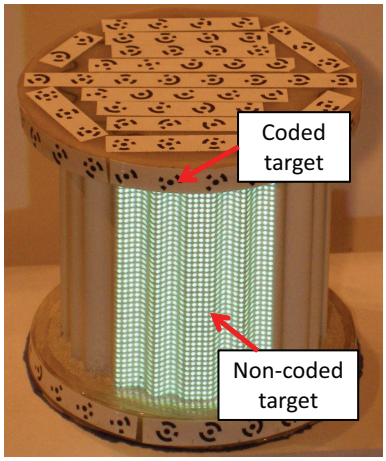

Figure 4.9: Coded and non-coded targets.

The setup for measuring the shell geometry is shown in Fig. 4.10. There are four steps involved in a measurement. In the first step the coded targets were photographed and correlated to define a global coordinate system. Only one camera was used in this step, and it was higher than the shell so as to record the targets on the top surface of the epoxy base. The shells were rotated between 18 and 23 times such that all coded targets can be photographed by the camera. The photos were processed with Photomodeler 6. All photos included the coded targets on the top surface of the epoxy base, to act as fiducials in the final correlation of all data. Three non-collinear coded targets on the top surface were picked to define the $o - x - y$ plane, and the distance between two of these points provided a scale for the measurements.

The second step obtained the positions of the non-coded targets projected on the shell surface. We used three cameras pointed in different directions to photograph the shell surface, as shown in Fig. 4.10. Photomodeler 6 was used to correlate the coded and non-coded targets in these three photos with all the photos taken in the first step to calculate their coordinates in the global coordinate system. We projected the non-coded targets onto a narrow rectangular area, as seen in Fig. 4.9. Therefore, the shell was rotated multiple times to obtain the complete geometry. The coordinates of the non-coded targets obtained from a measurement were exported to a text file for post-processing.

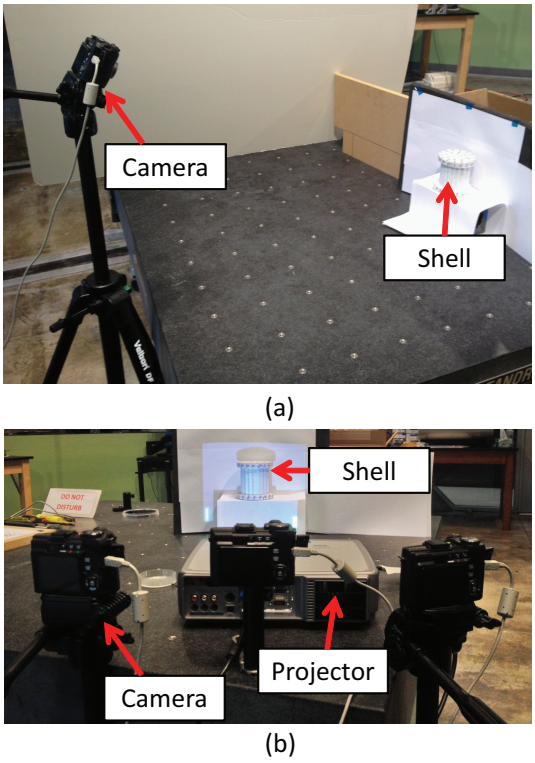

Figure 4.10: Camera setup for (a) defining a global coordinate system (step 1) and (b) measuring positions of non-coded targes (step 2)

The third step was to combine the points obtained in the previous step to obtain the complete shell surface. Rhino 3D, a CAD software package, was employed to read the text files containing the coordinates of the targets and to combine these points into a single cluster of points.

The fourth step was to compute the shell imperfections. We followed the method discussed in Section 2.1.2.2 to find the best-fit position of the measured points. A three-parameter transformation was defined in terms of translations in the x and y directions and rotation with respect to the z-axis, and the square of the distance between measured and designed shapes was computed. The coordinate transformation was determined by minimizing the square distance with Covariance Matrix Adaptation Evolution Strategy (CMA-ES):

$$\begin{aligned} \text{Minimize}: \quad & \sum_{p=1}^{N_p} e_p^2 \\ \text{Subject to}: \quad & (1) \quad |T_x| \leq 10 \text{ mm} \\ & (2) \quad |T_y| \leq 10 \text{ mm} \\ & (3) \quad |R_z| \leq \frac{\pi}{2} \end{aligned} \tag{4.1}$$

where e_p, T_x, T_y and R_z are the normal distance, translations in the x and y directions, and rotation with

respect to the z-axis, respectively. N_p denotes the total number of measured points. This process that provides the best-fit measured points is shown in Fig. 4.11. Before running the above minimization problem, we manually moved the measured cluster of points to a position close to the imaginary perfect wavy shell in order to achieve faster convergence.

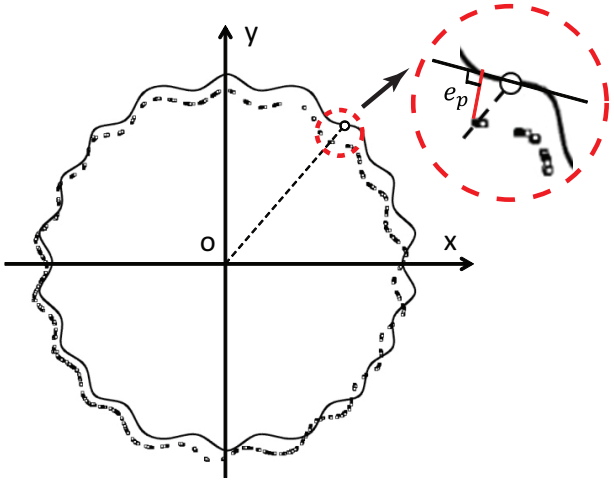

Figure 4.11: Schematic of finding the best-fit position of measured shells. e_p is the normal distance between the p^{th} measured point and the corresponding point on the perfect shell.

4.2.2 Distributions of Thickness and Mid-Plane Imperfections

The thickness distributions were measured using a micrometer before potting. We measured thickness at the heights of 0 cm, 2 cm, 5 cm and 7 cm on each hill, valley, as well as the middle points between the hill and valley of each corrugation. The thickness at the height of 3.5 cm on the middle points between the hill and valley of each corrugation was also measured. Fig. 4.12 shows the thickness distributions of the three wavy shells. The results obtained from the photogrametry measurements are outer-surface imperfections. The mid-plane imperfection was computed by subtracting the non-uniformity of thickness from the outer-surface imperfections. The mid-plane imperfections are plotted in Fig. 4.13. The imperfection amplitudes were $2.98t_{nom}$, $2.08t_{nom}$ and $2.53t_{nom}$ for wavy shells 1, 2 and 3, respectively. The mean and standard deviations for the thickness and imperfection amplitudes are listed in Table 4.1. Note that the average thicknesses of wavy shells were around 166 μm, 7.8% thinner than the nominal thickness 180 μm.

Shells	Thickness [μm]	Imperfection Amplitude [μm]	μ
Wavy shell 1	166±16	536	2.98
Wavy shell 2	166±22	374	2.08
Wavy shell 3	165±19	455	2.53

Table 4.1: Measured thickness and imperfections of circular and wavy shells. μ is the ratio between the imperfection amplitude and nominal shell thickness 180 μm.

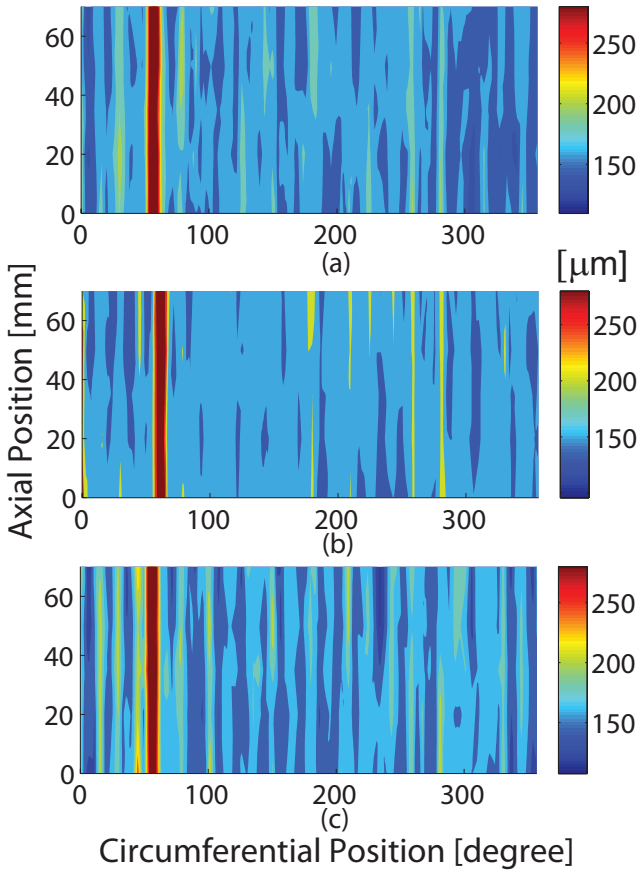

Figure 4.12: (a), (b), and (c) are thickness distributions of wavy shells 1, 2, and 3, respectively.

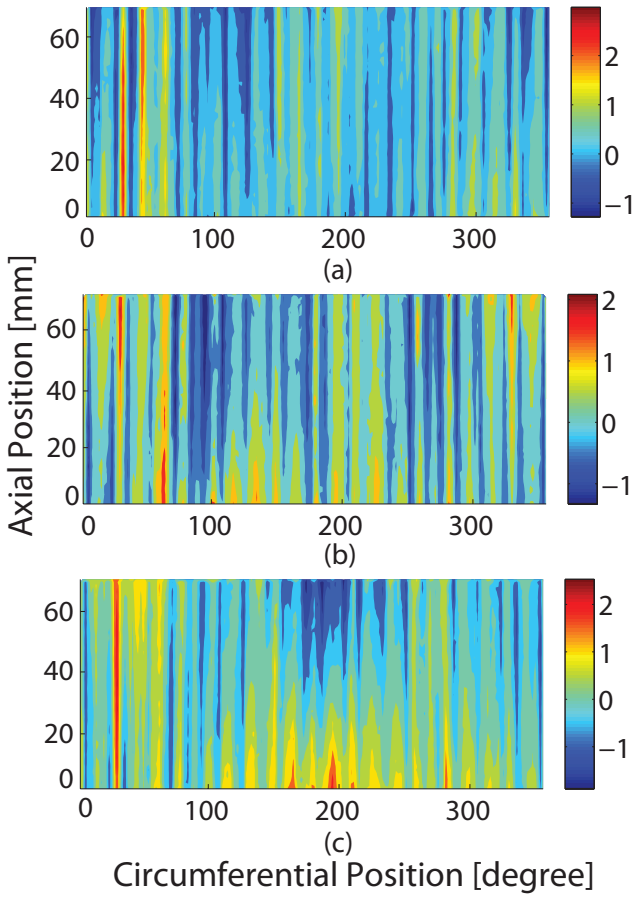

Figure 4.13: (a), (b), and (c) are mid-plane imperfection ratio (imperfection divided by nominal thickness) distributions of wavy shells 1, 2, and 3, respectively.

4.2.3 Components of Imperfections

The mid-plane imperfections in Fig. 4.13 were decomposed into half-cosine Fourier components: $\omega(x,\theta) = t_{nom}\sum_{k=0}^{M}\sum_{l=0}^{M} cos(\frac{k\pi x}{L})[A_{kl}cos(l\theta)+B_{kl}sin(l\theta)]$. The Fourier coefficients and amplitude of each component were computed by Eqs. 2.11 and 2.12. The imperfection amplitudes for components $k = 0$, $k = 1$, and $l = 0$ to $l = 50$ are plotted in Fig. 4.14. The amplitudes of $k \geq 2$ components were much smaller than $k \leq 1$, and thus they are not shown in the figure.

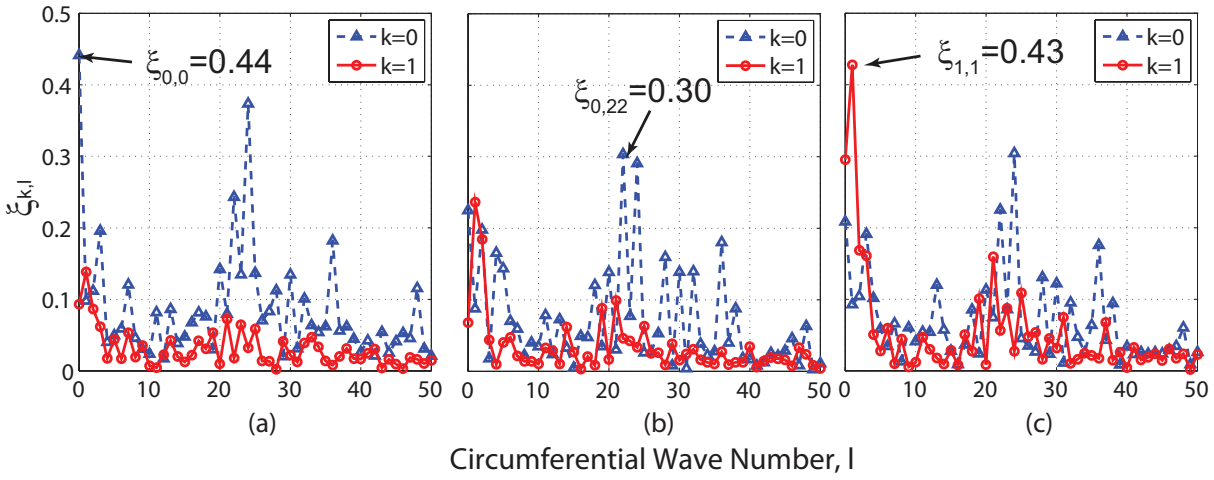

Figure 4.14: (a), (b), and (c) are the Fourier components of the mid-plane imperfections of wavy shells 1, 2, and 3, respectively.

The peak, second, and third imperfection components of wavy shell 1 are respectively $A_{0,0}$, $A_{0,24}cos(24\theta)+B_{0,24}sin(24\theta)$, and $A_{0,22}cos(22\theta)+B_{0,22}sin(22\theta)$, indicating that the major imperfection components of wavy shell 1 are uniform along the axial direction. The $k = 0$, $l = 22$ and $k = 0$, $l = 24$ components are among the largest three imperfection components of wavy shell 2. However, both wavy shell 2 and 3 have large axial half-cosine ($k = 1$) imperfections.

4.3 Predicted Behavior of Axially Loaded Wavy Shells

We predicted the behavior of wavy shells subject to axial compression based on critical-mode imperfections, measured thickness distributions, and measured mid-plane imperfections by using finite element models. The simulation methods and results are presented in this section.

4.3.1 Adjusted Material Properties

The material properties in Eq. 3.9 were computed based on the nominal shell thickness 180 μm. However, the measured average shell thickness for wavy shells was 166 μm. It is necessary to modify the ABD matrix to consider the reduction in shell thickness. We followed Ref. Hilburger and Starnes Jr (2001) which assumed

that any variations in the shell thickness resulted from a variation in epoxy volume only rather than the fiber volume and used the rule of mixture to adjust lamina properties for measured shell thickness. We derived the modified lamina properties, shown as follows:

$$\begin{aligned} V_f &= \frac{V_{f,nom}}{\alpha} \\ E_1 &= \frac{1}{\alpha} E_{1,nom} \\ E_2 &= \frac{\alpha(1-V_{f,nom})}{\alpha - V_{f,nom}} E_{2,nom} \\ G_{12} &= \frac{\alpha(1-V_{f,nom})}{\alpha - V_{f,nom}} G_{12,nom} \\ \nu_{12} &= \nu_{12,nom} \end{aligned} \tag{4.2}$$

where α is the ratio between the measured and nominal laminate thickness, and α is 0.922 for the wavy shells tested in the present study. Using the classical lamination theory, the modified ABD matrix for $\alpha = 0.922$ was calculated as:

$$ABD(\alpha = 0.922) = \begin{pmatrix} 9.928 \times 10^6 & 2.668 \times 10^6 & 0 & 0 & 0 & 0 \\ 2.668 \times 10^6 & 9.928 \times 10^6 & 0 & 0 & 0 & 0 \\ 0 & 0 & 3.630 \times 10^6 & 0 & 0 & 0 \\ 0 & 0 & 0 & 0.0093 & 0.0084 & 0.0029 \\ 0 & 0 & 0 & 0.0084 & 0.0317 & 0.0069 \\ 0 & 0 & 0 & 0.0029 & 0.0069 & 0.0106 \end{pmatrix} \tag{4.3}$$

where the units of the A and D matrices are N/m and Nm, respectively.

4.3.2 Finite Element Models

The bottom edge of the shell is fully clamped in the FEA models. The only degree of freedom of the top edge is the displacement in the axial direction. However, there are two ways to apply axial compression: uniform axial load and uniform end-shortening, as shown in Fig. 4.15. Both loading conditions were analyzed in this section. However, uniform end-shortening is considered to be a better representation of experiments than uniform axial load. Therefore, simulations based on uniform end-shortening were used to compare to the experiments.

In order to obtain the uniform end-shortening and clamped boundary condition in simulations, a rigid plate was employed and a concentrated axial load was applied to the rigid plate through a reference point as illustrated in Fig. 4.15 (b). The rigid plate can only move axially without any transverse displacements or rotations, i.e., $U_y = U_z = R_x = R_y = R_z = 0$. The top edge of the shell was constrained to the rigid plate by the "tie constraint" in the Abaqus CAE/Standard, which can guarantee that the top edge has the

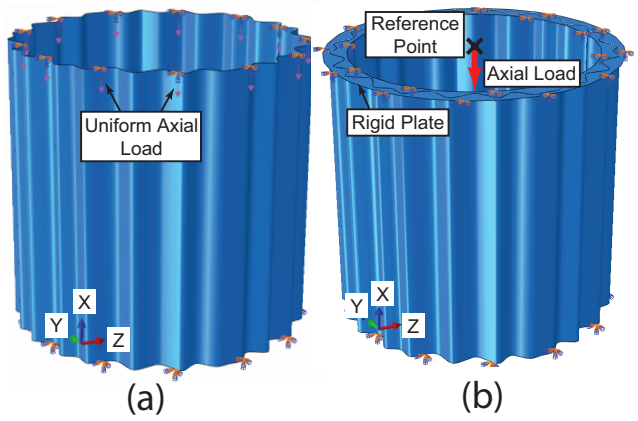

Figure 4.15: Abaqus models for (a) uniform axial load and (b) uniform end-shortening.

same translational displacements and rotations as the rigid plate. Therefore, the top edge of the shell can only move along the axial direction. The bottom edge of the shell was fully clamped, i.e., $U_x = U_y = U_z = R_x = R_y = R_z = 0$.

The buckling loads were computed by carrying out a load-displacement arc-length incrementation non-linear analysis, using the Riks solver in Abaqus CAE/standard. The first limit load of the load-displacement curve was taken as the buckling load. The increments of the axial load in the analysis were limited between 50 N and 100 N. The Abaqus models consisted of around 30,000 reduced integrated quadrilateral thin-shell S8R elements.

4.3.3 Buckling Loads Based on Uniform Thickness and Critical-Mode Imperfections

Using the measured average shell thickness 166 μm, the buckling loads of imperfect wavy shells were computed. The imperfection shape was the critical buckling mode, which was obtained by running a linear eigenvalue buckling analysis in Abaqus/Standard. The finite element model discussed in Section 4.3.2 was used. The imperfection was introduced in the finite element model by superposing the critical buckling mode on the mesh of the perfect shell and modifying the positions of its nodes in the model. Imperfections with both positive and negative amplitudes were considered.

We run simulations on both uniform axial load (Fig. 4.15 (a)) and uniform axial end-shortening (Fig. 4.15 (b)) using the modified ABD matrix in Eq. 4.3. The buckling loads of geometrically perfect shell and imperfect shells of various imperfection amplitudes are summarized in Tab. 4.2.

The buckling loads of the perfect shells subject to uniform axial load and uniform end shortening were computed as 10.461 kN and 10.437 kN, respectively. The buckling loads for those two loading conditions are very close. The knockdown factors for the shell subject to uniform axial load are at least 0.991 even for large imperfections. The buckling loads of the imperfect wavy shells subject to uniform end shortening are

	P_0 [kN]	μ	min(P_+,P_-) [kN]
Uniform axial load	10.461	2	10.378
		2.5	10.366
		3	10.392
Uniform end shortening	10.437	2	13.063
		2.5	12.983
		3	12.911

Table 4.2: Summary of computed buckling loads for the wavy shells to be tested. μ is the imperfection amplitude divided by the nominal shell thickness, $t_{nom} = 180$ μm.

higher than the perfect shell. The results obtained for both loading conditions showed that the wavy shell was not sensitive to imperfections. The uniform end-shortening can better represent the experiments, and it was used as the loading condition for all simulations showed in the following sections.

4.3.4 Buckling Loads Based on Measured Non-Uniform Thickness and Imperfection

We incorporated the measured thickness and imperfection distributions shown in Figs. 4.12 and 4.13 in finite element models to further improve the accuracy of analyses. The non-uniform thickness was introduced in the finite element models by assigning the modified local ABD matrix to the shell sections in the analyses. The shell in the FEA model was partitioned into around 600 patches. We assumed that the thickness at each patch is uniform and equal to the local average thickness within the patch. The ratio between the local average thickness and nominal thickness, α, was first computed, and the lamina properties were adjusted by Eq. 4.2. The local ABD matrix was calculated by using the classical lamination theory and then assigned to the corresponding patch in the FEA model.

The buckling loads of the imperfect shells with both non-uniform thickness and mid-plane imperfections were computed, and the results are summarized in Tab. 4.3. The buckling load of the perfect wavy shell is 10.437 kN. Therefore, the buckling loads were increased after introducing the imperfections. These results showed that the wavy shells were not sensitive to imperfections.

Shells	Non-uniform thickness + mid-plane imperfection
Wavy shell 1	13.125 kN
Wavy shell 2	12.853 kN
Wavy shell 3	12.581 kN

Table 4.3: Buckling loads based on measured thickness and mid-plane imperfection distributions.

Typical load versus end shortening curves are plotted in Fig. 4.16. Note that the perfect shell in the plot is the shell with uniform thickness of 166 μm and no mid-plane imperfection. The load-end shortening curve for the imperfect shell was computed based on the measured non-uniform thickness and mid-plane imperfection of wavy shell 3. The perfect shell buckles at 10.437 kN as the axial load drops to 10.290 kN

when it reaches the first limit load. However, the non-linearity due to imperfections leads to a smooth load-end shortening curve and prevents the decrease in axial load at around 10.437 kN, resulting in a higher buckling load than the perfect wavy shell.

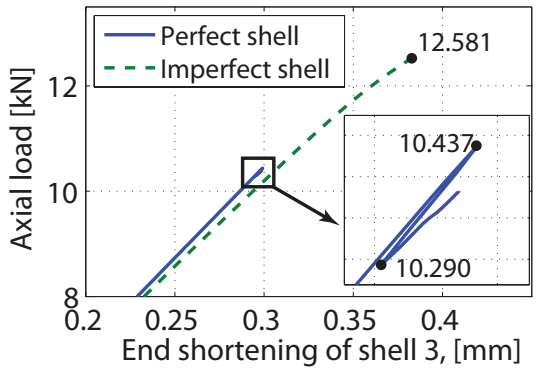

Figure 4.16: Load versus end shortening curves for perfect shell and imperfect wavy shell 3.

4.3.5 Estimation of Material Strength and Structural Failure Analysis

4.3.5.1 Material Strength

The composite material used in this study consists of 30 μm thick unidirectional laminae of T800 carbon fibers and ThinPreg 120EPHTg-401 epoxy with a fiber volume fraction of 50%. The laminate configuration is $[+60°, -60°, 0°]_s$, where 0° is the shell axial direction. Due to the material availability, the strength of the lamina was estimated based on the properties of the ThinPreg 120EPHTg-401 epoxy provided by the North Thin Ply Company and measured fiber misalignment. The interlaminar shear strength for ThinPreg 120EPHTg-401 reinforced by T700 with a volume fraction of 58% is 94.9 MPa (The North Thin Ply Company, 2013). Assuming the material is transversely isotropic, it is reasonable to use the interlaminar shear strength as the in-plane shear strength F_6. The in-plane shear strength of the unidirectional composite based on matrix shear failure can be predicted by (Daniel and Ishai, 2006):

$$F_6 = \frac{F_{ms}}{k_\tau} \tag{4.4}$$

where F_{ms} is the matrix shear strength and k_τ is the shear stress concentration factor. k_τ is given by (Daniel and Ishai, 2006):

$$k_\tau = \frac{1 - V_f(1 - G_m/G_{12})}{1 - (4V_f/\pi)^{1/2}(1 - G_m/G_{12})} \tag{4.5}$$

where V_f, G_m, and G_{12} are the fiber volume fraction, shear modulus of matrix and fiber, respectively. Assuming G_m is much smaller than G_{12}, Eq. 4.5 can be written as:

$$k_\tau = \frac{1 - V_f}{1 - (4V_f/\pi)^{1/2}} \tag{4.6}$$

k_τ for the unidirectional composite consisting of ThinPreg 120EPHTg-401 and T700 fibers with a volume fraction of 58% is calculated as 2.991 by Eq. 4.6.

The in-plane shear strength for the unidirectional composite consisting of ThinPreg 120EPHTg-401 and T800 fibers can be estimated by:

$$F_{6,T700}k_{\tau,T700} = F_{ms} = F_{6,T800}k_{\tau,T800} \tag{4.7}$$

The local fiber volume fraction of the composite can be modified by thickness through:

$$V_{f,T800} = \frac{V_{f,nom}}{\alpha}, \tag{4.8}$$

where α is the ratio between the measured local thickness and nominal thickness (180 μm). The in-plane shear strength can be calculated by Eqs. 4.7 and 4.8:

$$F_{6,T800} = \frac{1-(4V_{f,nom}/(\alpha\pi))^{1/2}}{1-(V_{f,nom}/\alpha)}F_{6,T700}k_{\tau,T700}, \tag{4.9}$$

where $V_{f,nom} = 0.5$, $F_{6,T700} = 94.9$ MPa, $k_{\tau,T700} = 2.991$.

The longitudinal compressive strength can be estimated by using the initial fiber misalignment (Daniel and Ishai, 2006):

$$F_{1c} = \frac{F_6}{\phi} \tag{4.10}$$

where ϕ is the initial fiber misalignment that was measured as 1.9° for the composite used in the present study. Therefore, the longitudinal compressive strength can be estimated by:

$$F_{1c,T800} = \frac{1-(4V_{f,nom}/(\alpha\pi))^{1/2}}{1-(V_{f,nom}/\alpha)}\frac{F_{6,T700}k_{\tau,T700}}{\phi} \tag{4.11}$$

The transverse compressive strength $F_{2c,T800}$ was not able to estimated. However, F_{2c} is usually about 200 to 228 MPa for carbon/epoxy unidirectional composite (Daniel and Ishai, 2006). Therefore, we assume $F_{2c,T800} = 200$ MPa.

4.3.5.2 Failure Analysis

We used the maximum stress theory to estimate the failure load of the wavy shells. The lamina principal stresses can be computed by (Daniel and Ishai, 2006):

$$[\sigma]^k_{1,2} = [T]^k([Q]^k_{x,y}[\varepsilon^o]_{x,y} + z[Q]^k_{x,y}[\kappa]_{x,y}) \tag{4.12}$$

where $[T]^k$ and $[Q]^k_{x,y}$ are the transformation matrix and transformed stiffness matrix of the k^{th} layer:

$$[T]^k = \begin{pmatrix} cos^2\theta_k & sin^2\theta_k & 2cos\theta_k sin\theta_k \\ sin^2\theta_k & cos^2\theta_k & -2cos\theta_k sin\theta_k \\ -cos\theta_k sin\theta_k & cos\theta_k sin\theta_k & cos^2\theta_k - sin^2\theta_k \end{pmatrix} \tag{4.13}$$

$$[Q]^k_{x,y} = [T^{-1}]^k \begin{pmatrix} \frac{E_1}{1-\nu_{12}\nu_{21}} & \frac{\nu_{12}E_1}{1-\nu_{12}\nu_{21}} & 0 \\ \frac{\nu_{12}E_1}{1-\nu_{12}\nu_{21}} & \frac{E_2}{1-\nu_{12}\nu_{21}} & 0 \\ 0 & 0 & G_{12} \end{pmatrix} [T]^k \tag{4.14}$$

θ_k denotes the fiber angle of the layer k. $[\varepsilon^o]_{x,y}$ and $[\kappa]_{x,y}$ are the transformed mid-plane strain and curvature. z is the distance between the mid-plane of the k^{th} layer and the laminate mid-plane.

The shell is subject to axial compression, and hence we assume that the critical region is at the element where the longitudinal compressive strain is maximum. The failure analyses were carried out only on the critical element in the FEA model, and the procedure is illustrated in Fig. 4.17. The strains and curvatures at the critical region at load P were obtained in the analyses in Section 4.3.4 based on the measured thickness and mid-plane imperfections. The principal stresses of each layer were calculated by Eq. 4.12 using the local $ABD(\alpha)$. Local F_{1c} and F_6 were also obtained by Eqs. 4.10 and 4.9, and F_{2c} was assumed to be 200 MPa. The principal stresses $|\sigma_1|$, $|\sigma_2|$, and $|\tau|$ at each layer were compared to F_{1c}, F_{2c}, and F_6. The analysis was repeated until any principal stress reached the corresponding strength.

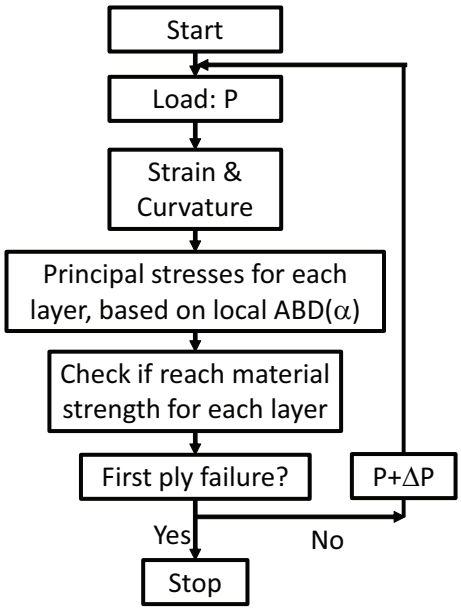

Figure 4.17: Flow chart of the failure analysis on the critical region.

The ratio between the principal stresses and strengths on the critical region of the wavy shell 1 are plotted in the Fig. 4.18. All laminae are subject to compression in both longitudinal and transverse direction.

Fig. 4.18 shows that layer 5 ($-60°$) failed first by shearing at about 11.9 kN.

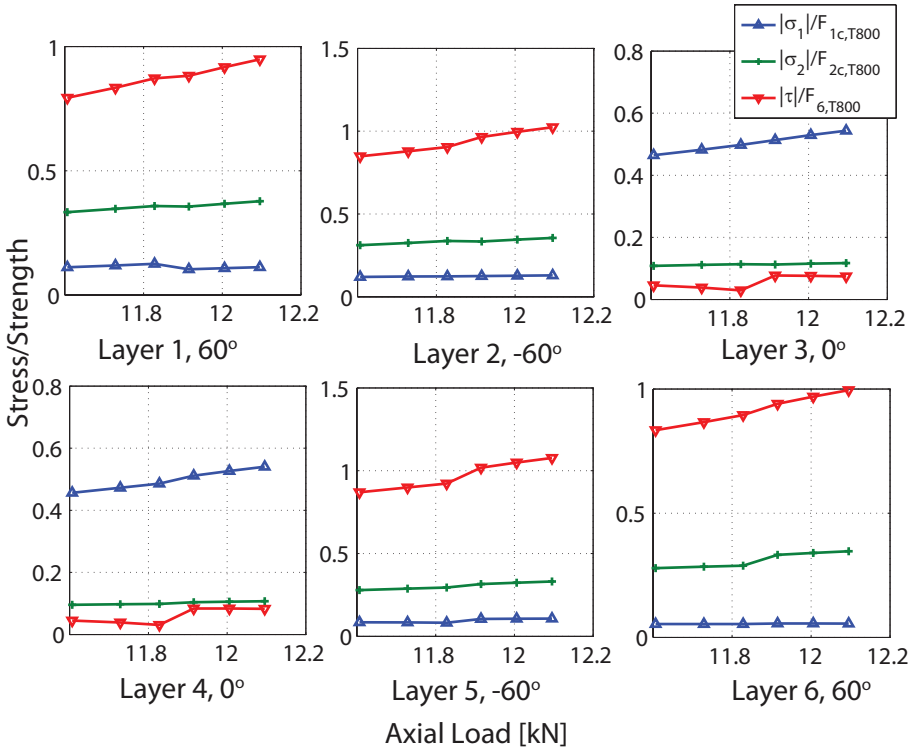

Figure 4.18: The ratio between the stress and the corresponding strength for each layer of laminate of wavy shell 1. Layer 1 is on the outer surface of the shell.

The stresses of wavy shells 2 and 3 were also computed. It was found that wavy shell 2 failed by shearing in layer 5 ($-60°$) at 11.65 kN and wavy shell 3 failed by shearing in layer 6 ($60°$) at 11.78 kN.

The difference between the buckling load and failure load of the wavy shell should be clarified. The material strength was not considered in all buckling analyses, i.e., in computing the load-displacement curves shown in Fig. 4.16. The buckling loads were chosen to be the first limit loads on the load-displacement curves. Due to the nearly stable post-buckling behavior of the perfect wavy shell, the imperfect wavy shells can carry higher loads than the buckling load of the perfect wavy shell. Therefore, the wavy shells are not sensitive to imperfections, i.e., imperfections cannot reduce the buckling loads.

Failure loads are the ones that correspond to the structural collapse due to material failure. The analyses described above show that the imperfect wavy shells collapse due to material failure, and the failure loads are approximately 10% lower than the buckling loads of the imperfect wavy shells. However, the failure loads of the imperfect wavy shells are approximately 10% higher than the buckling load of the perfect wavy shell (10.437 kN). Successful experimental validations should show that the measured compressive loads of the wavy shells can reach 100% of the buckling load of the perfect wavy shell (10.437 kN). Since the failure loads are higher than 10.437 kN, it is expected that material strength does not affect the feasibility of experimental validations.

4.4 Experiments

This section presents the test setup and experimental behavior of three wavy shells. Two circular shells were also tested and compared to the wavy shells.

4.4.1 Test Setup

Fig. 4.19 shows the setup for compression tests. The Instron 5500 Series materials testing machine with a 50 kN load cell was employed to conduct the compression tests. The displacement rate was 1mm per minute and the tests took about 30 seconds. A Vic3D digital image correlation (DIC) system was used to record shell deformations before structural collapse. A Phantom v310 high speed camera was used to capture the process of shell collapse. The high speed camera was pointed toward the critical region predicted in the analyses in Section 4.3. The film speed was 2000 to 3000 frames per second. The total recording time was about 10 seconds and the recording was manually triggered when the compressive loads reached 9.5 kN.

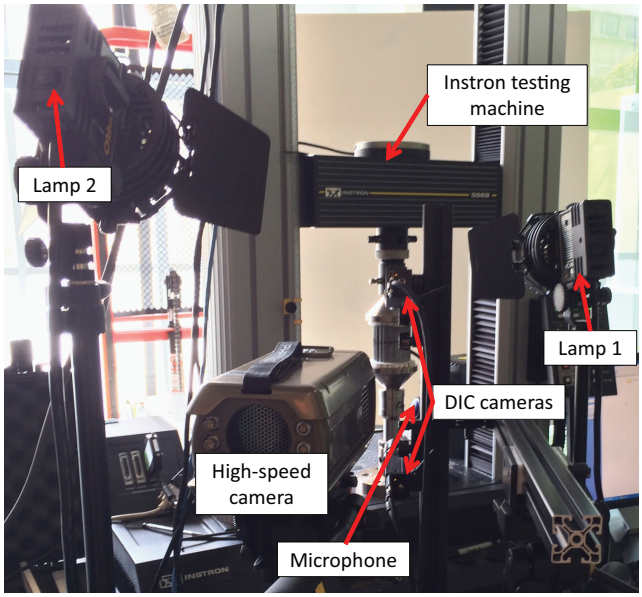

Figure 4.19: Experimental setup for compression tests.

4.4.2 Experimental Behavior of Wavy Shells

The buckling loads of the perfect wavy shell, predicted and measured failure loads, and knockdown factors of the wavy shells are summarized in Table 4.4. All wavy shells collapsed at loads higher than the buckling load of the perfect shell, indicating that our design was imperfection-insensitive. The measured failure loads were very close to the predicted loads. The failure loads were very consistent as the maximum load was only 3.4% higher than the minimum one.

The load-time curves of the three wavy shells are plotted in Fig. 4.20. The compressive loads of wavy shells

	Failure Load [KN]			Knockdown Factor
	Perfect	Prediction	Test	
Wavy Shell 1	10.437	11.90	11.475	1.099
Wavy Shell 2		11.65	11.680	1.114
Wavy Shell 3		11.78	11.302	1.083

Table 4.4: Predicted and measured failure loads and knockdown factors for wavy shells. The buckling load of the perfect wavy shell was computed based on the uniform thickness of 166 μm, which is the measured average thickness.

1 and 3 increased monotonically until they collapsed. The compressive load of wavy shell 2 monotonically increased to 11.58 kN, and the load dropped to 11.52 kN and then to 11.51 kN before ramping up to the the failure load,11.68 kN.

The acoustic emissions of the three wavy shells during loading were recorded and plotted in Fig. 4.21. The acoustic emission technique is very convenient to study damage initiation and progression (Agarwal et al., 2006). There is only one high-amplitude event in the acoustic emission of wavy shells 1 and 3, respectively, and the event corresponds to the structural collapse. The acoustic emission of wavy shell 2 shows three high-amplitude events. The third event was due to the structural collapse. The first and second events correspond to the two decreases in load in the load-time curve of wavy shell 2 shown in Fig. 4.20. It is generally accepted that the fracture of fibers could result in high-amplitude events (Agarwal et al., 2006). Therefore, there may be two local fiber-failure events before the final structural collapse for wavy shell 2. These two local failures did not propagate immediately, and the shell was able to carry higher compressive load until the structural collapse. For wavy shell 2, the load corresponding to the third high-amplitude event (structural collapse) was chosen to be the failure load.

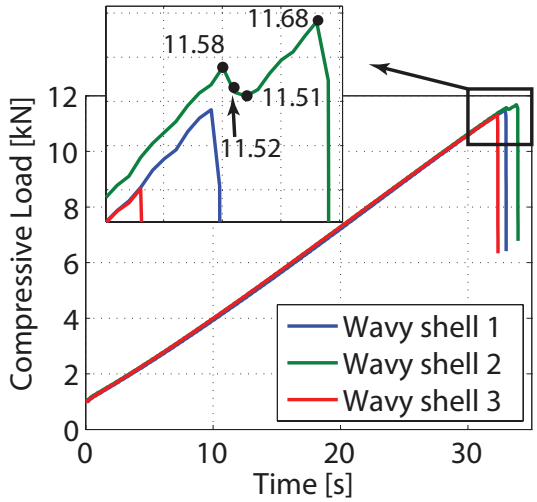

Figure 4.20: Load-time curve for wavy shells.

Shell deformations were recorded by the 3D DIC system and a typical out-plane deformation field is plotted in Fig. 4.22. The shell expanded outward when the axial load was small (around 4 kN); however,

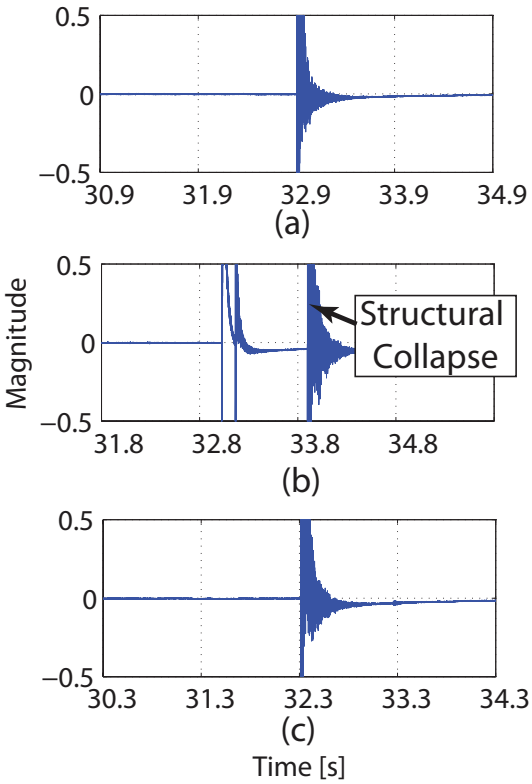

Figure 4.21: Acoustic emissions of wavy shells 1, 2, 3 are plotted in (a), (b), and (c), respectively.

waves along the axial direction appeared as the load increased. Fig. 4.22 (b) shows that there were wavy deformations even when the axial loads were smaller than the buckling loads of perfect shell, and the waves remained when the loads ramped beyond the perfect buckling load (Fig. 4.22 (c)) until the shells failed. These phenomena suggest that for our imperfection-insensitive wavy shells imperfections lead to a stable post-buckling behavior, conforming with the observed failure loads shown in the Tab. 4.4.

The typical failure process recorded by the high-speed camera was plotted in Fig. 4.23. Fig. 4.23 (b) shows that the shell failed at a local region, which led to the collapse of the whole structures (Fig. 4.23 (c)). Significant delamination was observed when the shell was unloaded. These observations conform with the failure predictions in Section 4.3.

The predicted critical regions where the axial compressive strains are maximum, along with the observed kind band, are shown in the circles in Fig. 4.24. The initial failure region of wavy shell 1 was not captured by the high-speed camera, but its kink band went through the critical regions predicted from simulations. The initial failure region of wavy shell 2 was on the same corrugation and at about the same height as the predicted critical region. Three initial failure regions of wavy shell 3 were observed, and two regions were on the same corrugation as the predicted critical region. The predicted critical region is about 1 cm higher than the observed initial failure regions.

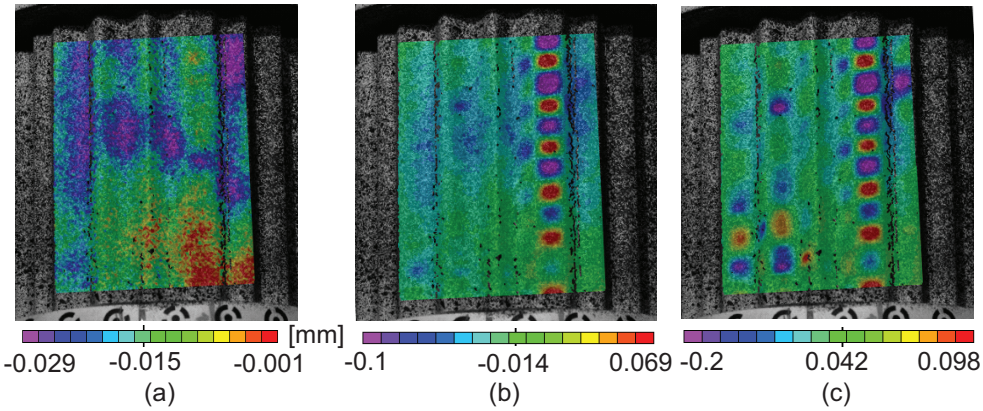

Figure 4.22: Out-plane deformations of wavy shell 2 when the axial load was (a) 3.985 kN, (b) 9.536 kN, and (c) 11.626 kN

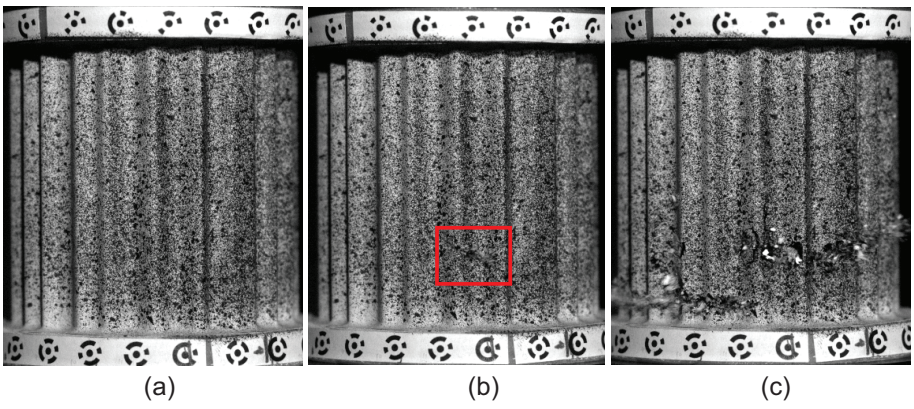

Figure 4.23: Three consecutive images recorded by the high speed camera when the shell was (a) before collapse, (b) during collapse, and (c) after collapse. The initial failure region is in the rectangle in (b).

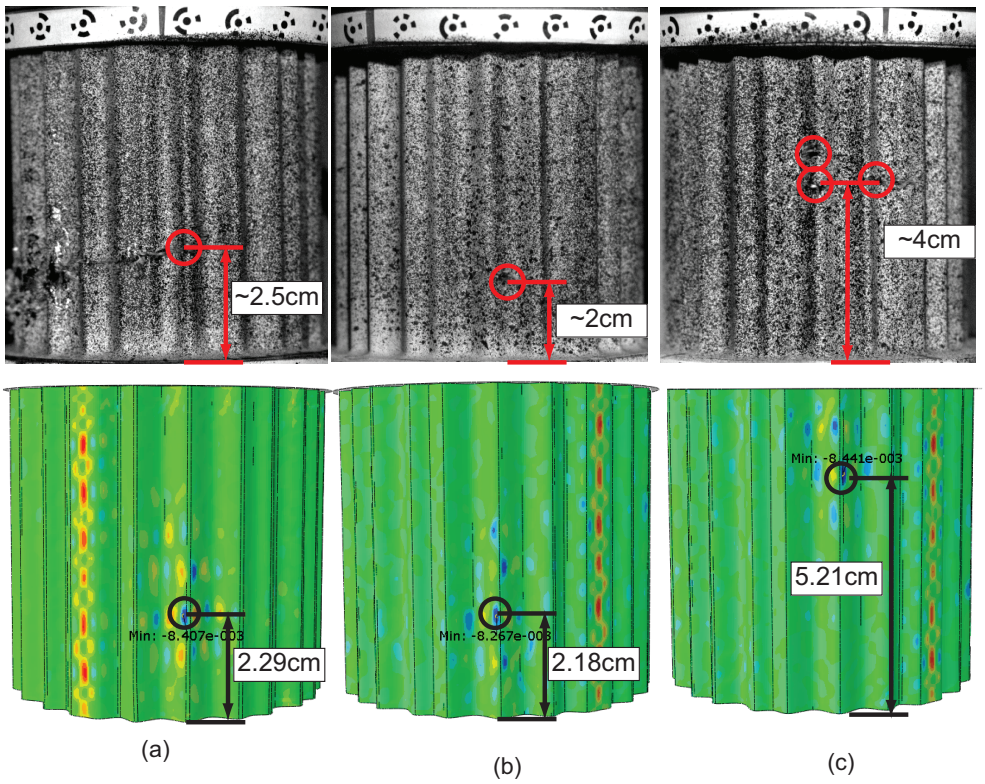

Figure 4.24: Comparison of the critical regions between experiments (top) and simulations (bottom) for wavy (a) shell 1, (b) shell 2, and (c) shell 3. The simulations show the axial compressive strain fields.

4.4.3 Experimental Behavior of Circular Cylindrical Shells

Two composite circular cylindrical shells of the same radius and length as the wavy shells were made and tested. The thickness and imperfection distributions were measured before the compression tests. The results are summarized in Tabs. 4.5 and 4.6. Although the thicknesses of circular shells are more uniform and the imperfection amplitudes are smaller than the wavy shells, the measured buckling loads were much lower than the buckling load of the perfect circular cylindrical shell. The average buckling load is 2.209 kN, only 19.3% of the average failure load of the wavy shells. The highest knockdown factor is only 0.589, indicating a large imperfection-sensitivity.

Shells	Thickness [μm]	Imperfection Amplitude [μm]	μ
Circular shell 1	176±9	257	1.43
Circular shell 2	176±13	394	2.19

Table 4.5: Measured thickness and imperfections of circular shells.

Shells	Buckling Load (perfect) [kN]	Measured Buckling Load [kN]	Knockdown factor
Circular shell 1	4.058	2.392	0.589
Circular shell 2		2.025	0.499

Table 4.6: Measured buckling loads and knockdown factors of circular shells..

Fig. 4.25 shows the typical buckling shape of the circular shells. It can be seen that the circular shells buckled into the classical diamond shape. No material failure was observed after unloading, indicating that the circular shells cannot fully utilize the capacity of the composite materials.

Figure 4.25: Typical buckling shape for circular shells.

4.5 Summary

We have developed a fabrication technique which was able to make cylindrical shells with intricate wavy cross-sections. We have also developed a potting technique which can obtain clamped boundary conditions without introducing large imperfections. Instead of using traditional three-dimensional survey systems, we developed a photogrammetry technique to measure the geometric imperfections of our shells. Three wavy cylindrical shells and two circular cylindrical shells were fabricated and tested in this study.

We predicted the behavior of the wavy shells under axial compression based on the measured thickness and mid-plane imperfection distributions. The buckling load of the perfect wavy shell, i.e., a wavy shell with uniform thickness of 166 μm and without mid-plane imperfections, was calculated as 10.473 kN. The mid-plane imperfections and non-uniformity of thickness were then incorporated in the finite element models to compute the buckling loads of imperfect wavy shells. The predicted buckling loads of the three imperfect shells with measured imperfections were between 12.581 and 13.125 kN, larger than the buckling load of the perfect wavy shell. This confirmed that the wavy shells were not sensitive to imperfections. The material strength was estimated and we conducted failure analyses based on the maximum stress theory. It was predicted that the three wavy shells can reach the material strength and collapse at 11.90, 11.65, and 10.78 kN, respectively, due to the shearing in the $\pm 60^o$ layers. The initial failure regions were also predicted.

We carried out compression tests on three wavy shells and two circular cylindrical shells. A DIC system, high-speed camera, and microphone were employed to record the shell responses during the tests. The three wavy shells collapsed at compressive loads of 11.302 kN, 11.475 kN, and 11.680 kN, respectively. The difference among the three failure loads was only 3.4%, and discrepancy between the measured and predicted failure loads was less than 4.1%. The shell deformations obtained by the DIC system showed that axial waves appeared at a low load and remained until the shells collapsed. The high-speed camera was able to capture the initial failure regions of wavy shells 2 and 3. The kink band of wavy shell 1 went through the predicted critical region; the positions of the initial failure regions matched well with the predicted critical regions. Significant delamination was observed after unloading for all the wavy shells. The measured average buckling load of the circular cylindrical shells was only 19.3% of the average failure load of the wavy shells. The highest knockdown factor of the circular shells was only 0.589. Comparisons between the wavy shells and circular shells showed that introducing optimal symmetry-breaking wavy cross-section can significantly reduce imperfection-sensitivity and improve the load-bearing capability of cylindrical shells.

Chapter 5

Buckling Analysis of Corrugated/Stiffened Shells Using Modified Bloch Wave Method

This chapter presents a fast computational method for the buckling analysis of corrugated and stiffened cylindrical shells under axial compression. The method is first described and several computational examples are then presented to validate the method.

5.1 Methodology

A modification of the Bloch wave method that exploits the stiffness matrix method for rotationally periodic structures has been developed. We present the modified Bloch wave method in this section by using an example of corrugated cylindrical shell. It should be noted that our method is also applicable to the buckling analysis of stiffened cylindrical shell under axial compression.

5.1.1 Bloch Wave Method for Rotationally Periodic Structures under Axial Compression

Consider, for definiteness, a corrugated cylindrical shell under axial compression. It is periodic only in the circumferential direction and is compressed by the application of a uniform end-shortening on one of its ends, as shown in in Figs. 2.9 (b) and 5.1 (a).

The Bloch wave method for 2-dimensional infinite periodic structure cannot be directly used for the buckling analysis of axially loaded rotationally periodic structures due to the following issues. First, the shell is not infinitely long in the longitudinal direction. Second, the Bloch wave method for 2-dimensional infinite periodic structures cannot capture the effects of clamped boundary conditions on edges A and B in Fig. 2.9 (b). Third, corrugated or stiffened shells have finite number of corrugations or stiffeners in the circumferential direction, leading to finite values of wave numbers in the circumferential direction, as

discussed in Section 2.1.3.2.

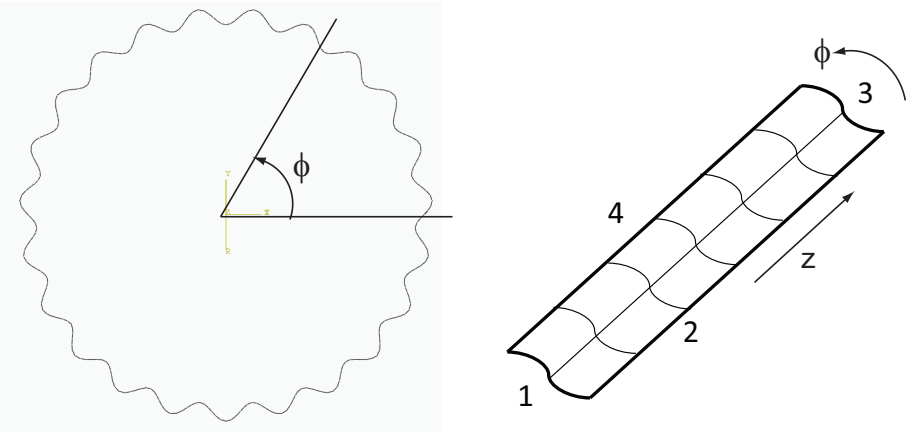

Figure 5.1: (a) Cross-section of corrugated cylindrical shell. (b) Schematic of a complete corrugation. ϕ and z are the circumferential and axial directions, respectively. The four edges of the corrugation are denoted as edges 1 to 4.

In order to consider the finite length of the shell and the boundary conditions, a complete corrugation, as shown in Fig. 5.1 (b), is considered. Edge 1 is fully clamped and edge 3 is clamped to a rigid plate and subject to uniform end-shortening. Due to the rotationally periodicity, the following Bloch wave propagation functions are used:

$$\begin{aligned} \tilde{U}(z,\phi) &= P_u(z,\phi)\exp(in\phi) \\ \tilde{F}(z,\phi) &= P_f(z,\phi)\exp(in\phi) \end{aligned} \tag{5.1}$$

z and ϕ denote the shell axial coordinate and angular position in the circumferential direction; n is the wave number. P_u and P_f are rotationally periodic functions with periodicity of one unit cell (one corrugation). Note that there is only one wave number n corresponding to the wave propagation in circumferential direction in the exponential terms. According to Eq. 5.1, edges 2 and 4 are coupled by the following displacement and force Bloch relations:

$$\begin{aligned} \tilde{U}_4 &= \tilde{U}_2 \ \exp(i\frac{2\pi}{N}n) \\ \tilde{F}_4 &= -\tilde{F}_2 \ \exp(i\frac{2\pi}{N}n) \end{aligned} \tag{5.2}$$

where N is the total number of unit cells, i.e., corrugations or longitudinal stiffeners, along the circumferential direction. We define a coupling matrix $Q(n)$ to eliminate the dependent displacements:

$$\tilde{U} = Q\ U_{ind} \tag{5.3}$$

where U_{ind} is the independent displacements and $\tilde{U}_{ind} = [\tilde{U}_i, \tilde{U}_1, \tilde{U}_2, \tilde{U}_3]^T$. Q involves the exponential terms in Eq. 5.2 and is a function of wave number n. Similar to the discussion in Section 2.1.3.3, the buckling conditions of a single unit cell can be transformed into the following eigenvalue problem by using the coupling matrix Q:

$$Q^T K(\lambda_c) Q U_{ind} = \hat{K}(n, \lambda_c) U_{ind} = Q^T \tilde{F} = 0 \tag{5.4}$$

where λ_c is the buckling load corresponding to a wave number n. More details are presented in Appendix A.

Two features of the stiffness matrix method can be incorporated into the modified Bloch wave method. First, the feasible values of wave number n are the same as those in the stiffness matrix method:

$$n = 0, 1, 2, ..., \{N/2\} \tag{5.5}$$

where $\{N/2\}$ is $N/2$ for even N and $(N-1)/2$ for odd N. The displacement relation in Eq. 5.2 has the same form as Eq. 2.18. Therefore, n and $N-n$ are the same mode propagating in opposite directions and only one of them is necessary in the analysis. The critical buckling load is the lowest among the buckling loads for all values of n:

$$\lambda_{crit} = \min_{n=0,1,2,...,\{N/2\}} (\lambda_c(n)) \tag{5.6}$$

Second, as discussed in Section 2.1.3.2, the eigenmode has zero displacement on the edge 3 in Fig. 5.1 for $n > 0$. Edge 3 is clamped to a rigid plate and subject to uniform end-shortening. Therefore, all nodes on edge 3 have the same displacements. The only condition that satisfies the displacement relation in Eq. 5.2 for $n > 0$ is $U_3 = 0$. Edge 1 is always fully clamped and U_1 is zero in all analyses.

5.1.2 Buckling and Natural Frequency Analysis

Operationally, the eigenvalue analysis of the buckling problem in Eq. 5.4 is solved by analyzing the corresponding natural frequency problem. This is based on the fact that buckling happens when the lowest natural frequency decreases to zero as the load magnitude is increased (Virgin, 2007).

The equation of motion for a single corrugation is

$$M\ddot{\tilde{u}} + K\tilde{u} = \tilde{F} \tag{5.7}$$

where M and K are mass and stiffness matrices, respectively. $\tilde{u}$ is the complex-valued displacement field and $\ddot{\tilde{u}}$ denotes its second derivative with respect to time t. The displacement can be written as

$$\tilde{u} = \tilde{U} e^{i\omega t} \tag{5.8}$$

where ω is the angular frequency. Substitute Eq. 5.8 into 5.7, multiply it by Q^T, use the relation in Eq. 5.3,

and eliminate the exponential term to obtain the relation:

$$Q^T(K - \omega^2 M)Q\tilde{U}_a = 0 \tag{5.9}$$

Equation 5.9 is an eigenvalue problem, and the eigenvalue ω^2 and eigenvector $\tilde{U}$ are respectively the square of the natural frequency and the corresponding vibration mode.

If the lowest natural frequency is zero, i.e. $\omega^2 = 0$, Eq. 5.9 degenerates into the eigenproblem in Eq. 5.4. Therefore, the buckling problem can be solved through the natural frequency problem by finding the load at which the lowest natural frequency is zero. The vibration mode of the frequency problem in this case is also the buckling mode.

When the eigenvalue ω^2 is positive, the angular frequency ω is a real value. Then, $\tilde{u}$ can be written as

$$\tilde{u} = \tilde{U}e^{i\omega t} = \tilde{U}(\cos(\omega t) + i\sin(\omega t)) \tag{5.10}$$

However, when $\omega^2 < 0$, ω is a complex value and $e^{i\omega t}$ exponentially grows with time, leading to an unstable structure. Therefore, $\omega^2 = 0$ corresponds to the onset of buckling and this relation is exploited to facilitate the implementation of the Bloch wave method in Abaqus.

5.2 Numerical Implementation

Most of the current commercial finite element packages, including Abaqus, cannot deal with complex-valued fields. We modified the technique developed by Aberg and Gudmundson (1997), Bertoldi et al. (2008); Shim et al. (2013), and Shim et al. (2013) to apply our modified Bloch wave method in Abaqus. Our technique is first presented in this section, followed by an efficient algorithm of finding the critical buckling loads and modes.

5.2.1 Finite Element Implementation

The complex-valued fields can be separated into real and imaginary parts, and the equation of motion of a corrugation (Eq. 5.7) can be written as

$$\left(\begin{bmatrix} K & \mathbf{0} \\ \mathbf{0} & K \end{bmatrix} - \omega^2 \begin{bmatrix} M & \mathbf{0} \\ \mathbf{0} & M \end{bmatrix} \right) \begin{bmatrix} \tilde{U}^{Re} \\ \tilde{U}^{Im} \end{bmatrix} = \begin{bmatrix} \tilde{F}^{Re} \\ \tilde{F}^{Im} \end{bmatrix} \tag{5.11}$$

where $\tilde{U}^{Re}$, $\tilde{U}^{Im}$, $\tilde{F}^{Re}$, and $\tilde{F}^{Im}$ are the real and imaginary parts of the displacement and force fields of a unit cell. The complex Bloch relation of displacements in Eq. 5.2 can be separated into two equations, each

of which represents the real or imaginary relation:

$$\begin{aligned}\tilde{U}_4^{Re} &= \tilde{U}_2^{Re}\cos(\frac{2\pi}{N}n) - \tilde{U}_2^{Im}\sin(\frac{2\pi}{N}n)\\ \tilde{U}_4^{Im} &= \tilde{U}_2^{Re}\sin(\frac{2\pi}{N}n) + \tilde{U}_2^{Im}\cos(\frac{2\pi}{N}n)\end{aligned} \tag{5.12}$$

Eq. 5.12 can be represented by two identical meshes in a single analysis in Abaqus whose boundaries are coupled by the *MPC (Multi-Point Constraint) function in Abaqus, as shown in Fig. 5.2. Nodes A and B have the same axial and circumferential coordinates. Their displacements are input into Eq. 5.12 to calculate $\tilde{U}_4^{Re}$. The displacements of node C are enforced to be $\tilde{U}_4^{Re}$ by the *MPC. The imaginary part of the Bloch relations can also be realized in the same way.

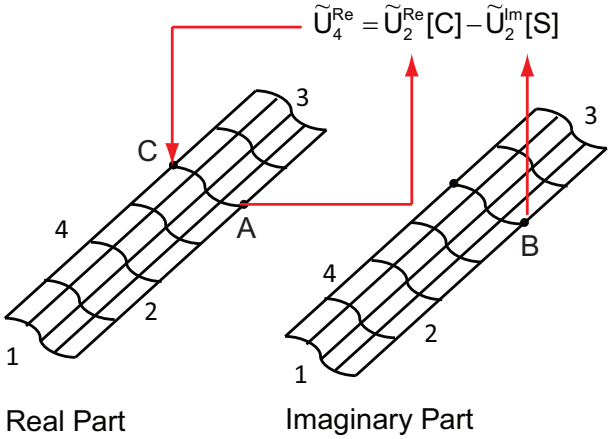

Figure 5.2: Schematic of two identical meshes coupled by the *MPC function in Abaqus. $[S]$ and $[C]$ are the sine and cosine terms in Eq. 5.12, respectively. Only the real part of the Bloch relation is shown in this figure.

Similar to previous discussions, the coupling relations give the following eigenvalue problem:

$$Q^T\left(\begin{bmatrix} K & \mathbf{0} \\ \mathbf{0} & K \end{bmatrix} - \omega^2 \begin{bmatrix} M & \mathbf{0} \\ \mathbf{0} & M \end{bmatrix}\right) Q\ \tilde{U}_{ind} = 0 \tag{5.13}$$

where $\tilde{U}_{ind}$ is independent displacements and Q is the coupling matrix. More details can be found in Appendix A.

The calculation of ω^2 consists of two steps: a nonlinear static analysis (pre-buckling analysis) and a frequency analysis (eigenvalue analysis). In the static analysis the pre-buckling deformation of cylindrical shell has a periodicity of one unit cell, i.e., $\tilde{U}_2^{Re} = \tilde{U}_4^{Re}$ and $\tilde{U}_2^{Im} = \tilde{U}_4^{Im}$. Edge 1 is fully clamped and the shell is compressed by applying a uniform axial end-shortening on edge 3, i.e., $\tilde{U}_1^{Re} = \tilde{U}_1^{Im} = 0$ and $\tilde{U}_{z,3}^{Re} = \tilde{U}_{z,3}^{Im} = Uz$. Therefore, the load parameter λ in the previous discussion is $\lambda = |Uz|$.

In the frequency analysis edges 2 and 4 are coupled by the Bloch relations Eq. 5.12. Edge 1 is fully clamped. As discussed in the previous section, $\tilde{U}_3^{Re}$ and $\tilde{U}_3^{Im}$ are zero when $n > 0$ in order to satisfy the

Bloch relations. For the case $n = 0$, the real and imaginary parts are not coupled and the only free degree of freedom of edge 3 is the uniform translational displacement in the z (axial) direction. $|Uz|$ corresponding to zero ω^2 is the buckling load λ_c for the wave number n.

5.2.2 Algorithm for Finding Critical Buckling Load

In principle, we need to run $\{N/2\} + 1$ simulations in order to find the lowest buckling load according to Eq. 5.6:

$$\lambda_{crit} = \min_{n=0,1,2,\ldots,\{N/2\}} (\lambda_c(n))$$

This process could be computationally expensive. We developed an algorithm to reduce the number of simulations required to find the lowest buckling load. Our algorithm consists of four steps which are shown in Fig. 5.3.

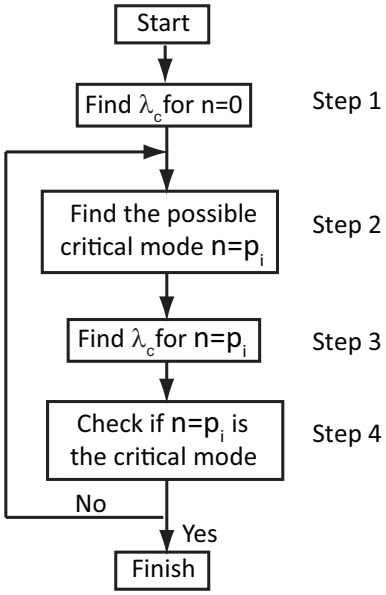

Figure 5.3: Flow chart of the algorithm of finding the critical buckling mode and load.

5.2.2.1 Step 1: Find the Buckling Load for $n = 0$ mode

In the nonlinear static step, the shell is compressed by applying incremental uniform end-shortening. The bifurcation point B_0 of mode $n = 0$, as shown in the schematic Fig. 5.4, is found when the eigenvalue ω^2 obtained from the frequency analysis are zero. Operationally, coarse increments are first used and the increment containing the bifurcation point is further refined until the required accuracy is achieved.

Both the pre-buckling deformation and buckling mode for $n = 0$ have the periodicity of one unit cell, i.e., $\tilde{U}_2^{Re} = \tilde{U}_4^{Re}$ and $\tilde{U}_2^{Im} = \tilde{U}_4^{Im}$. Therefore, the structure can be loaded into the postbuckling state in the nonlinear static step. Four possible situations could happen if the compressive load is larger than the

buckling load $\lambda_c(n=0)$, and the methods of finding $\lambda_c(n=0)$ for these cases are discussed as follows.

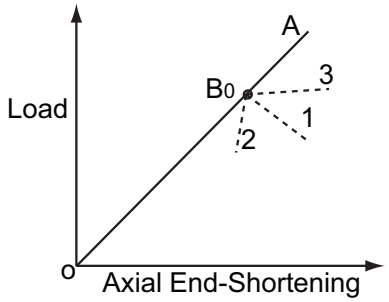

Figure 5.4: Schematic of possible post-buckling branches. B_0 is the bifurcation point corresponding to the branch of $n=0$.

Even though the nonlinear analysis is used for the static step, it is still possible that the shell stays on the primary branch $B_0 - A$ when the load exceeds the bifurcation point. The shell is in an unstable state in this case. The shell is also not stable if it is loaded into the branch $B_0 - 1$. Therefore, the eigenvalue ω^2 of the loading state on branches $B_0 - A$ and $B_0 - 1$ are negative, whereas ω^2 is positive before buckling. For these two cases, B_0 can be accurately found by checking the change of sign of ω^2.

The branch $B_0 - 2$ is also unstable. The shell is subject to displacement-control loading ($\lambda = |Uz|$) in the static step and the compressive end-shortening incrementally increases. Hence, the shell can never reach the branch $B_0 - 2$. The increments of the nonlinear static analysis are set to automatically decrease in order to find the equilibrium state. Therefore, the shell can reach a loading state that is very close to B_0. The last point on the primary branch is used as the bifurcation point in this case.

B_0 is relatively difficult to find for the case of stable post-buckling branch $B_0 - 3$ because its eigenvalues are still positive and B_0 cannot be found by checking the change of signs of eigenvalues. Two signatures are used to determine if the shell is in the stable post-buckling state. First, the eigenvalue decreases dramatically when the load is close to the bifurcation point and it increases from zero when the load exceeds B_0 and goes onto branch $B_0 - 3$. Second, the slope of the load-displacement curve is different for the primary and secondary branches. We use the point with largest slope change, i.e. largest curvature, on the load-displacement curve $O - B_0 - 3$ as the bifurcation point, instead of finding the point with zero eigenvalue which is operationally very difficult for this case.

5.2.2.2 Step 2: Find the Possible Critical Mode p_i

Instead of sequentially computing the buckling loads for $n = 1, 2, ..., \{N/2\}$, we always find the possible critical mode $n = p_i$ and calculate the corresponding buckling load $\lambda_c(p_i)$ in each iteration, where i denotes the i^{th} iteration. The structure loaded at $\lambda_c(p_{i-1})$ is used to find p_i. $\lambda_c(n=0)$ is used in the first iteration $i = 1$. The procedure is described as follows.

First, frequency analyses corresponding to the modes in the search domain were performed on the structure loaded at $\lambda_c(p_{i-1})$. The search domain is the set of buckling modes which contains the critical one, and

it is $n = 1, 2, ..., \{N/2\}$ for the first iteration $i = 1$. The search domain is updated in Step 4 for iterations $i > 1$.

If the eigenvalue ω^2 is positive for a certain mode $n = n_+$, then the buckling load corresponding to $n = n_+$ is larger than $\lambda_c(p_{i-1})$. The reason is that the structure needs to be compressed more in order to reduce ω^2 to zero. Although the buckling load of mode $n = n_+$ is unknown, it is sure that $n = n_+$ is not a critical mode. Therefore, all modes with positive ω^2 at the stress state of $\lambda_c(p_{i-1})$ are discarded in future analyses.

Second, only the modes with negative eigenvalues are defined as search domain for future analyses. The mode with lowest negative value is likely to be the critical one and it is chosen to be the possible critical mode p_i.

5.2.2.3 Step 3: Find the Buckling Load for p_i

The structure is compressed incrementally in a nonlinear static step, and a frequency analysis step is then used to find the load at which ω^2 is zero. In the nonlinear static step, the deformation of the shell is enforced to have the periodicity of one unit cell, i.e. $\tilde{U}_2^{Re} = \tilde{U}_4^{Re}$ and $\tilde{U}_2^{Im} = \tilde{U}_4^{Im}$; however, the buckling mode of $n = p_i$ has different periodicity according to the Bloch relations (Eq. 5.12). Therefore, the structure stays on the primary path of mode $n = p_i$ during the loading in the static step. As a result, the eigenvalue ω^2 is negative when the load exceeds the bifurcation point of $n = p_i$, and the buckling load $\lambda_c(p_i)$ can be found by checking the change of sign of ω^2. Operationally, coarse increments are first used and the increment containing the bifurcation point is further refined until the required accuracy is achieved.

5.2.2.4 Step 4: Check if p_i is the Critical Mode

If $n = p_i$ is the critical mode, then the eigenvalues corresponding to the stress state at $\lambda_c(p_i)$ for the other modes are all positive. Therefore, the search domain is empty for the next iteration and the program is stopped in this case. If there exist some modes with negative eigenvalues at the stress state at $\lambda_c(p_i)$, then $n = p_i$ is not the critical mode. The updated search domain consists of these modes with negative eigenvalues and the program goes back to Step 2 for the next iteration.

This algorithm can reduce computational effort due to three reasons. First, it always finds the buckling load of the possible critical mode rather than sequentially searches $n = 0, 1, 2, ..., \{N/2\}$. Hence, it can find the critical mode as soon as possible. Second, coarse increments are first used and the increment containing the bifurcation point is then refined in the static analysis. This can reduce the number of nonlinear analyses which are time-consuming. Third, most of the frequency analyses are are independent with each other and they are parallel carried out, further reducing the computational time.

5.3 Numerical Examples

We applied our analysis method to several corrugated cylindrical shells and a stiffened cylindrical shell in order to validate both the method formulation and the implementation techniques. For each problem, two additional solutions were obtained by carrying out both linear and nonlinear buckling analyses using full finite element models. Note that a linear buckling analysis is an eigenvalue analysis of an unloaded structure, and a nonlinear buckling analysis is an eigenvalue analysis of a loaded structure whose stress state is obtained by a nonlinear static analysis. The results and computational time required for these two full solutions are compared to the modified Bloch wave method.

5.3.1 Corrugated Composite Cylindrical Shells

5.3.1.1 Shell Geometry and Material

The corrugations are sinusoidal and the cross-sections were obtained by superposing a sinusoidal wave on a reference circle:

$$r(\phi) = R + \Delta r \sin(N\phi), \tag{5.14}$$

where N is the total number of corrugations and Δr their amplitude. In this thesis, the number of corrugations N is chosen to be $N = 12, 13, 16, 17, 19, 22, 23, 34, 25, 26, 29, 30, 31, 37, 40$

The shells were chosen to have a square aspect ratio. The dimensions presented in Table 5.1 were chosen.

Table 5.1: Dimensions of wavy shell designs

Thickness, t	180 μm
Radius, R	35 mm
Length L	70 mm
Maximum deviation from circle, Δr	1.5 mm

A symmetric six-ply laminate, $[+60°, -60°, 0°]_s$ was adopted, and 0° direction is shell axial direction. It consisted of 30 μm thick unidirectional laminae of T800 carbon fibers and ThinPreg 120EPHTg-402 epoxy, with a fiber volume fraction of approximately 50%. The following lamina properties were measured: $E_1 = 127.9$ GPa, $E_2 = 6.49$ GPa, $G_{12} = 7.62$ GPa, and $\nu_{12} = 0.354$, where E_1 is the modulus along the fiber direction. The ABD matrix of the laminate was calculated from these properties, using classical lamination

theory:

$$ABD = \begin{pmatrix} 9.919 \times 10^6 & 2.670 \times 10^6 & 0 & 0 & 0 & 0 \\ 2.670 \times 10^6 & 9.919 \times 10^6 & 0 & 0 & 0 & 0 \\ 0 & 0 & 3.625 \times 10^6 & 0 & 0 & 0 \\ 0 & 0 & 0 & 0.0108 & 0.0099 & 0.0034 \\ 0 & 0 & 0 & 0.0099 & 0.0373 & 0.0081 \\ 0 & 0 & 0 & 0.0034 & 0.0081 & 0.0125 \end{pmatrix} \tag{5.15}$$

where the units of the A and D matrices are N/m and Nm, respectively.

5.3.1.2 Buckling Loads and Modes

Around 1,500 S4 fully integrated shell elements were used for a corrugation in the Bloch wave method. Both linear and nonlinear analyses of detailed full finite element models were carried out. The full finite element models have the same element size as the models in the Bloch wave method. All simulations of these examples were run on a Xeon X5680 server with 12 CPUs on a single motherboard.

The linear eigenvalue analysis *Buckle function of Abaqus was used for linear buckling analysis. Abaqus offers the Lanczos and the subspace iteration eigenvalue extraction methods. It was found that the Lanczos method was much slower than the subspace method and it failed to solve the eigenvalue problem for the shells with more than 23 corrugations. Therefore, the subspace method was used for the linear buckling analysis. As discussed in the previous sections, there are two coincident buckling modes for the cases $n > 0$. It was found that the subspace method could provide an inaccurate second buckling mode if the number of extracted eigenvalues is too small. Therefore, we extracted the first 10 eigenmodes although we are only interested in the first two buckling modes. We found that this setup was able to provide accurate second buckling modes.

The nonlinear analyses of full detailed finite element models consisted of two steps, similar to the Bloch wave method, that are a nonlinear static analysis and a frequency analysis. The shells were first compressed by applying a uniform end-shortening at one end, and then a frequency step was carried out to find the eigenvalue ω^2 corresponding to this stress state. The critical buckling load was found when the eigenvalue ω^2 decreased to zero. Coarse increments in the nonlinear static step were first used and the increment containing the bifurcation point was then refined. The frequency analyses are independent of each other so they were performed in a parallel way.

The critical axial end-shortening obtained from the modified Bloch wave method, nonlinear, and linear full finite element analyses are plotted in Fig. 5.5. The buckling loads are plotted in Fig. 5.6. In the linear eigenvalue analysis only one parameter can be used in extracting the eigenvalue, i.e., the critical end-shortening and critical buckling load cannot be obtained by the eigenvalue analysis at the same time. In the present study, the end-shortening was extracted as the eigenvalue. Therefore, the critical loads were

not obtained for linear eigenvalue analysis. One could use load as the parameter for the linear eigenvalue analysis if it is of interest; however, the critical end-shortening cannot be obtained in this case.

The results obtained from the Bloch wave method and the linear full finite element analyses are compared to the ones obtained from the nonlinear full finite element analyses. Figs. 5.5 and 5.6 show that the results obtained from the three methods are very close to each other. It was found that the differences were less than 0.5% for all the corrugated shells studied in this thesis.

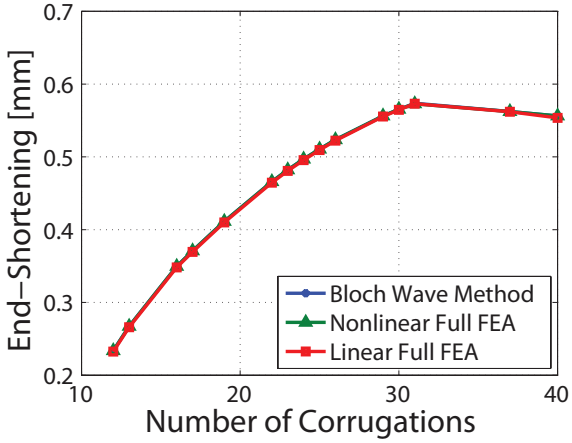

Figure 5.5: Critical end-shortening obtained from the modified Bloch wave method, nonlinear, and linear full FEA models.

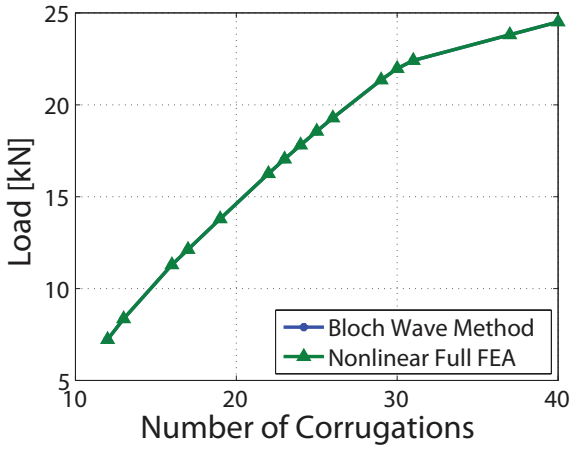

Figure 5.6: Critical buckling loads obtained from the modified Bloch wave method, nonlinear, and linear full FEA models.

The buckling modes obtained from the modified Bloch wave method, linear, and nonlinear full model analysis for $N = 13, 31, 40$ are plotted in Figs. 5.7, 5.8, and 5.9. The buckling modes in Fig. 5.7 are typical for shells with $N <= 30$ corrugations. Each corrugation has several half waves in the axial direction and two half waves in the circumferential direction. Compared to the size of a unit cell (a corrugation in this case), the wavelength in both axial and circumferential directions is small. Therefore, the buckling modes

are local for $N <= 30$. Fig. 5.7 shows that both the modified Bloch wave method and linear full FEA model can accurately capture the local buckling mode.

Figs. 5.8 (a) and (b) are typical buckling modes for shells with $N >= 31$ corrugations. There is only one half wave in the axial direction. The most significant component of the buckling mode is a uniform expansion in the radial direction. Therefore, the buckling modes for $N >= 31$ are global. Fig. 5.8 shows that, compared to the nonlinear full FEA model, the modified Bloch wave method can obtain accurate buckling modes. However, the linear FEA model produced a local mode for $N >= 31$. Fig. 5.9 shows the global buckling modes for the shell with $N = 40$ corrugations. Both the modified Bloch wave method and linear full FEA model were able to give accurate buckling modes.

Figs. 5.7, 5.8, and 5.9 show that the modified Bloch wave method can capture both local (short wavelength) and global (long wavelength) buckling and the buckling modes match the results obtained from the nonlinear full model analyses. However, although the linear full FEA models can provide accurate buckling loads, they could find inaccurate buckling modes in some cases, as seen in Fig. 5.8 (c).

5.3.1.3 Computational Time

The computational time for the three sets of simulations is plotted in Fig. 5.10. It can be seen that the computational time of the nonlinear full FEA models increased linearly with respect to the number of corrugations. For linear full FEA analysis, the computational time increased faster for larger number of corrugations and it was slightly faster than the nonlinear analysis for $N = 40$. However, the computational time of the Bloch wave method did not scale up as the number of corrugations increased.

5.3.2 Large-Scale Orthogonally Stiffened Aluminum Cylindrical Shell

5.3.2.1 Shell Geometry and Material

We applied the modified Bloch wave method to compute the buckling load and mode for a large-scale orthogonally stiffened aluminum cylindrical which was recently constructed by NASA Langley for the Shell Buckling Knockdown Factor project (Hilburger et al., 2012b). The stiffeners are on the internal side of the shell and consist of longitudinal stringers and circumferential rings. The geometry of stiffeners is presented in Fig. 5.11. The dimensions are listed in Tab. 5.2. The shell has 75 longitudinal stringers and 18 circumferential rings. The material is aluminum, and the modulus and Poisson's ratio used in this study are 68.9 GPa and 0.3, respectively.

5.3.2.2 Buckling Loads, Modes, and Computational Time

A unit cell shown in Fig. 5.12 was used in the modified Bloch wave method. Edge 1 was full clamped; edge 3 was clamped to a rigid plate and subject to uniform end-shortening. Edges 2 and 4 had the same displacement in the nonlinear static analysis step and were coupled by the Bloch relations Eq. 5.12 in the

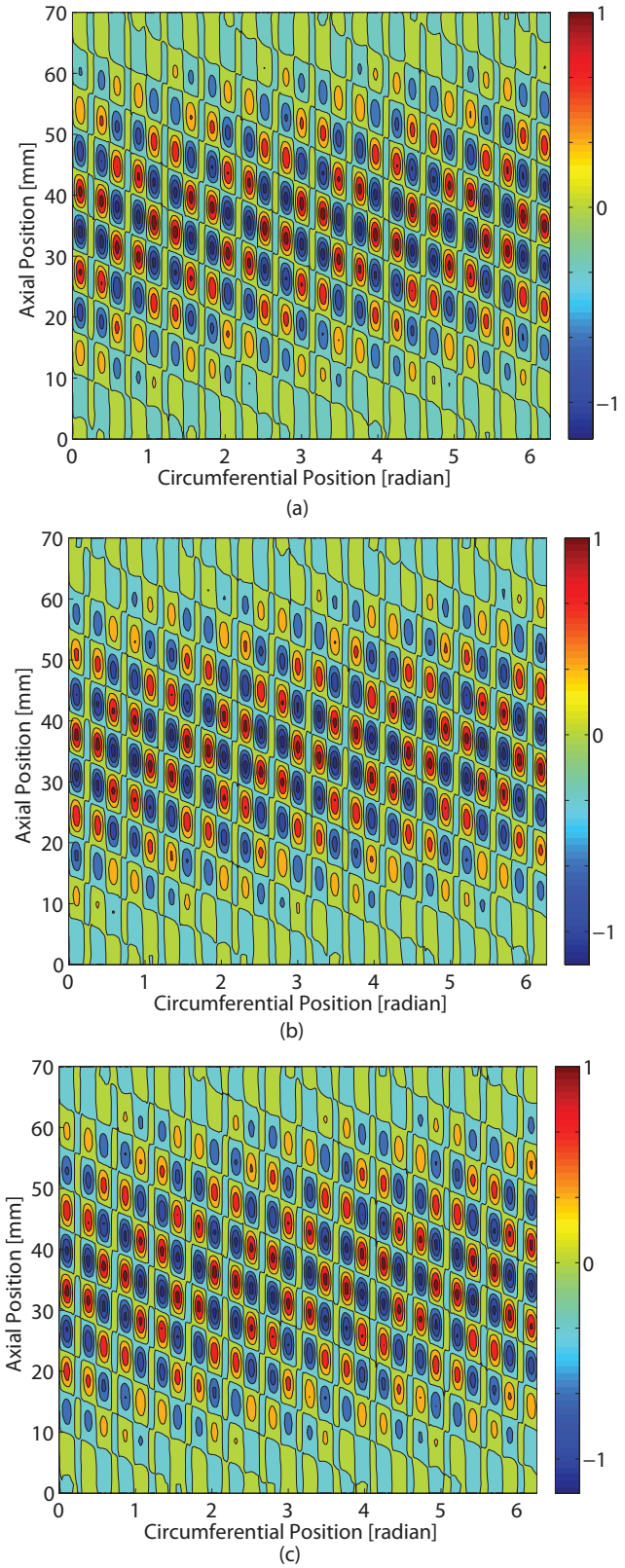

Figure 5.7: Buckling modes of the shell with $N = 13$ corrugations obtained from (a) modified Bloch wave method, (b) nonlinear full FEA model, and (c) linear full FEA model.

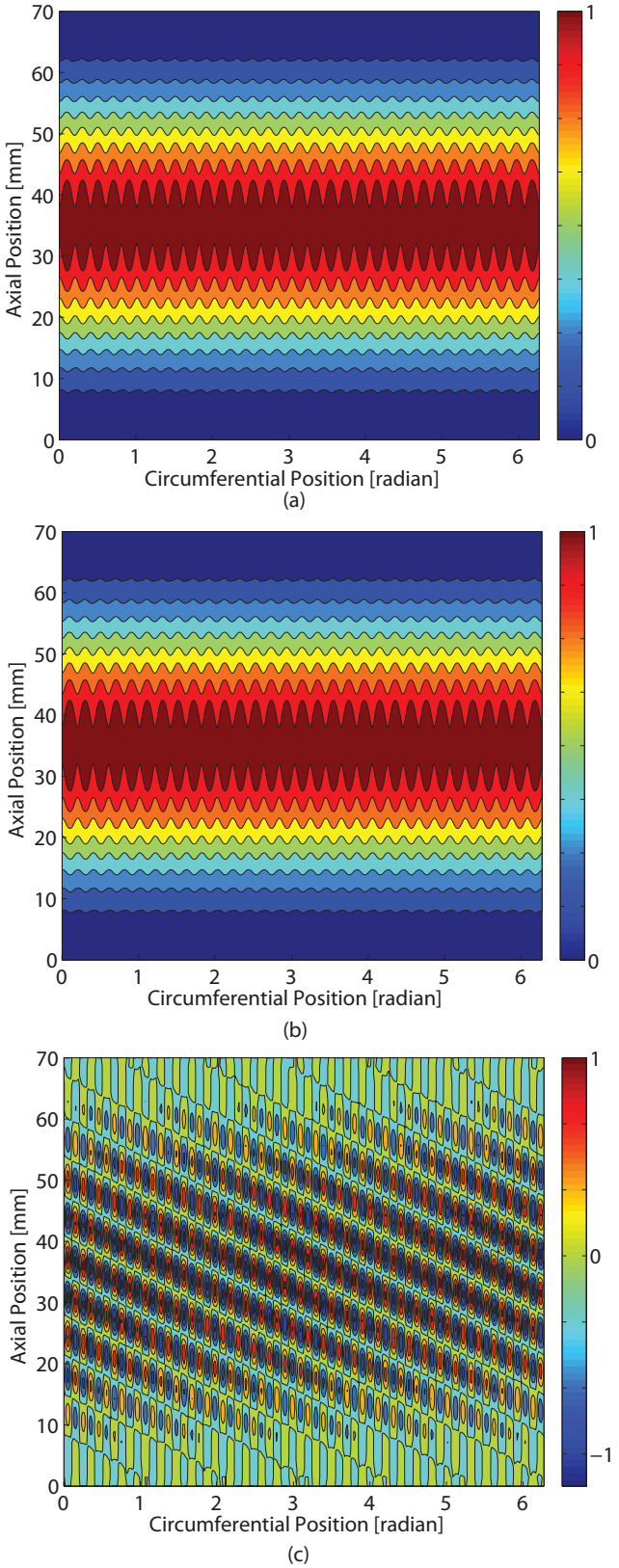

Figure 5.8: Buckling modes of the shell with $N = 31$ corrugations obtained from (a) modified Bloch wave method, (b) nonlinear full FEA model, and (c) linear full FEA model.

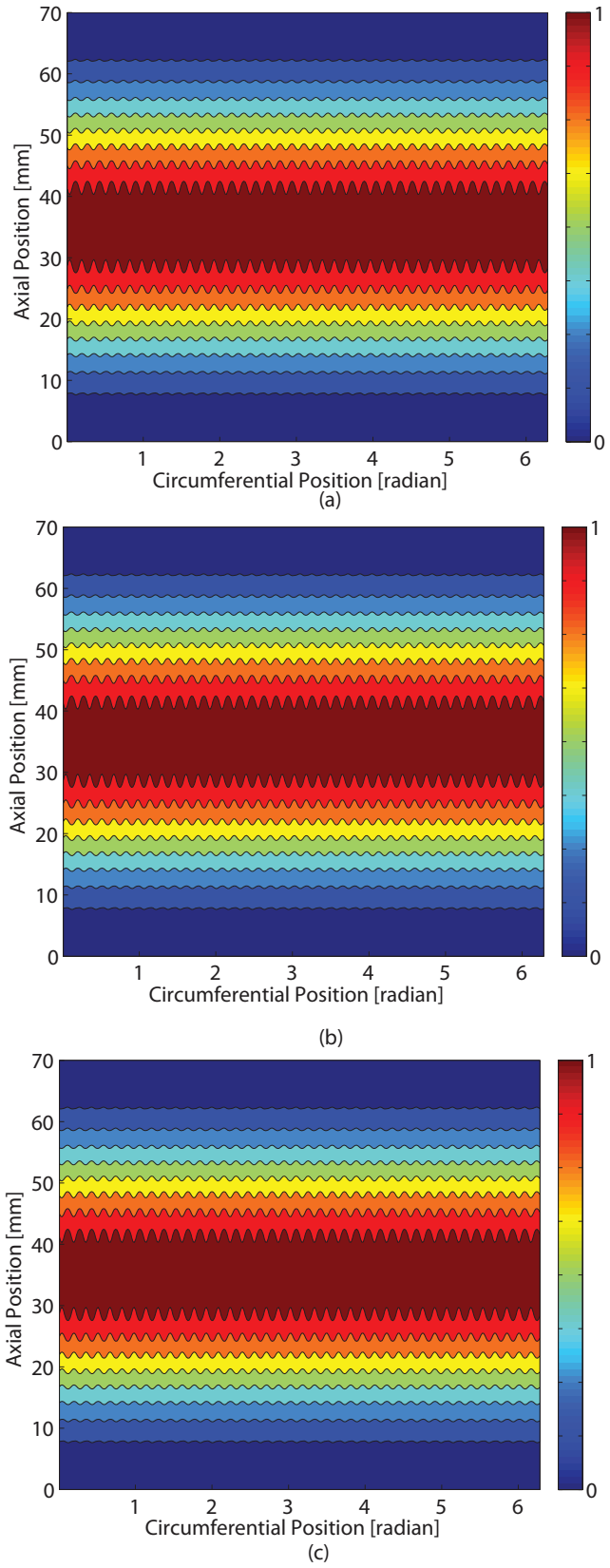

Figure 5.9: Buckling modes of the shell with $N = 40$ corrugations obtained from (a) modified Bloch wave method, (b) nonlinear full FEA model, and (c) linear full FEA model.

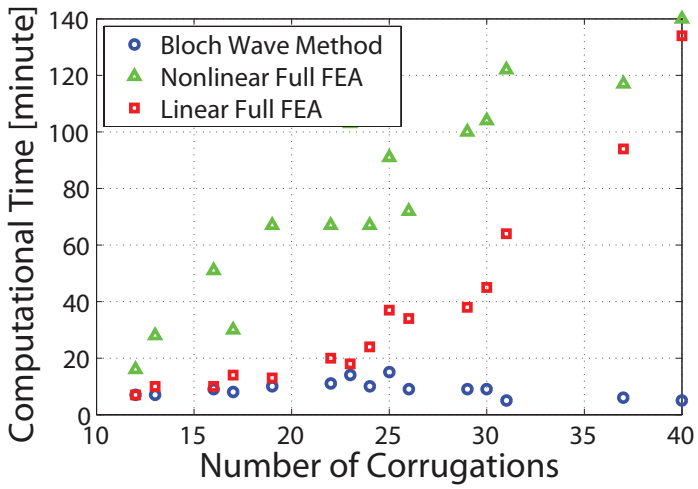

Figure 5.10: Computation time for the modified Bloch wave method, linear, and nonlinear full FEA models.

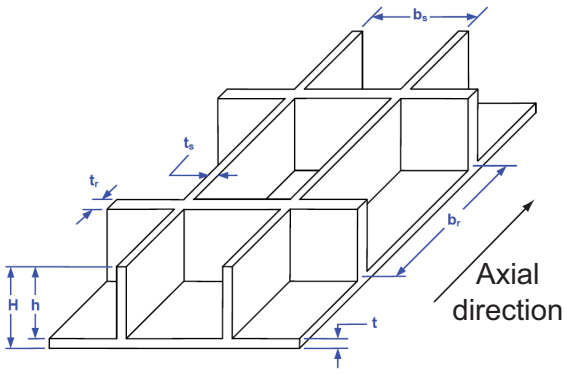

Figure 5.11: Schematic of stiffeners (from Hilburger et al. (2012b)).

Skin thickness, t	0.100
Stiffener height, H	0.400
Stiffener height, h	0.300
Space between stringers, b_s	4.00
Stringer thickness, t_s	0.100
Space between rings, b_r	4.00
Ring thickness, t_r	0.100
Shell radius, R	48.0
Shell length, L	72.0

Table 5.2: Dimensions of stiffeners. The unit is in inches.

frequency analysis step. Around 1,100 S4 fully integrated shell elements were used for a unit cell in the modified Bloch wave method.

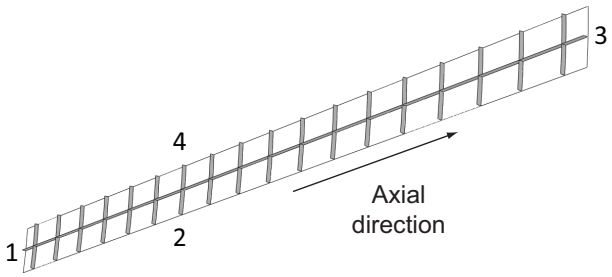

Figure 5.12: Schematic of a unit cell used in the modified Bloch wave method.

The computational setup for the linear and nonlinear full FEA models was the same as that of the corrugated cylindrical shells in Section 5.3.1. The full FEA models had the same element type and size as the modified Bloch wave method. All simulations of these examples were run on a Xeon E5410 desktop with 8 CPUs.

The buckling loads obtained from the three simulations and their computational time are presented in Tab. 5.3.2.2. Compared to the full nonlinear FEA model, the errors in the critical end-shortening obtained from the modified Bloch wave method and linear full FEA model are within 0.3%. The difference between the buckling loads of the full nonlinear FEA model and the modified Bloch wave method is within 0.6%. Although the full nonlinear FEA model was most accurate, it required significant computational effort and the simulation took 16 hours to finish. However, the modified Bloch wave method and full linear FEA model were much more efficient and the computational time was 0.5 and 1 hour, respectively.

	Critical End-Shortening [mm]	Critical Axial Load [kN]	Computational Time [hour]
Modified Bloch wave method	3.3546	2719	0.5
Full nonlinear FEA	3.3554	2702	16
Full linear FEA	3.3458	N/A	1

Table 5.3: Buckling loads and computational time of stiffened shell.

The buckling modes obtained from the modified Bloch wave method and nonlinear full model analysis for the stiffened shell are plotted in Figs. 5.13 (a) and (b). It can be seen that the modified Bloch wave method can produce accurate buckling mode. The buckling mode has 5 half waves in the axial direction. There are 15 waves in the circumferential direction and each circumferential full wave spans over 5 stringers. Compared to the size of a grid in Fig. 5.11, the wavelength in both axial and circumferential directions is large. The full linear FEA model also produced a mode with 15 full waves in the circumferential direction; however, the mode has 7 half waves in the axial direction. Therefore, although the linear full FEA model can obtain accurate buckling load with high computational efficiency, it cannot produce accurate buckling

mode.

5.4 Summary

We have developed an efficient computational method for the buckling analysis of corrugated and stiffened cylindrical shells which builds on the Bloch wave method and the stiffness matrix method of rotationally periodic structures. The traditional Bloch wave method is applicable for the buckling analysis of infinitely 2- or 3-dimensional periodic structures. We modified the Bloch wave method in order to analyze the buckling of rotationally periodic shell structures subject to axial compression. Following the work by Aberg and Gudmundson (1997) and Bertoldi et al. (2008); Shim et al. (2013), we implemented our modified Bloch wave method in the commercial finite element code Abaqus. We also developed a highly efficient algorithm of performing the modified Bloch wave method.

We used our modified Bloch wave method to analyze the onset of buckling for several small corrugated composite cylindrical shells and a large-scale orthogonally stiffened aluminum cylindrical shell. Both linear and nonlinear analyses based on detailed full finite element models were also performed in order to validate our method. It was shown that our modified Bloch wave method can obtain highly accurate buckling loads. Compared to the nonlinear full FEA models, the errors of the buckling loads obtained by the modified Bloch wave method are smaller than 0.6% for all the shells studied in this thesis.

Numerical examples also showed that the modified Bloch wave method can produce the same buckling modes as those obtained from the nonlinear full FEA models and that it can accurately capture local (short wavelength) and global (long wavelength) buckling modes. Comparisons between the buckling modes of linear and nonlinear full FEA models showed that, although the linear full FEA model can produce accurate bucking loads, the buckling modes obtained from the linear FEA model could be inaccurate.

In the examples of corrugated cylindrical shells, the computational time required by the modified Bloch wave method did not scale up as the number of corrugations increased. However, both linear and nonlinear full FEA models required much higher computational time than the Bloch wave method for heavily corrugated shells. For a shell with 40 corrugations, the computational time of the modified Bloch wave method is only 7% of the computational time of the linear and nonlinear full FEA models. For the stiffened cylindrical shell, the computational time of the modified Bloch wave method is respectively 50% and 3% of the computational time of the linear and nonlinear full FEA models.

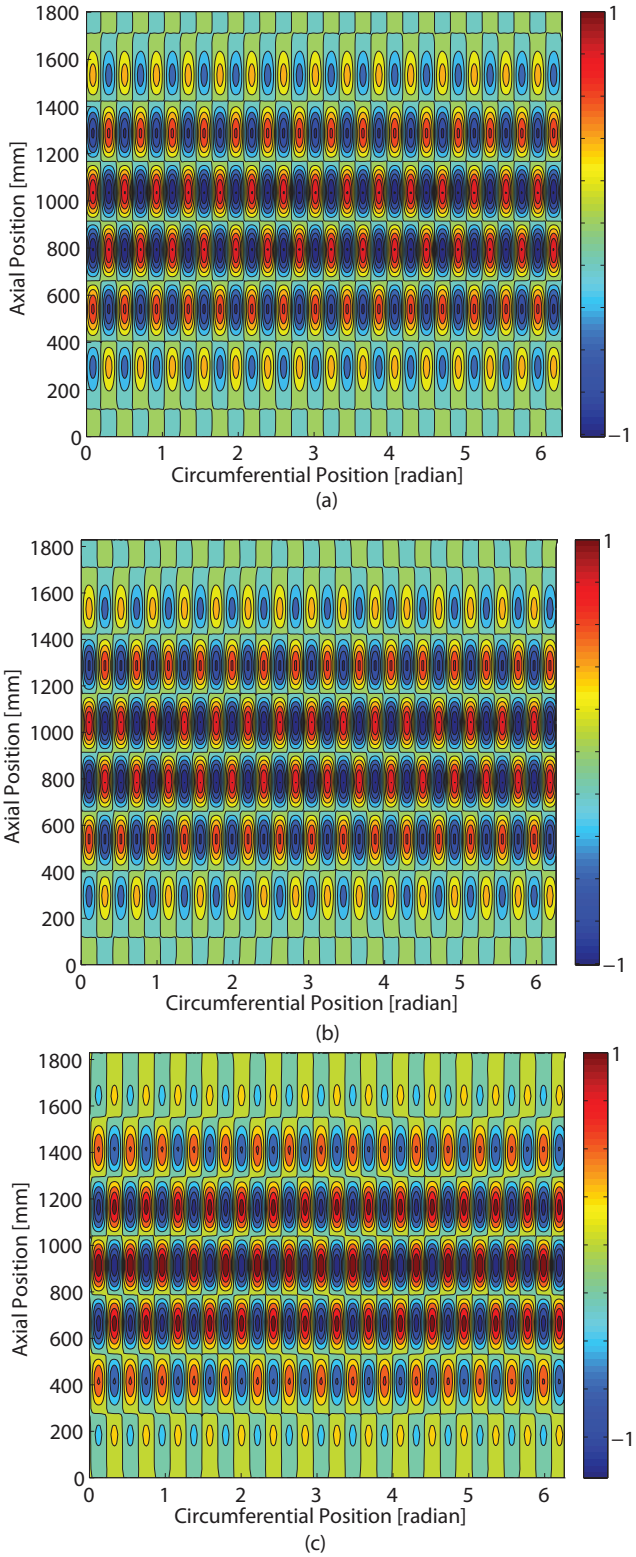

Figure 5.13: Buckling modes of the stiffened shell obtained from (a) modified Bloch wave method, (b) nonlinear full FEA model, and (c) linear full FEA model.

Chapter 6

Imperfection-Insensitive Pseudo-Spherical Shells

This chapter describes the studies of imperfection-insensitive pseudo-spherical shells under external pressure. It has been shown in the previous sections that breaking the rotational symmetry of axially compressed cylindrical shells can improve buckling loads and make the shells insensitive to imperfections. This idea of breaking symmetry is used to design imperfection-insensitive shells under external pressure. Specifically, the exact spherical symmetry is abandoned and polyhedra are used instead.

This chapter starts with the buckling analyses of several commonly seen designs, including an icosahedron and two geodesic shells. Then each face of an icosahedron was replaced by a pyramid, creating triambic icosahedra (Wenninger, 1974). Parametric studies were performed to investigate the effects of the heights of the pyramids. The best triambic icosahedron was then chosen as the initial design for further optimizations.

6.1 Icosahedron and Geodesic Shells

An icosahedron was chosen as the starting design of this study for two reasons. First, regular polyhedra have simple geometry and the icosahedron has larger volume than the other regular polyhedra with the same radius of a circumscribed sphere. Second, the faces of an icosahedron can be subdivided to create geodesic shells, which approach to a sphere as the order of subdivision increases. Assuming the radius of the circumscribed sphere is constant, the only parameter required to define a geodesic shell is the order of subdivision. Therefore, it is easy to parameterize the geometry of a geodesic shell.

6.1.1 Geometry and Material

An icosahedron has 20 equilateral triangular faces, 30 edges, and 12 vertices, and it has 5 equilateral triangular faces at each vertex. Fig. 6.1 shows a model of icosahedron and its 2D folding pattern.

A geodesic sphere is obtained by subdividing the faces of an icosahedron and then projecting the intermediate vertices onto the circumscribed sphere. Fig. 6.2 shows half of a geodesic shell. The blue lines in

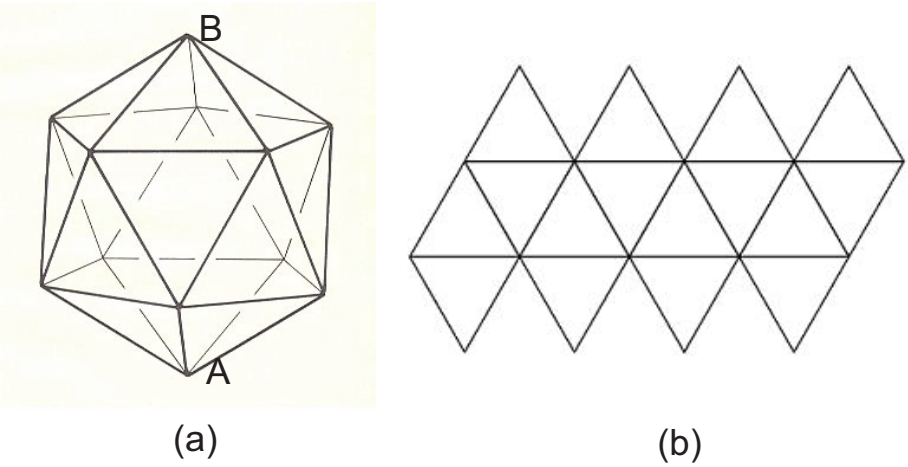

Figure 6.1: (a) Icosahedron. (b) The 2D folding pattern of an icosahedron.

Fig. 6.2 represent the original topology of an icosahedron, and the red lines are new edges created through the subdivision. The solid dots are the original vertices of the icosahedron, and the empty dots are the intermediate vertices obtained by subdividing the faces of the icosahedron.

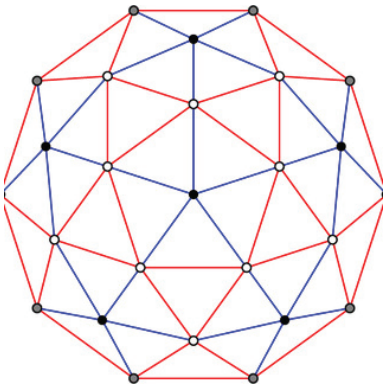

Figure 6.2: A second order geodesic sphere. Note that only half of the shell is shown in the figure for clarity. (Image from www.instructables.com)

Fig. 6.3 explains the method of creating a geodesic shell. The triangle in Fig. 6.3 (a) corresponds to a face of an icosahedron. The second order subdivision splits each edge into two equal segments and creates four equilateral triangles (Fig. 6.3 (b)) . Similarly, the n^{th} order subdivision divides each edge of a face of an icosahedron into n equal segments and creates n^2 equilateral triangles. The intermediate vertices (empty dots in Fig. 6.3 (b) and (c)) are then projected on the circumscribed sphere along the radial direction, while keeping them connected by straight lines. The new triangles are the faces of geodesic shells.

In the present study, the radius of the circumscribed sphere of the icosahedron was chosen to be 0.5 m, and the shell thickness was 0.5 mm. Aluminum was used as the material, and it was assumed to be linear-elastic. The Young's modulus and Poisson's ratio were 68.9 GPa and 0.3, respectively.

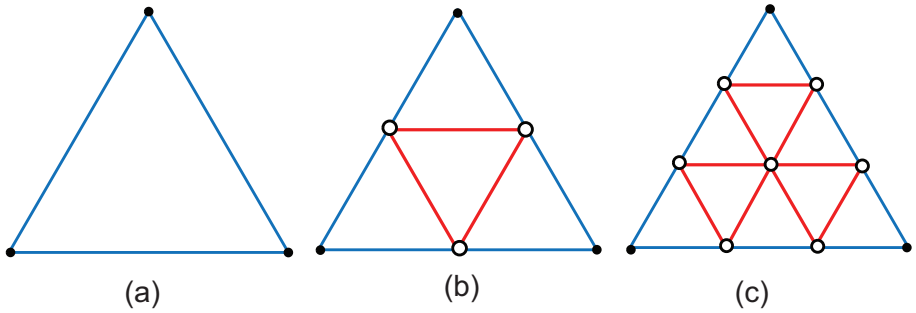

Figure 6.3: Schematic of subdividing a face of icosahedron into faces of a geodesic sphere. (a) A face of icosahedron. (b) Second order subdivision. (c) Third order subdivision.

6.1.2 Simulation

The simulation method used in this section is the same as that of the cylindrical shells under axial compression in Section 3.1.3 except the type of shell elements, the boundary and loading conditions, and the solver for calculating buckling pressures. The general purpose finite element package Abaqus 6.11 was used to calculate the buckling pressure. Fully-integrated triangular thin shell elements (element S3) were used for the Abaqus models. The size of each element was chosen as 0.02 m, and there were around 20,000 elements in the model. All the six degrees of freedom of the lowest vertex A, as shown in Fig. 6.1, were fixed in the simulation. The highest vertex B can only move downward and its other degrees of freedom were fixed. The shell was subject to uniform external pressure.

The nonlinear static analysis solver of Abaqus/Standard was used to calculate pressure-displacement curves. It was found that the Riks solver of Abaqus/Standard often crashed before the structure actually buckled. Therefore, the Riks solver was not used in all simulations of shells under external pressure. The external pressure was incrementally increased until it reached the first maximum value. Therefore, the simulation was load-controlled. Since the pressure always increased, the simulation was stopped at the first limit point of the external pressure and it was chosen to be the buckling pressure. The postbucklng behavior was not able to be found due to the nature of this nonlinear static solver. The increments of external pressure were automatically determined by the solver. The maximum and minimum increments allowed were 4 kPa and 0.4 Pa, respectively.

Similar to Section 3.1.3, both perfect and imperfect models were used in the simulations. The shape of the imperfections was the first buckling mode obtained by a linear eigenvalue solver. The amplitudes of the imperfections were chosen to be $\pm t$, where t is the shell thickness, 0.5 mm.

6.1.3 Results

The simulation method in 6.1.2 was use to analyze an icosahedron, a second order geodesic shell, and a third order geodesic shell. A complete spherical shell with the same radius (0.5 m), thickness (0.5 mm), and material (aluminum) as icosahedron was also analyzed. The results are summarized in Tab. 6.1. P_0, P_+, and

P_- are the buckling pressures of the perfect shell and imperfect shells with positive and negative amplitudes of imperfections, respectively. γ is the knockdown factor defined in Eq. 3.10.

Table 6.1: Buckling pressure of icosahedron shell and geodesic shells.

Shell	P_0 [kPa]	$\min(P_+ , P_-)$ [kPa]	γ
Icosahedron	44.280	44.726	1.010
2^{nd} order geodesic	30.296	30.779	1.016
3^{rd} order geodesic	24.810	24.819	1.000
Sphere	83.641	25.304	0.303

The perfect spherical shell has the highest bucking pressure among the above shells. The buckling pressure of the perfect spherical shell obtained from the simulation is only 0.3% higher than the theoretical value, 83.4 kPa, which was calculated by Eq. 2.36. However, its knockdown factor is only 0.303, indicating an extreme imperfection-sensitivity. The buckling pressures of all the three perfect polyhedron shells are smaller than that of the spherical shell. The knockdown factors of the polyhedron shells are close to one, i.e., they are not sensitive to imperfections. The buckling pressure of the imperfect icosahedron is higher than the imperfect geodesic shells and the spherical shell. Note that the buckling pressures decrease as the order of subdivision increases. The results show that the icosahedron has better performance than the geodesic shells and spherical shell. Therefore, the icosahedron was chosen to be the initial design for further parametric studies.

6.2 Triambic Icosahedron

A triambic icosahedron is obtained by replacing each triangular face of a regular icosahedron with a pyramid. Fig. 6.4 (a) shows a model of triambic icosahedron. A trambic icosahedron has 60 identical triangular faces. The height of pyramid, i.e., the distance between the pyramid apex and the base face, was changed in the present parametric studies.

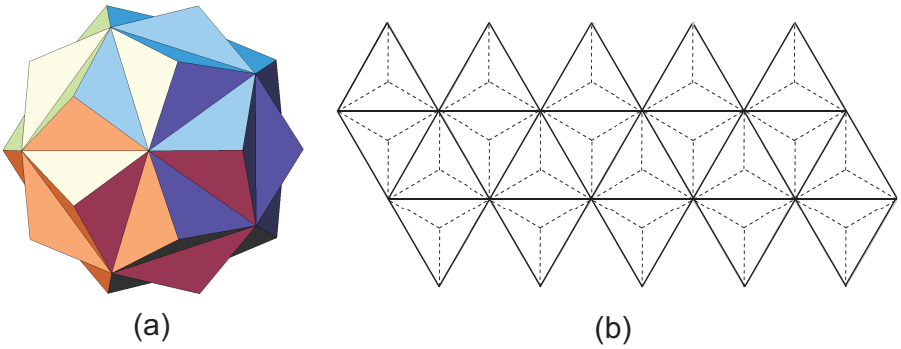

Figure 6.4: (a) Top view of a triambic icosahedron (from Wikipedia). (b) The solid lines correspond to the folding pattern of an icosahedron, and the dash lines are projections of the edges of pyramids on the faces of icosahedron.

17 equally spaced values of heights of pyramids between $-2H_0$ and $2H_0$ were analyzed in the present study. H_0 is the distance between the center of an icosahedral face and the circumscribed sphere. Therefore, the pyramid apexes are on the circumscribed sphere if the height is H_0. Negative heights correspond to concave pyramids. The results are summarized in Fig.6.5.

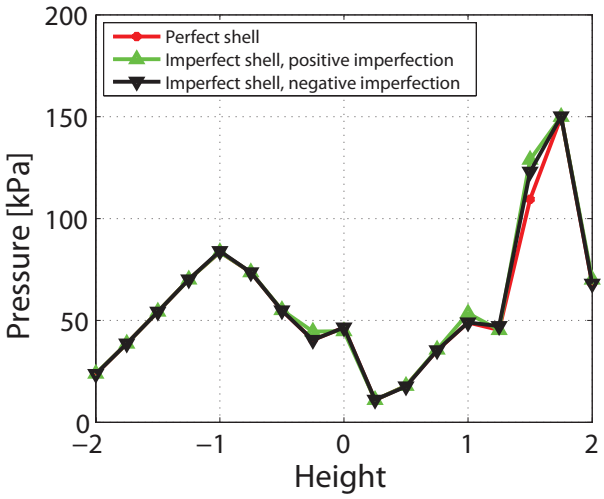

Figure 6.5: Buckling pressures of triambic pyramids with various heights of pyramids.

The buckling pressures of the imperfect shells are very close to those of the perfect shells. Therefore, the triambic icosahedra are not sensitive to imperfections. The shell with pyramid height of $1.75H_0$ has the highest buckling pressures: $P_0 = 149.970$ kPa, $P_+ = 149.965$ kPa, and $P_- = 150.105$ kPa. Its buckling pressure is 79% and 493% higher than the buckling pressures of the perfect and imperfect spherical shells, respectively. The knockdown factor is 1.000, 230% higher than the knockdown factor of the spherical shell.

The buckling modes of triambic icosahedra with convex and concave pyramids are different, as shown in Fig. 6.6. The buckling modes of triambic icosahedra with concave pyramids are localized on several faces. The buckling mode of the icosahedron is more global and each face has a half wave. However, as the heights of pyramids increase to a large positive value, the wavelength of the buckling modes decreases. The buckling mode of triambic icosahedron with $H = 1.75H_0$ has a full wave on each face.

6.3 Optimization

The triambic icosahedron with pyramid height of $1.75H_0$ was chosen as the starting design of optimizations. It was found that each simulation of externally pressurized shells required around 30 minutes, much slower than the axially compressed cylindrical shells. Therefore, only a small number of design variables was used in the present study to reduce the total computational time of optimizations. The simulation technique used in optimizations was the same as that presented in Section 6.1.2. The optimization algorithm was CMA-ES.

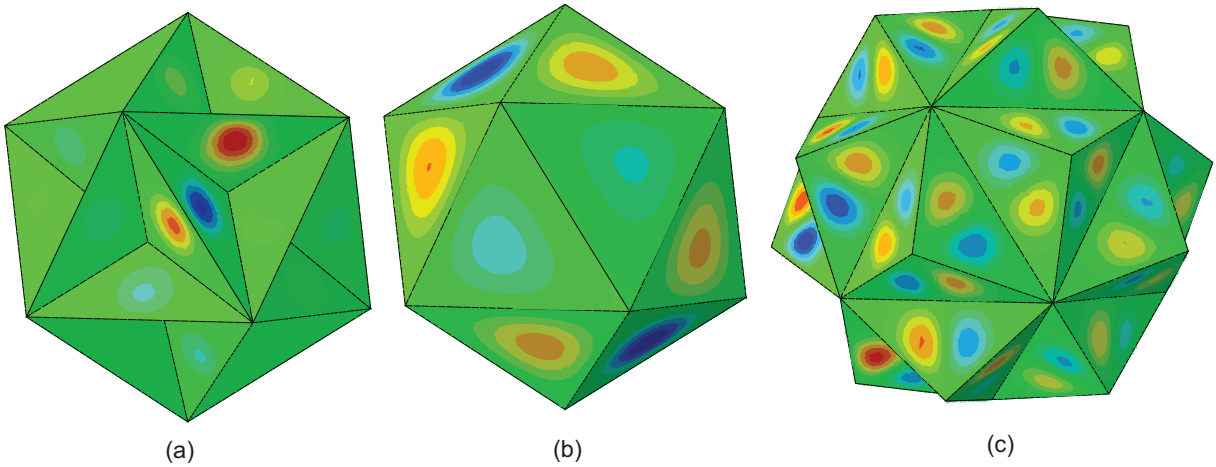

Figure 6.6: Buckling modes of (a) triambic icosahedron with $H = -H_0$, (b) icosahedron, and (c) triambic icosahedron with $H = 1.75H_0$. Red regions represent outward deformation.

6.3.1 Optimization 1: Positions of Pyramid Apexes

6.3.1.1 Design Variables

The height of a pyramid, i.e., the distance between its apex and base, was $1.75H_0$ and remained unchanged during this optimization. The position of the apex of each pyramid was uniquely defined by the position of its projection on the base. Fig. 6.7 explains the method for parameterizing the geometry. The point O_i is the projection of the i^{th} pyramid apex on the corresponding triangular bases.

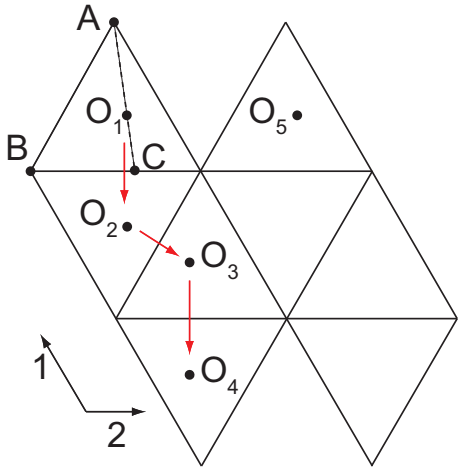

Figure 6.7: Parametrization of shell geometry. This figure is the 2D pattern of the bases of pyramids, and only 8 triangular bases are shown here.

The position of O_1 can be found if the lengths of line segments $\overline{BC}$ and $\overline{AO_1}$ are known. Two geometric constraints were introduced to reduce the number of design variables. First, a mirror symmetry along the 1-direction was used to find the positions of projections of apexes. For example, the projections O_2 and O_1 are mirror-symmetric with respect to $\overline{BC}$. The positions of O_3 and O_4 can be found following the same

rule of mirror symmetry. The red arrows represent the sequence of mirroring the positions of projections. Second, a translational symmetry along the 2-direction was used. For example, the relative position between O_5 and its triangular base was the same as that between O_1 and its triangular base. Therefore, the only design variables in this optimization were the lengths of $\overline{BC}$ and $\overline{AO_1}$.

6.3.1.2 Results

Similar to the optimizations in Chapter 3, $min(P_0, P_+, P_1)$ was maximized by CMA-ES. Four individuals were used for each generation in this optimization, and the program was run for 100 generation. The evolution of buckling pressures and design variables during optimization was plotted in Fig. 6.8. X_1 and X_2 are normalized lengths of $\overline{BC}$ and $\overline{AO_1}$, i.e., $X_1 = \overline{BC}/\overline{AB}$ and $X_2 = \overline{AO_1}/\overline{AC}$.

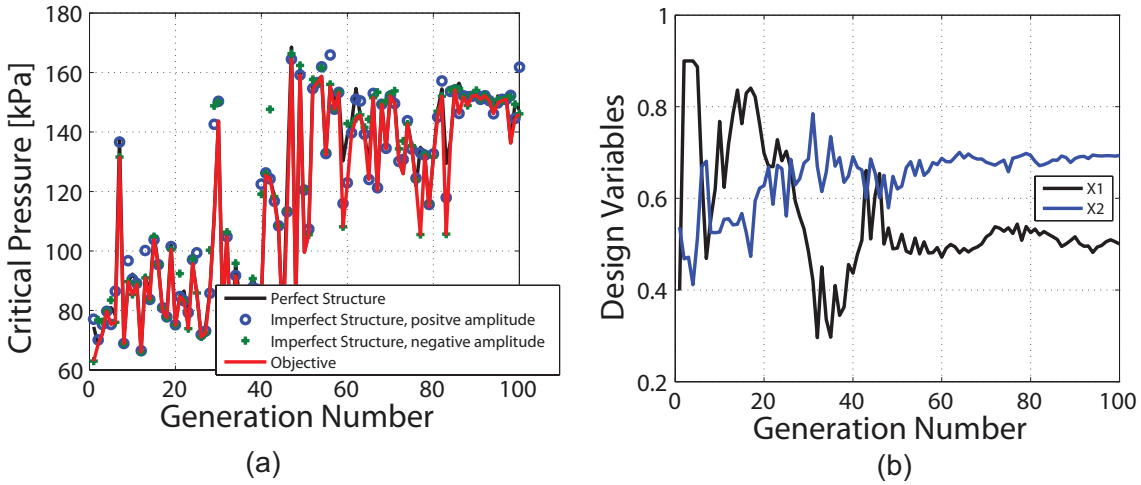

Figure 6.8: Evolution of (a) buckling pressures and (b) design variables during optimization 1.

The optimum was found at the 47^{th} generation. The corresponding buckling pressure, $min(P_0, P_+, P_1)$, and knockdown factor are 164.444 kPa and 0.976, respectively. Compared to the triambic icosahedron with pyramid height of $1.75H_0$, the buckling pressure was increased by 9.656%. The knockdown factor was very close to one, indicating that the optimal shell was not sensitive to imperfections. The optimal design variables are $X_1 = 0.500$ and $X_2 = 0.650$. Note that the center of the triangular base is at $X_1 = 0.500$ and $X_2 = 2/3$. Therefore, the optimal design is very close to the triambic icosahedron.

6.3.2 Optimization 2: Positions and Heights of Pyramid Apexes

The positions and heights of pyramid apexes were optimized. The method of defining the positions of O_i was the same as that in the Section 6.3.1. The heights of all pyramids were the same. Therefore, there were three design variables in this optimization: X_1, X_2, and height H. The height is constrained to be between 0 and $2H_0$, i.e., the pyramids were always convex. Six individuals were used in each generation and the program was run for 50 generations. The results are shown in Fig. 6.9.

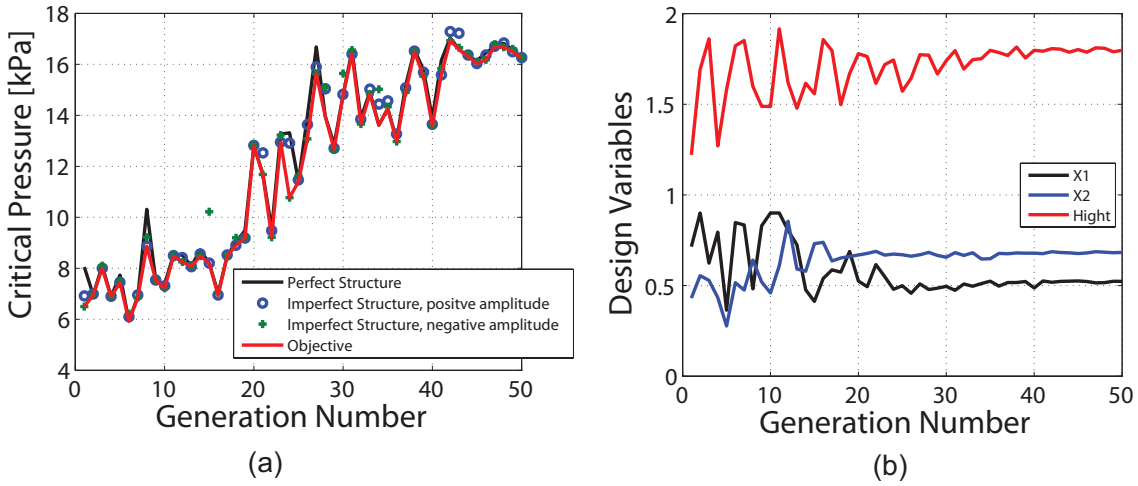

Figure 6.9: Evolution of (a) buckling pressures and (b) design variables during optimization 2. Note that the height is normalized by H_0.

The optimum was found at the 42^{nd} generation. The corresponding buckling pressure, $min(P_0, P_+, P_1)$, and knockdown factor are 169.254 kPa and 0.993, respectively. Compared to the triambic icosahedron with pyramid height of $1.75H_0$, the buckling pressure is increased by 12.860%. The optimal design is not sensitive to imperfections. The optimal design variables are $X_1 = 0.518$, $X_2 = 0.686$, and $H = 1.806H_0$. The position of projection of pyramid apex was close to the center of the triangular base. However, the height was larger than the best triambic icosahedron with $H = 1.75H_0$.

6.3.3 Optimization 3: Constrained Positions and Heights of Pyramid Apexes

In the optimization in Section 6.3.1 O_1 was able to move in two directions within the triangular base. In the optimization of this section O_1 was constrained to move only in the vertical direction. X_1 was set as 0.5. Fig. 6.10 explains the method of parameterizing the geometry. The point O_i is the projection of apexes of the i^{th} triangular bases.

The projections O_i can only move along the dash lines which are perpendicular bisectors of the triangular bases. The distance between O_i and A_i was X_2. A translational symmetry along the 2-direction was used. The relative position between O_5 and its triangular base was the same as the one between O_1 and its triangular base. The design variables in this optimization were X_2 and pyramid height H.

Four individuals were used in each generation and the program was run for 50 generations. The results are shown in Fig. 6.11. The optimum was found at the 39^{th} generation. The corresponding buckling pressure, $min(P_0, P_+, P_1)$, and knockdown factor are 161.950 kPa and 0.998, respectively. The buckling pressure is slightly smaller than the shell obtained in Section 6.3.2. The optimal design is not sensitive to imperfections. The optimal design variables are $X_2 = 0.649$ and $H = 1.809H_0$.

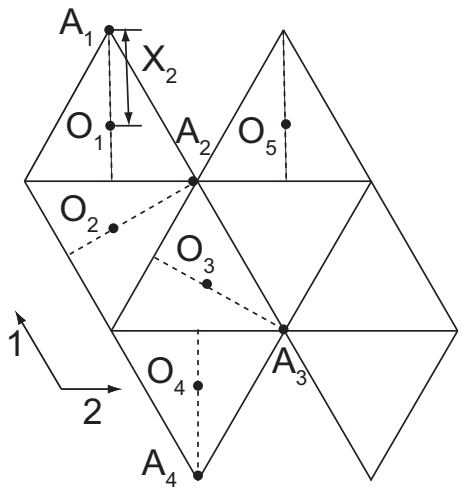

Figure 6.10: Parametrization of shell geometry. This figure is the 2D pattern of the bases of pyramids, and only 8 triangular bases are shown here.

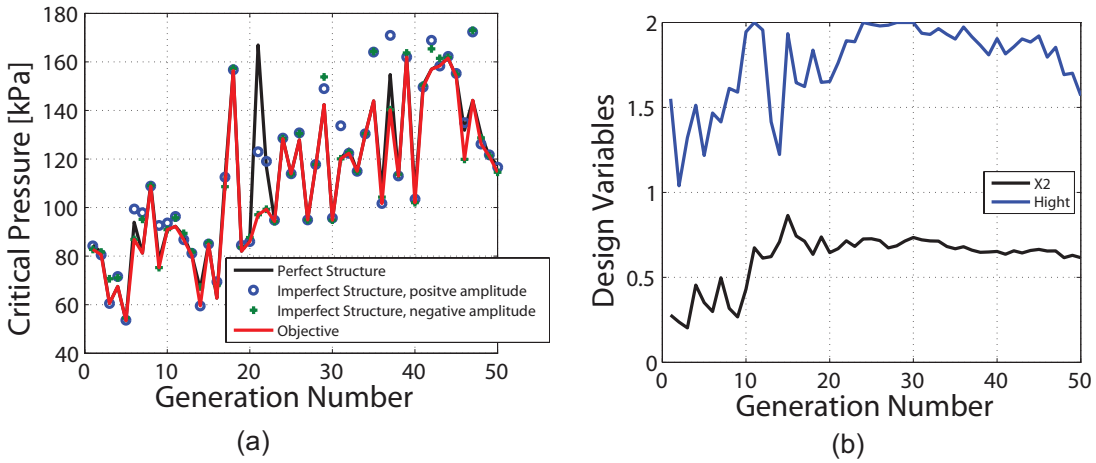

Figure 6.11: Evolution of (a) buckling pressures and (b) design variables during optimization. Note that the height is normalized by H_0.

6.4 Summary

Pseudo-spherical shells, i.e., polyhedral shells, were analyzed and optimized in this chapter. The buckling pressures and knockdown factors of an icosahedron and two geodesic shells were first computed. It was found that the buckling pressures of both perfect and imperfect geodesic shells decreased as the order of subdivision increased. Triambic icosahedra with various heights of pyramids were then studied. It was found that the triambic icosahedron with pyramid height of $H = 1.75H_0$ had highest buckling pressure.

A series of optimizations were performed with the best triambic icosahedron as the initial design. The best design was obtained in the optimization with the positions and heights of pyramid apexes as design variables. The buckling pressure of this optimal design is 102% and 569% higher than the perfect and imperfect spherical shells, respectively. The optimal designs obtained in this chapter were very close to the best triambic icosahedron with $H = 1.75H_0$. Compared to the best triambic icosahedron, the best optimal design improved the buckling pressure by 12.86%. All the pseudo-spherical shells in this chapter were not sensitive to imperfections.

Chapter 7

Conclusion

This thesis has presented a novel method to design imperfection-insensitive symmetry-breaking (wavy) cylindrical shells subject to axial compression. The method employs an optimization technique to obtain geometric shapes that maximize the minimum between the buckling loads of the geometrically perfect structure and geometrically imperfect structures with positive and negative imperfections.

It has been shown that the wavy cylindrical shells developed with this approach can achieve very high critical stress while also being practically insensitive to geometric imperfections. It has also been shown that designs based on the present approach are comparable to the most efficient stiffened shell designs that have been developed during the past decades.

Comparisons between the optimal wavy shells obtained from the present approach and the periodically corrugated shells have shown that the optimized wavy designs can achieve higher buckling stresses and knockdown factors. It has been found that the mass efficiency of periodically corrugated shells cannot exceed a certain limit even with a large number of corrugations. In contrast, the optimal wavy shells are more efficient than this limit value of the periodically corrugated shells. These comparisons have justified that breaking the symmetry of cylindrical shells through optimization can significantly improve the performance of axially compressed cylindrical shells.

The method of obtaining imperfection-insensitive wavy cylindrical shells has been validated by experiments on three composite wavy shells. A fabrication technique was developed to make composite wavy cylindrical shells, and a novel photogrammetry technique was developed to measure the full-field geometric imperfections. The experimental behavior of composite wavy shells was predicted based on measured thickness and mid-plane imperfections. The predictions have shown that the postbuckling of wavy shells is nearly stable, leading to the imperfection-insensitive feature of the wavy shells. The predictions have also shown that the wavy shells collapse due to material failure rather than buckling.

Compression tests on three wavy shells and two circular cylindrical shells have been carried out. It has been found that all three wavy shells were able to reach 100% of the buckling load of a perfect wavy shell and then continue to carry higher load. The difference among the failure loads of the wavy shells was only 3.4%, and discrepancy between the measured and predicted failure loads was less than 4.1%. Significant

delamination was observed after unloading for all wavy shells. This observation and the videos recored by high-speed camera confirmed that the wavy shells collapsed due to material failure. The measured average buckling load of the circular cylindrical shells was only 19.3% of the average failure load of the wavy shells. The highest knockdown factor of the circular shells was only 0.589. Comparisons between the experiments of the wavy shells and circular shells have shown that introducing optimal symmetry-breaking wavy cross-section can significantly reduce the imperfection-sensitivity and improve the load-bearing capability of cylindrical shells.

This thesis has demonstrated the effects of breaking the symmetry of cylindrical shells by using wavy cross-sections with uniform thickness. It would be interesting to study other ways of breaking symmetry such as using unequally spaced stiffeners for stiffened shells. Recently, the development of variable angle tow technology has enabled us to construct composite shells with variable material properties. This technology permits us to investigate the effects of breaking the symmetry of material distribution.

It should be noted that our proposed method did not consider the effects of material failure. It would be interesting to include the limit of material strength in optimizations in the future. This thesis is mainly focused on cylindrical shells under axial compression because the imperfection sensitivity for axial compressed cylinders is higher than the other loading conditions. An important direction for the future work is to extend the current design method to external pressure, shearing, bending, and combined loading conditions.

This thesis has proposed an efficient computational method for the buckling analysis of corrugated and stiffened cylindrical shells that builds on the Bloch wave method and the stiffness matrix method of rotationally periodic structures. The traditional Bloch wave method for infinitely 2- or 3-dimensional periodic structures has been modified in order to analyze the buckling of rotationally periodic shell structures subject to axial compression. A highly efficient algorithm has been developed to implement the modified Bloch wave method.

The modified Bloch wave method was used to analyze the onset of buckling for several small corrugated composite cylindrical shells and a large-scale orthogonally stiffened aluminum cylindrical shell. Compared to the nonlinear full FEA models, the errors of the buckling loads obtained by the modified Bloch wave method are smaller than 0.6% for all the shells studied in this thesis. Numerical examples have also shown that the modified Bloch wave method can produce the same buckling modes as those obtained from the nonlinear full FEA models and that it can accurately capture local (short wavelength) and global (long wavelength) buckling modes. It has been found that for a shell with 40 corrugations the computational time of the modified Bloch wave method is only 7% of the computational time of the linear and nonlinear full FEA models. For the stiffened cylindrical shell, the computational time of the modified Bloch wave method is respectively 50% and 3% of the computational time of the linear and nonlinear full FEA models.

A major constraint that prevented us from optimizing large-scale cylindrical shells was the high computational time. The high computational efficiency of the modified Bloch wave method shows it is promising to use it in the optimization of large-scale cylindrical shells with many corrugations or stiffeners. It should be

noted the modified Bloch wave method is applied on a repeating unit portion such as a single corrugation. However, practical imperfections are usually not periodic and their wavelength may be much larger than a repeating unit portion. Therefore, it is worth investigating the Bloch wave method for imperfect or nearly perfect structures in the future.

This thesis has performed parametric studies on a series of externally pressurized pseudo-spherical shells, i.e., polyhedral shells, including icosahedron, geodesic shells, and triambic icosahedra. Optimizations have also been performed in order to further improve the performance of pseudo-spherical shells under external pressure. It has been shown that the buckling pressure of the best design obtained through the optimizations is 102% and 569% higher than the perfect and imperfect spherical shells, respectively. It has also been found that all the pseudo-spherical shells in this thesis are not sensitive to imperfections.

It should be noted that the numbers of design variables were chosen to be very small in all the optimizations of pseudo-spherical shells in order to reduce the computational time. Therefore, the search space for the optimizations was highly constrained. Expanding the search space would possibly further improve the results of optimizations. For example, the height and positions of each tetrahedron could be independent design variables. In the present study all the designs were based on an icosahedron. It would be interesting to investigate other polyhedra in the future. So far, only numerical studies were performed in this study. An important follow-on work would be the development of manufacturing technique for pseudo-spherical shells and their experimental studies. A potential application of this study is lighter-than-air vehicle with internal vacuum, i.e. vacuum balloon. This would be an interesting direction for the future work.

Bibliography

Aberg, M. and Gudmundson, P. (1997). The usage of standard finite element codes for computation of dispersion relations in materials with periodic microstructure. *The Journal of the Acoustical Society of America*, 102(4).

Agarwal, B. D., Broutman, L. J., and Chandrashekhara, K. (2006). *Analysis and performance of fiber composites*. John Wiley & Sons, Hoboken, NJ.

Agarwal, B. L. and Sobel, L. H. (1977). Weight optimized stiffened, unstiffened, and sandwich cylindrical shells. *Journal of Aircraft*, 14:1000–1008.

Almroth, B. O., Holmes, A. M. C., and Brush, D. O. (1964). An experimental study of the bucking of cylinders under axial compression. *Experimental Mechanics*, 4(9).

Amazigo, J. C. and Hutchinson, J. W. (1967). Imperfection-sensitivity of eccentrically stiffened cylindrical shells. *AIAA Journal*, 5(3).

Anderson, M. S., Williams, F. W., and Wright, C. J. (1983). Buckling and vibration of any prismatic assembly of shear and compression loaded anisotropic plates with an arbitrary supporting structure. *International Journal of Mechanical Sciences*, 25(8).

Araar, M. (1990). *Contribution à L'autoraidissage des Coques Cylindriques vis-à-vis du Flambage*. PhD thesis, INSA de Lyon.

Araar, M., Derbali, M., and Jullien, J. F. (1998). Buckling of the multi-vaulted aster shell under axial compression alone or combined with an external pressure. *Structural Engineering and Mechanics*, 6(7):827–839.

Arbocz, J. and Babcock Jr, C. D. (1968). Experimental investigation of the effect of general imperfections on the buckling of cylindrical shells. Technical Report NASA CR-1163.

Arbocz, J. and Williams, J. G. (1977). Imperfection surveys on a 10-ft diameter shell structure. *Imperfection Surveys on a 10-ft Diameter Shell Structure*, 15(7):949–956.

Babcock, C. D. (1962). *The Buckling of Cylindrical Shells with An Initial Imperfection under Axial Compression Loading*. PhD thesis, California Institute of Technology.

Bäck, T. (1996). *Evolutionary Algorithm in Theory and Practice: Evolution Strategies, Evolutionary Programming, Genetic Algorithms*. Oxford University Press, Oxford.

Bertoldi, K., Boyce, M. C., Deschanel, S., Prange, S. M., and Mullin, T. (2008). Mechanics of deformation-triggered pattern transformations and superelastic behavior in periodic elastomeric structures. *Journal of the Mechanics and Physics of Solids*, 56(8):2642–2668.

Bisagni, C. and Vescovini, R. (2009). Fast tool for buckling analysis and optimization of stiffened panels. *Journal of Aircraft*, 46(6):2041–2053.

Block, D. L., Card, M. F., and Mikulas Jr, M. M. (1965). Buckling of eccentrically stiffened orthotropic cylinders. Technical Report NASA-TN-D-2960.

Briassoulis, D. (1989). Equivalent orthotropic properties of corrugated sheets. *Computers and Structures*, 23(2):129–138.

Brush, D. O. and Almroth, B. O. (1975). *Buckling of Bars, Plates, and Shells*. McGraw-Hill, New York.

Bushnell, D. (1967). Nonlinear axisymmetric behavior of shells of revolution. *AIAA Journal*, 5(3):432–439.

Bushnell, D. (1985). *Computerized Buckling Analysis of Shells*. Martinus Nijhoff Publishers, Dordrecht.

Calladine, C. R. (1989). *Theory of Shell Structures*. Cambridge University Press, Cambridge, UK.

Card, M. F. (1964a). Bending tests of large diameter cylinders susceptible to general instability. Technical Report NASA TN D-2200.

Card, M. F. (1964b). Preliminary results of compression tests on cylinders with eccentric longitudinal stiffeners. Technical Report NASA TM X-1004.

Card, M. F. and Jones, R. M. (1966). Experimental and theoretical results for buckling of eccentrically stiffened cylinders. Technical Report NASA TN D-3639.

Cartalas, C., Van der Hoeven, H. J. C., and Klompé, A. W. H. (1990). Guide to the data reduction of imperfection surveys on circular shells. Technical Report Memorandum M-622, Delft University of Technology, Delft, Netherlands.

Combescure, A. and Pernette, E. (1989). Linear and nonlinear buckling of discrete supported cooling towers using special axisymmetric shell elements. *Nuclear Engineering and Design*, 111(2):217–225.

Daniel, I. M. and Ishai, O. (2006). *Engineering Mechanics of Composite Materials*. Oxford University Press, Oxford.

Davis, R. (1982). Buckling test of a 3-meter-diameter corrugated graphite-epoxy ring-stiffened cylinder. Technical Report NASA TP-2032.

Donnell, L. H. and Wan, C. C. (1950). Effects of imperfections on buckling of thin cylinders and columns under axial compression. *Journal of Applied Mechanics*, 17:73–83.

Dowling, P. J. and Harding, J. E. (1982). Experimental behaviour of ring and stringer stiffened shells. In Harding, J., Dowling, P. J., and Agelidis, N., editors, *Buckling of Shells in Offshore Structures*, pages 73–107, Granada, London.

Elishakoff, I. (2012). Probabilistic resolution of the twentieth century conundrum in elastic stability. *Thin-Walled Structures*, 59:35–57.

EosSystems (2004). *PhotoModeler Pro 6, User Manual*.

Geymonat, G., Müller, S., and Triantafyllidis, N. (1993). Homogenization of nonlinearly elastic materials, microscopic bifurcation and macroscopic loss of rank-one convexity. *Archive for rational mechanics and analysis*, 122(3):231–290.

Gong, L., Kyriakides, S., and Triantafyllidis, N. (2005). On the stability of kelvin cell foams under compressive loads. *Journal of the Mechanics and Physics of Solids*, 53(4):771–794.

Hansen, N. (2011). *The CMA Evolution Strategy: A Tutorial*.

Hansen, N. (2012). The cma evolutionary strategy.

Hansen, N., Müller, S. D., and Koumoutsakos, P. (2003). Reducing the time complexity of the derandomized evolution strategy with covariance matrix adaptation (cma-es). *Evolutionary Computation*, 11:1–18.

Hilburger, M. W. (2012). Developing the next generation shell buckling design factors and technologies. In *53rd AIAA/ASME/ASCE/AHS/ASC Structures, Structural Dynamics and Materials Conference*, Honolulu, HI.

Hilburger, M. W., Haynie, W. T., Lovejoy, A. E., Roberts, M. G., Norris, J. P., Waters, W. A., and Herring, H. M. (2012a). Subscale and full-scale testing of buckling-critical launch vehicle shell structures. In *53rd AIAA/ASME/ASCE/AHS/ASC Structures, Structural Dynamics and Materials Conference*, Honolulu, HI. AIAA-2012-1688.

Hilburger, M. W., Lovejoy, A. E., Thornburgh, R. P., and Rankin, C. (2012b). Design and analysis of subscale and full-scale buckling-critical cylinders for launch vehicle technology development. In *53rd AIAA/ASME/ASCE/AHS/ASC Structures, Structural Dynamics and Materials Conference*, Honolulu, HI.

Hilburger, M. W., Nemeth, M. P., and Starnes, J. H. (2006). Shell buckling design criteria based on manufacturing imperfection signatures. *AIAA Journal*, 44:654–663.

Hilburger, M. W. and Starnes Jr, J. H. (2001). High-fidelity nonlinear analysis of compression-loaded composite shells. In *42nd AIAA/ASME/ASCE/AHS/ASC Structures, Structural Dynamics and Materials Conference*, Seattle, WA. AIAA-2001-1394.

Hughes, T. J. R., Cottrell, J. A., and Bazilevs, Y. (2009). *Isogeometric Analysis: CAD, Finite Elements, NURBS, Exact Geometry and Mesh Refinement.* Wiley, New York.

Hutchinson, J. W. (1967). Imperfection sensitivity of externally pressurized spherical shells. *Journal of Applied Mechanics*, 34(1):49–55.

Hutchinson, J. W. and Koiter, W. T. (1970). Postbuckling theory. *Applied Mechanics Reviews*, 23:1353–1366.

Johnson, R. (1978). Design and fabrication of a ring-stiffened graphite-epoxy corrugated cylindrical shell. Technical Report NASA Contractor Report 3026.

Jones, R. M. (2006). *Buckling of Bars, Plates, and Shells.* Bull Ridge, Blacksburg.

Jullien, J. F. and Araar, M. (1991). Towards an optimal cylindrical shell structures under external pressure. In Jullien, J., editor, *Buckling of Shell Structures, on Land, in the Sea, and in the Air*, pages 21–32. Elsevier, London.

Kaplan, A. (1974). Buckling of spherical shells. In Fung, Y. C. and Sechler, E. E., editors, *Thin Shell Structures, Theory, Experiment, and Design*, pages 248–288. Prentice-Hall, Inc., Englewood Cliffs, NJ.

Katz, L. (1965). Compression tests on integrally stiffened cylinders. Technical Report NASA TM X- 53315.

Kittel, C. and McEuen, P. (1976). *Introduction to solid state physics (Vol. 8).* Wiley, New York.

Knapp, R. H. (1974). Numerical and experimental analysis of a pseudo-cylindrical shell. In *IASS/CISM Symposium on Folded Plates and Spatial Panel Structures, Udine, Italy*, pages 23–35.

Knapp, R. H. (1977). Pseudo-cylindrical shells: a new concept for undersea structures. *Journal of Manufacturing Science and Engineering*, 99(2):485–492.

Koga, T. and Hoff, N. J. (1969). The axisymmetric buckling of initially imperfect complete spherical shells. *International Journal of Solids and Structures*, 5(7):679–697.

Koiter, W. (1969). Nonlinear buckling problem of a complete spherical shell under uniform external pressure. i. *PROCEEDINGS OF THE KONINKLIJKE NEDERLANDSE AKADEMIE VAN WETENSCHAPPEN SERIES B-PHYSICAL SCIENCES*, 72(1):40.

Koiter, W. T. (1945). *On the Stability of Elastic Equilibrium.* PhD thesis, TU Delft. H.J. Paris, Amsterdam. English translation, Air Force Flight Dym. Lab. Tech. Rep., AFFDL-TR-70-25.

Koiter, W. T. (1963). The effect of axisymmetric imperfections on the buckling of cylindrical shells under axial compression. *Proc. K. Ned. Akad. Wet.*, 6. also, Lockheed Missiles and Space Co. Rep. 6-90-63-86, Palo Alto, California.

Krenzke, M. A. (1962). Tests of machined deep spherical shells under external hydrostatic pressure. Technical Report DTMB-1601, The David Taylor Model Basin, Washington, D.C.

Krenzke, M. A. and Kiernan, T. J. (1963). Tests of stiffened and unstiffened machined spherical shells under external hydrostatic pressure. Technical Report DTMB-1741, The David Taylor Model Basin, Washington, D.C.

Lamberti, L., Venkataraman, S., Haftka, R. T., , and Johnson, T. F. (2003). Preliminary design optimization of stiffened panels using approximate analysis models. *International Journal for Numerical Methods in Engineering*, 57(10):1351–1380.

Liew, K. M., Peng, L. X., and Kitipornchai, S. (2007). Nonlinear analysis of corrugated plates using a fsdt and a meshfree method. *Computer Methods in Applied Mechanics and Engineering*, 196(21):2358–2376.

Limam, A., Jullien, J. F., Greco, E., and Lestrat, D. (1991). Buckling of thin-walled cylinders under axial compression and internal pressure. In Jullien, J., editor, *Buckling of Shell Structures, on Land, in the Sea, and in the Air*, pages 359–369, London.

Lockheed Martin Company (2009). Space shuttle external tank fact sheet. Complied by Lockheed Martin Space Systems Company.

Lpez Jimnez, F. and Triantafyllidis, N. (2013). Buckling of rectangular and hexagonal honeycomb under combined axial compression and transverse shear. *International Journal of Solids and Structures*, 50(24):3934–3946.

NASA (1968). Saturn v news reference: First stage fact sheet.

NASA-SP-8032 (1969). Buckling of thin-walled doubly curved shells. Technical Report NASA SP-8032.

Nemeth, M. and Mikulas, M. M. (2009). Simple formulas and results for buckling-resistance and stiffness design of compression-loaded laminated-composite cylinders. Technical Report NASA TP-2009-215778.

Nemeth, M. P. and Starnes, J. H. (1998). The nasa monographs on shell stability design recommendations: a review and suggested improvements. Technical Report NASA TP-1998-206290.

Ning, X. and Pellegrino, S. (2012). Design of lightweight structural components for direct digital manufacturing. In *53rd AIAA/ASME/ASCE/AHS/ASC Structures, Structural Dynamics and Materials Conference*, Honolulu, HI. AIAA-2012-1807.

Ning, X. and Pellegrino, S. (2013). Imperfection-insensitive axially loaded cylindrical shells. In *54th AIAA/ASME/ASCE/AHS/ASC Structures, Structural Dynamics and Materials Conference*, Boston, MA. AIAA-2013-1768.

Ning, X. and Pellegrino, S. (2015a). Buckling analysis of axially loaded corrugated cylindrical shells. In *56th AIAA/ASME/ASCE/AHS/ASC Structures, Structural Dynamics and Materials Conference*, Kissimmee, FL. AIAA-2015-1435.

Ning, X. and Pellegrino, S. (2015b). Imperfection-insensitive axially loaded thin cylindrical shells. *International Journal of Solids and Structures*. In press.

Öry, H., Reimerdes, H.-G., Schmid, T., Rittweger, A., and Garcıa, J. G. (2002). Imperfection sensitivity of an orthotropic spherical shell under external pressure. *International journal of non-linear mechanics*, 37(4):669–686.

Pan, B. and Cui, W. (2010). An overview of buckling and ultimate strength of spherical pressure hull under external pressure. *Marine Structures*, 23(3):227–240.

Peterson, J. P. (1967). Structural efficiency of ring-stiffened corrugated cylinders in axial compression. Technical Report NASA TN D-1073.

Peterson, J. P., Seide, P., and Weingarten, V. I. (1965). Buckling of thin-walled circular cylinders. Technical Report NASA SP-8007.

Ramm, E. and Wall, W. A. (2004). Shell structures − a sensitive interrelation between physics and numerics. *International Journal for Numerical Methods in Engineering*, 60:381–427.

Reitinger, R., Bletzinger, K. U., and Ramm, E. (1994). Shape optimization of buckling sensitive structures. computing systems in engineering. *Computing Systems in Engineering*, 5:65–75.

Reitinger, R. and Ramm, E. (1995). Buckling and imperfection sensitivity in the optimization of shell structures. *Thin-walled Structures*, 23:159–177.

Rotter, J. M., Coleman, R., Ding, X. L., and Teng, J. G. (1992). The measurement of imperfections in cylindrical silos for buckling strength assessment. In *Proceedings of 4th International Conference on Bulk Materials, Storage, Handling and Transportation*, pages 473–479, Wollongong, Australia.

Sabir, A. (1964). Large deflection and buckling behaviour of a spherical shell with inward point load and uniform external pressure. *Journal of Mechanical Engineering Science*, 6(4):394–404.

Scott, N. D., Harding, J. E., and Dowling, P. J. (1987). Fabrication of small scale stiffened cylindrical shells. *Journal of Strain Analysis*, 22:97–106.

Sendelbeck, R. L. (1964). The manufacture of thin shells by the electroforming process. Technical Report SUDEAR Report No. 185, Stanford University, Stanford, California.

Shim, J., Shan, S., Komrlj, A., Kang, S. H., Chen, E. R., Weaver, J. C., and Bertoldi, K. (2013). Harnessing instabilities for design of soft reconfigurable auxetic/chiral materials. *Soft Matter*, 9(34):8198–8202.

Simitses, G. J. (1971). General instability of eccentrically stiffened cylindrical panels. *Journal of Aircraft*, 8(7):569575.

Singer, J., Arbocz, J., and Weller, T. (2002a). *Buckling Experiments: Experimental Methods in Buckling of Thin-Walled Structures: Vol. 1.* Wiley, New York.

Singer, J., Arbocz, J., and Weller, T. (2002b). *Buckling Experiments: Experimental Methods in Buckling of Thin-Walled Structures: Vol. 2.* Wiley, New York.

Sleight, D., Sreekantamurthy, T., Kosareo, D. N., Martin, R. A., and Johnson, T. F. (2011). Structural design of ares v interstage composite structure. In *52nd AIAA/ASME/ASCE/AHS/ASC Structures, Structural Dynamics and Materials Conference*, Denver, CO. AIAA-2011-1790.

Teng, J. G. (1996). Buckling of thin shells: Recent advances and trends. *Applied Mechanics Reviews*, 49(4):263–274.

The North Thin Ply Company (2013). *ThinPreg 120 EPHTg/CF Product Datasheet.*

Thill, C., Etches, J. A., Bond, I. P., Potter, K. D., Weaver, P. M., and Wisnom, M. R. (2010). Investigation of trapezoidal corrugated aramid/epoxy laminates under large tensile displacements transverse to the corrugation direction. *Composites Part A: Applied Science and Manufacturing*, 41(1):168–176.

Thompson, J. (1962). The elastic instability of a complete spherical shell. *Aeronautical Quarterly*, 13(2):189–201.

Thompson, J. (1964a). The post-buckling of a spherical shell by computer analysis. In *Proc. World Conference on Shell Structures, National Academy of Sciences, Washington.*

Thompson, J. (1964b). The rotationally-symmetric branching behaviour of a complete spherical shell. *Koninkl. Ned. Akad. Wetenschap*, B67:295–311.

Timoshenko, S. and Gere, J. (1961). *Theory of Elastic Stability. 2.ed.* McGraw-Hill, New York, NY.

Triantafyllidis, N. and Schnaidt, W. C. (1993). Comparison of microscopic and macroscopic instabilities in a class of two-dimensional periodic composites. *Journal of the Mechanics and Physics of Solids*, 41(9):1533–1565.

Triantafyllidis, N. and Schraad, M. W. (1998). Onset of failure in aluminum honeycombs under general in-plane loading. *Journal of the Mechanics and Physics of Solids*, 46(6):1089–1124.

Tsien, H. S. (1942). A theory for the buckling of thin shells. *Journal of the Aeronautical Sciences*, 9:373–384.

United Launch Alliance (2009). Delta iv (5-meter) fact sheet. Complied by United Launch Alliance.

Ventsel, E. and Krauthammer, T. (2001). *Thin plates and shells: theory: analysis, and applications*. CRC press, New York, NY.

Verduyn, W. D. and Elishakoff, I. (1982). A testing machine for statistical analysis of small imperfect shells: Part i. Technical Report Report LR-357, Delft University of Technology, Delft, Netherlands.

Virgin, L. N. (2007). *Vibration of axially-loaded structures*. Cambridge University Press, Cambridge, UK.

Vision Research (2014). Configuration of phantom v310.

Von Kármán, T. and Tsien, H. (1939). The buckling of spherical shells by external pressure. *Journal of the Aeronautical Sciences*, 7:43–50.

Von Kármán, T. and Tsien, H. (1941). The buckling of thin cylindrical shells under axial compression. *Journal of the Aeronautical Sciences*, 8:303–312.

Wang, D. and Abdalla, M. M. (2015). Global and local buckling analysis of grid-stiffened composite panels. *Composite Structures*, 119:767–776.

Wenninger, M. J. (1974). *Polyhedron models*. Cambridge University Press, Cambridge, UK.

Williams, F. W. (1986a). An algorithm for exact eigenvalue calculations for rotationally periodic structures. *International journal for numerical methods in engineering*, 23(4):609–622.

Williams, F. W. (1986b). Exact eigenvalue calculations for structures with rotationally periodic substructures. *International journal for numerical methods in engineering*, 23(4):695–706.

Williams, F. W. and Anderson, M. S. (1983). Incorporation of lagrangian multipliers into an algorithm for finding exact natural frequencies or critical buckling loads. *International Journal of Mechanical Sciences*, 25(8):579–584.

Williams, F. W., Anderson, M. S., Kennedy, D., Butler, R., and Aston, G. (1990). Viconopt-program for exact vibration and buckling analysis or design of prismatic plate assemblies. Technical Report NASA CR-181966.

Wittrick, W. H. and Williams, F. W. (1974). Buckling and vibration of anisotropic or isotropic plate assemblies under combined loadings. *International Journal of Mechanical Sciences*, 16(4):209–239.

Wu, K. C., Stanford, B. K., Hrinda, G. A., Wang, Z., Martin, R. A., and Kim, H. A. (2013). Structural assessment of advanced composite tow-steered shells. In *54th AIAA/ASME/ASCE/AHS/ASC Structures, Structural Dynamics and Materials Conference*, Boston, MA. AIAA-2013-1769.

Xia, Y., Friswell, M. I., and Flores, E. I. (2012). Equivalent models of corrugated panels. *International Journal of Solids and Structures*, 49(13):1453–1462.

Yamaki, N. and Otomo, K. (1973). Experiments on the postbuckling behavior of circular cylindrical shells under hydrostatic pressure. *Experimental Mechanics*, 17(3):299–304.

Ye, Z., Berdichevsky, V. L., and Yu, W. (2014). An equivalent classical plate model of corrugated structures. *International Journal of Solids and Structures*, 51(11):2073–2083.

Yokozeki, T., Takeda, S., Ogasawara, T., and Ishikawa, T. (2006). Mechanical properties of corrugated composites for candidate materials of flexible wing structures. *Composites Part A: Applied Science and Manufacturing*, 37(10):1578–1586.

Yoshimura, Y. (1951). On the mechanism of buckling of a circular cylindrical shell under axial compression. Technical Report NACA-TM-1390.

Appendix A

Bloch Method for Stiffened/Corrugated Cylindrical Shells

This appendix provides the details of the derivations of the modified Bloch wave method for stiffened/corrugated cylindrical shells.

A.1 Bloch Relations and Coupling Matrix of a 2-Dimensional Infinite Periodic Structure

$\tilde{U}$ and $\tilde{F}$ in Eq. 2.26 can be separated into the values on boundary and internal nodes:

$$\begin{aligned} \tilde{U} &= [\tilde{U}_i, \tilde{U}_a, \tilde{U}_b]^T \\ \tilde{F} &= [\tilde{F}_i, \tilde{F}_a, \tilde{F}_b]^T \end{aligned} \tag{A.1}$$

where i, a and b denote the internal nodes, nodes in regions "a" and "b", respectively, as shown in Fig. 2.11. Therefore, the displacements and forces of regions "a" and "b" are:

$$\begin{aligned} \tilde{U}_a &= [\tilde{U}_{(AD)}, \tilde{U}_A, \tilde{U}_{(AB)}]^T \\ \tilde{F}_a &= [\tilde{F}_{(AD)}, \tilde{F}_A, \tilde{F}_{(AB)}]^T \\ \tilde{U}_b &= [\tilde{U}_B, \tilde{U}_{(BC)}, \tilde{U}_C, \tilde{U}_{(CD)}]^T \\ \tilde{F}_b &= [\tilde{F}_B, \tilde{F}_{(BC)}, \tilde{F}_C, \tilde{F}_{(CD)}]^T \end{aligned} \tag{A.2}$$

The notation $(*)$ means edges without their end nodes.

Using Eqs. 2.23 and 2.28, we can obtain the following Bloch relations for the displacements on the

boundary nodes:

$$U_B = \mu_1 U_A;\quad U_{(BC)} = \mu_1 U_{(AD)};\quad U_C = \mu_1 U_D;\quad U_C = \mu_2 U_B;\quad U_{(CD)} = \mu_2 U_{(AB)};\quad U_D = -\mu_2 U_A \tag{A.3}$$

where $\mu_1 = \exp(2\pi i n_1)$ and $\mu_2 = \exp(2\pi i n_2)$. Similarly, the forces on the boundaries have the following Bloch relations:

$$F_B = -\mu_1 F_A;\quad F_{(BC)} = -\mu_1 F_{(AD)};\quad F_C = -\mu_1 F_D;\quad F_C = -\mu_2 F_B;\quad F_{(CD)} = -\mu_2 F_{(AB)};\quad F_D = -\mu_2 F_A \tag{A.4}$$

Using Eq. A.3, the displacements can be written as:

$$[\tilde{U}_i, \tilde{U}_{(AD)}, \tilde{U}_A, \tilde{U}_{(AB)}, \tilde{U}_B, \tilde{U}_{(BC)}, \tilde{U}_C, \tilde{U}_{(CD)}]^T = Q[\tilde{U}_i, \tilde{U}_{(AD)}, \tilde{U}_A, \tilde{U}_{(AB)}]^T \tag{A.5}$$

where the transformation matrix Q is defined as:

$$Q = \begin{bmatrix} \mathbf{I} & \mathbf{0} & \mathbf{0} & \mathbf{0} \\ \mathbf{0} & \mathbf{I} & \mathbf{0} & \mathbf{0} \\ \mathbf{0} & \mathbf{0} & \mathbf{I} & \mathbf{0} \\ \mathbf{0} & \mathbf{0} & \mathbf{0} & \mathbf{I} \\ \mathbf{0} & \mathbf{0} & [\mu_1] & \mathbf{0} \\ \mathbf{0} & [\mu_1] & \mathbf{0} & \mathbf{0} \\ \mathbf{0} & \mathbf{0} & [\mu_1\mu_2] & \mathbf{0} \\ \mathbf{0} & \mathbf{0} & \mathbf{0} & [\mu_2] \end{bmatrix} \tag{A.6}$$

The notation $[*]$ represents a diagonal submatrix with entries equal to *.

A.2 Bloch Relations and Coupling Matrix of a Rotationally Periodic Structure

$\tilde{U}$ and $\tilde{F}$ in Eqs. 5.3 and 5.4 can be separated into the values on boundary and internal nodes:

$$\begin{aligned} \tilde{U} &= [\tilde{U}_i, \tilde{U}_{(1)}, \tilde{U}_{[2]}, \tilde{U}_{(3)}, \tilde{U}_{[4]}]^T \\ \tilde{F} &= [\tilde{F}_i, \tilde{F}_{(1)}, \tilde{F}_{[2]}, \tilde{F}_{(3)}, \tilde{F}_{[4]}]^T \end{aligned} \tag{A.7}$$

The notations $(*)$ and $[*]$ represent edges respectively without and with their end nodes. The equilibrium equation of a corrugation on the point of buckling is

$$K(\lambda_c)[\tilde{U}_i, \tilde{U}_{(1)}, \tilde{U}_{[2]}, \tilde{U}_{(3)}, \tilde{U}_{[4]}]^T = [\tilde{F}_i, \tilde{F}_{(1)}, \tilde{F}_{[2]}, \tilde{F}_{(3)}, \tilde{F}_{[4]}]^T \tag{A.8}$$

The stiffness matrix $K(\lambda_c)$ and force vector $[\tilde{F}_i, \tilde{F}_{(1)}, \tilde{F}_{[2]}, \tilde{F}_{(3)}, \tilde{F}_{[4]}]^T$ in Eq. A.8 can be assembled into the global stiffness and force vector of the whole corrugated shell, and the following eigenproblem is then obtained:

$$K_c(\lambda)\tilde{U}_c = \tilde{F}_c = 0 \tag{A.9}$$

where K_c and $\tilde{U}_c$ are the global stiffness matrix and the eigenvector of the whole structure.

$\tilde{F}_c$ is zero when the structure buckles. Note that the force vectors F_i, $F_{(1)}$, and $F_{(3)}$ remain unchanged when they are assembled into the force vector in Eq. A.9 because the edges (1), (3), and internal nodes do not interact with the nodes in other corrugations. Therefore, Eq. A.8 can be written as:

$$K(\lambda)[\tilde{U}_i, \tilde{U}_{(1)}, \tilde{U}_{[2]}, \tilde{U}_{(3)}, \tilde{U}_{[4]}]^T = [0, 0, \tilde{F}_{[2]}, 0, \tilde{F}_{[4]}]^T \tag{A.10}$$

The incremental displacements on edge 4 can be eliminated by means of the relation:

$$[\tilde{U}_i, \tilde{U}_{(1)}, \tilde{U}_{[2]}, \tilde{U}_{(3)}, \tilde{U}_{[4]}]^T = Q[\tilde{U}_i, \tilde{U}_{(1)}, \tilde{U}_{[2]}, \tilde{U}_{(3)}]^T \tag{A.11}$$

where Q is

$$Q = \begin{bmatrix} \mathbf{I} & \mathbf{0} & \mathbf{0} & \mathbf{0} \\ \mathbf{0} & \mathbf{I} & \mathbf{0} & \mathbf{0} \\ \mathbf{0} & \mathbf{0} & \mathbf{I} & \mathbf{0} \\ \mathbf{0} & \mathbf{0} & \mathbf{0} & \mathbf{I} \\ \mathbf{0} & \mathbf{0} & [\exp(i\frac{2\pi}{N}n)] & \mathbf{0} \end{bmatrix} \tag{A.12}$$

Letting $[U_i, U_{(1)}, U_{[2]}, U_{(3)}]^T = \tilde{U}_{ind}$, and proceeding in analogy to Eqs 2.31-2.33, we obtain the following eigenproblem:

$$Q^T K(\lambda) Q \tilde{U}_{ind} = \hat{K}(n, \lambda)\tilde{U}_{ind} = Q^T \tilde{F} = 0, \quad n = 0, 1, 2, ..., \{N/2\} \tag{A.13}$$

where λ is the loading factor.

The transformation matrix Q can also be separated into real and imaginary parts based on Eq. 5.12.

$$\begin{bmatrix} U_i^{Re} \\ U_{(1)}^{Re} \\ U_{[2]}^{Re} \\ U_{(3)}^{Re} \\ U_{[4]}^{Re} \\ U_i^{Im} \\ U_{(1)}^{Im} \\ U_{[2]}^{Im} \\ U_{(3)}^{Im} \\ U_{[4]}^{Im} \end{bmatrix} = Q \begin{bmatrix} U_i^{Re} \\ U_{(1)}^{Re} \\ U_{[2]}^{Re} \\ U_{(3)}^{Re} \\ U_i^{Im} \\ U_{(1)}^{Im} \\ U_{[2]}^{Im} \\ U_{(3)}^{Im} \end{bmatrix} \tag{A.14}$$

where Q matrix is

$$\begin{bmatrix} \mathbf{I} & \mathbf{0} & \mathbf{0} & \mathbf{0} & \mathbf{0} & \mathbf{0} & \mathbf{0} & \mathbf{0} \\ \mathbf{0} & \mathbf{I} & \mathbf{0} & \mathbf{0} & \mathbf{0} & \mathbf{0} & \mathbf{0} & \mathbf{0} \\ \mathbf{0} & \mathbf{0} & \mathbf{I} & \mathbf{0} & \mathbf{0} & \mathbf{0} & \mathbf{0} & \mathbf{0} \\ \mathbf{0} & \mathbf{0} & \mathbf{0} & \mathbf{I} & \mathbf{0} & \mathbf{0} & \mathbf{0} & \mathbf{0} \\ \mathbf{0} & \mathbf{0} & [\cos(\frac{2\pi}{N}n)] & \mathbf{0} & \mathbf{0} & \mathbf{0} & -[\sin(\frac{2\pi}{N}n)] & \mathbf{0} \\ \mathbf{0} & \mathbf{0} & \mathbf{0} & \mathbf{0} & \mathbf{I} & \mathbf{0} & \mathbf{0} & \mathbf{0} \\ \mathbf{0} & \mathbf{0} & \mathbf{0} & \mathbf{0} & \mathbf{0} & \mathbf{I} & \mathbf{0} & \mathbf{0} \\ \mathbf{0} & \mathbf{0} & \mathbf{0} & \mathbf{0} & \mathbf{0} & \mathbf{0} & \mathbf{I} & \mathbf{0} \\ \mathbf{0} & \mathbf{0} & \mathbf{0} & \mathbf{0} & \mathbf{0} & \mathbf{0} & \mathbf{0} & \mathbf{I} \\ \mathbf{0} & \mathbf{0} & [\sin(\frac{2\pi}{N}n)] & \mathbf{0} & \mathbf{0} & \mathbf{0} & [\cos(\frac{2\pi}{N}n)] & \mathbf{0} \end{bmatrix} \tag{A.15}$$

The Bloch relations of forces are:

$$\begin{aligned} \tilde{F}_{[4]}^{Re} &= -(\tilde{F}_{[2]}^{Re}\cos(\frac{2\pi}{N}n) - \tilde{F}_{[2]}^{Im}\sin(\frac{2\pi}{N}n)) \\ \tilde{F}_{[4]}^{Im} &= -(\tilde{F}_{[2]}^{Re}\sin(\frac{2\pi}{N}n) + \tilde{F}_{[2]}^{Im}\cos(\frac{2\pi}{N}n)) \end{aligned} \tag{A.16}$$

We can also obtain the following relation by multiplying Eq. 5.11 by Q^T and using the above force Bloch

relations and $F_i = 0$, $F_{(1)} = 0$, and $F_{(3)} = 0$:

$$Q^T \left(\begin{bmatrix} K & \mathbf{0} \\ \mathbf{0} & K \end{bmatrix} - \omega^2 \begin{bmatrix} M & \mathbf{0} \\ \mathbf{0} & M \end{bmatrix} \right) Q \begin{bmatrix} U_i^{Re} \\ U_{(1)}^{Re} \\ U_{[2]}^{Re} \\ U_{(3)}^{Re} \\ U_i^{Im} \\ U_{(1)}^{Im} \\ U_{[2]}^{Im} \\ U_{(3)}^{Im} \end{bmatrix} = Q^T \begin{bmatrix} 0 \\ 0 \\ F_{[2]}^{Re} \\ 0 \\ F_{[4]}^{Re} \\ 0 \\ 0 \\ F_{[2]}^{Im} \\ 0 \\ F_{[4]}^{Im} \end{bmatrix} = 0 \tag{A.17}$$

Appendix B

Matlab Functions for Optimization Program

This appendix provides the details of the Matlab scripts used in the optimizations.

```
%%%%%%%%%%%%%%%%%%%%%%%%%%%%%%%%%%%%%%%%%%%%%%%%%%%%%%%%%%%%
% Function for Running Rhino
function modelstatus=RunRhino(RhinoFolder)
rhinostatus=0; % reset status into initial state for next loop
fid = fopen('rhinostatus.txt', 'w');
fprintf(fid, '%d',rhinostatus);
fclose(fid);
start=[RhinoFolder '/RunScript="-RunPythonScript Run_rhino.py"'];
[status result]=dos([start '&']);
[status result] = dos(['taskkill /IM ' 'cmd.exe'], '-echo');
% wait for the completion of model generating
load rhinostatus.txt
while rhinostatus==0
    disp('Running Rhino')
    pause(1)
    load rhinostatus.txt
end
rhinostatus=0; % reset status into initial state for next loop
fid = fopen('rhinostatus.txt', 'w');
fprintf(fid, '%d',rhinostatus);
fclose(fid);

% Close Rhino window
```

```
Rhino_exe = 'Rhino.exe';
[status result] = dos(['taskkill /IM ' Rhino_exe], '-echo');
disp('*************Finish Generating Model*************')
modelstatus=1;

%%%%%%%%%%%%%%%%%%%%%%%%%%%%%%%%%%%%%%%%%%%%%%%%%%%%%%%%
% Function for creating input files
function FEAstatus=RunAbaqusInpFiles_nonlinear(AbaqusFolder)
disp('************* Writing Inp Files *************')

[status result] = dos(AbaqusFolder{1}, '-echo');
[status result] = dos(AbaqusFolder{2}, '-echo');
abaqus=[AbaqusFolder{3} 'cae noGUI=Run_AbaqusInpFiles_nonlinear.py'];

[status1 result1] = dos(abaqus, '-echo');
disp('************* Finish Writing Inp Files *************')

FEAstatus=1;

%%%%%%%%%%%%%%%%%%%%%%%%%%%%%%%%%%%%%%%%%%%%%%%%%%%%%%%%
% Function for submitting Input files for Abaqus to analysis
function SubmitJob_nonlinear(PerStatus,ind,AbaqusFolder,FOLDER,cpunumber)
if PerStatus==1
    Jobname_buckle={['Ind_' num2str(ind) '_Perfect_buckle']...
,['Ind_' num2str(ind) '_Perfect_Nlbuckle']};
else
    Jobname_buckle={['Ind_' num2str(ind) '_Imperfect_pos_buckle']...
, ['Ind_' num2str(ind) '_Imperfect_neg_buckle']};

end

jobperm=randperm(5);
if jobperm(2)<jobperm(4)
    Jobname_first=Jobname_buckle{1};
    Jobname_second=Jobname_buckle{2};
else
```

```
    Jobname_first=Jobname_buckle{2};
    Jobname_second=Jobname_buckle{1};
end

disp('************** Running jobs **************')

    %%%%%%%%%%%%%%%%%%
    [status result] = dos(AbaqusFolder{1}, '-echo');
    [status result] = dos(AbaqusFolder{2}, '-echo');
    abaqus=[AbaqusFolder{3}...
'job=' ,Jobname_first,' ',cpunumber,' int memory="90 %" output_precision=full double=both'];
    [status1 result1] = dos(abaqus, '-echo');

    %%%%%%% check odb files
    Odb1name=[Jobname_first '.odb'];
    datafilestatus1=FileFind(Odb1name,FOLDER);
    Odb1name_f=[Jobname_first '.odb_f'];
    datafilestatus1_f=FileFind(Odb1name_f,FOLDER);

    if datafilestatus1_f==1 || datafilestatus1==0
% Incomplete odb files exist or good odb files are missing
        [status result] = dos(AbaqusFolder{1}, '-echo');
        [status result] = dos(AbaqusFolder{2}, '-echo');
        abaqus=[AbaqusFolder{3}...
'job=' ,Jobname_first,' ',cpunumber,' int memory="90 %" output_precision=full double=both'];
        [status1 result1] = dos(abaqus, '-echo');
    end

    %%%%%%%%%%%%%%%%%%
    [status result] = dos(AbaqusFolder{1}, '-echo');
    [status result] = dos(AbaqusFolder{2}, '-echo');
    abaqus=[AbaqusFolder{3}...
'job=',Jobname_second,' ',cpunumber,' int memory="90 %" output_precision=full double=both'];
    [status1 result1] = dos(abaqus, '-echo');

    %%%%%%% check odb files
```

```
    Odb2name=[Jobname_second '.odb'];
    datafilestatus2=FileFind(Odb2name,FOLDER);
    Odb2name_f=[Jobname_second '.odb_f'];
    datafilestatus2_f=FileFind(Odb2name_f,FOLDER);

    if datafilestatus2_f==1 || datafilestatus2==0
% Incomplete odb files exist or good odb files are missing
        [status result] = dos(AbaqusFolder{1}, '-echo');
        [status result] = dos(AbaqusFolder{2}, '-echo');
        abaqus=[AbaqusFolder{3}...
'job=',Jobname_second,' ',cpunumber,' int memory="90 %" output_precision=full double=both'];
        [status1 result1] = dos(abaqus, '-echo');
    end

str = sprintf('***************** Finish FEA of Individual %d ***************',ind);
disp(str);

%%%%%%%%%%%%%%%%%%%%%%%%%%%%%%%%%%%%%%%%%%%%%%%%%%%%%%%%%%%%%%%%
% Function for reading data from odb files
function Datastatus=RunAbaqusData_nonlinear(AbaqusFolder)
disp('************* Reading Data *************')

[status result] = dos(AbaqusFolder{1}, '-echo');
[status result] = dos(AbaqusFolder{2}, '-echo');
abaqus=[AbaqusFolder{3} 'cae noGUI=Run_abaqusData_nonlinear.py'];

[status1 result1] = dos(abaqus, '-echo');
disp('************* Finish Reading Data *************')
Datastatus=1;
```

Appendix C

Python Interface for Optimization Program

This appendix provides the details of the Python scripts used in the optimizations for generating geometry and for structural analyses by Abaqus.

C.1 Main Functions for Generating Geometry in Rhino 3D

```
import rhinoscriptsyntax as rs
import time
import math

rs.Command("_-SelAll")
rs.Command("_-Delete")
tol=rs.UnitAbsoluteTolerance(0.00000000001)
##### Function to read coordinates
def nodepoints(nodeFile):
    def node(text):
        items = text.strip("()\n").split(",")
        x = float(items[0])
        y = float(items[1])
        z = float(items[2])
        return x, y, z
    node_p = [node(line) for line in nodeFile]
    return node_p
###### Main function for NURBS interpolation and creating wavy geometry
# path: path to save igs files
```

```
# L: Shell length
# R=float(Rfile[0])
# Nxy: number of control points
# Nz: levels to extrude cylinders
# Nfile: Number of individuals

for ind in range(1,Nfile+1):
    Loftcurve=[]
    for i in range(1,Nz+1):
        nodename='Ind_'+str(ind)+'_Per_node_level_' + str(i) +'.txt'
        file = open(nodename, 'r')
        nodeFile = file.readlines()
        file.close()
        nodes=nodepoints(nodeFile)
        loft=rs.AddInterpCurve(nodes,degree=3, knotstyle=3)
        Loftcurve.append(loft)
        if i==Nz:
            loadlength=rs.CurveLength(loft)
            #print loadlength
            out_file=open('Ind_'+str(ind)+'_Per_edgelength.txt','w')
            out_file.write(str(loadlength))
            out_file.close()
    PerCyl=rs.AddLoftSrf(Loftcurve)
    rs.SelectObjects(PerCyl)
    rs.Command("_-Export " + path +"Ind_"+ str(ind)+ "_Shell_perfect" +".igs _Enter")
    rs.UnselectObjects(PerCyl)
```

C.2 Main Functions for Setting Abaqus Models

```
# Do not delete the following import lines
from abaqus import *
from abaqusConstants import *
from odbAccess import *
from sys import argv,exit
import testUtils
```

```
testUtils.setBackwardCompatibility()
from abaqusConstants import *
#import displayGroupOdbToolset as dgo
from textRepr import prettyPrint
from numpy.oldnumeric import array, Int32, Float64
import sketch
import part
import material
import section
import assembly
import step
import load
import regionToolset
import mesh
import job
import interaction
import connectorBehavior
import math
import sys
import os
import stat
import time
import shutil
#~~~~~~~~~~~~~~~~~~~~~~~~~~~~~~~~~~~~~~~~~~~~~~~~~~~~~~~~~~~~
# functions
def nodepoints(nodeFile):
    def node(text):
        items = text.strip("()\n").split(",")
        x = float(items[0])
        y = float(items[1])
        z = float(items[2])
        return x, y, z
    node_p = [node(line) for line in nodeFile]
    return node_p

def copyFile(filename1,filename2):
```

```
    print 'Copying ' + filename1 + ' to ' + filename2 + '...'
    shutil.copyfile(filename1, filename2)
    print 'done.'
def createModel(ABD_vector,Density,Meshsize,MeshFactor, Jobname1_per,ind,FOLDER):
    myModel = mdb.Model(name='Model-1')
    a = myModel.rootAssembly
    ### Create geometry
    shellname=FOLDER+'Ind_'+str(ind)+'_Shell_perfect.igs'
    shellfile=mdb.openIges(shellname, msbo=False, trimCurve=DEFAULT,
        topology=SHELL, scaleFromFile=OFF)
    myshell=myModel.PartFromGeometryFile(name='myshell', geometryFile=shellfile,
        combine=False, stitchAfterCombine=False, stitchTolerance=1.0,
        dimensionality=THREE_D, type=DEFORMABLE_BODY, topology=SHELL,
        convertToAnalytical=1, stitchEdges=1)
    myShellInstance=a.Instance(name='ShellInstance', part=myshell, dependent=ON)
    ### Create material
    ### Create & Assign Shell Section
    myModel.GeneralStiffnessSection(name='Section-1',
        referenceTemperature=None, stiffnessMatrix=(ABD_vector), applyThermalStress=0,
        poissonDefinition=DEFAULT, useDensity=ON, density=Density)
    # Assign section
    f = myshell.faces
    region = regionToolset.Region(faces=f)
    myshell.SectionAssignment(region=region, sectionName='Section-1', offset=0.0,
        offsetType=MIDDLE_SURFACE, offsetField='',
        thicknessAssignment=FROM_SECTION)
    # Orientation
    coord=myshell.DatumCsysByThreePoints(name='Datum csys-1', coordSysType=CYLINDRICAL,
        origin=(0.0, 0.0, 0.0), point1=(1.0, 0.0, 0.0), point2=(0.0, 1.0, 0.0))
    region = regionToolset.Region(faces=f)
    orientation = myshell.datums[coord.id]
    myshell.MaterialOrientation(region=region,
        orientationType=SYSTEM, axis=AXIS_2, localCsys=orientation,
        fieldName='', additionalRotationType=ROTATION_NONE, angle=0.0,
        additionalRotationField='')
    ### Create Mesh
```

```
    myshell.seedPart(size=Meshsize, deviationFactor=MeshFactor)
    elemType1 = mesh.ElemType(elemCode=S4, elemLibrary=STANDARD,
        secondOrderAccuracy=OFF, hourglassControl=DEFAULT)
    elemType2 = mesh.ElemType(elemCode=S3, elemLibrary=STANDARD,
        secondOrderAccuracy=OFF)
    pickedRegions =(myshell.faces, )
    myshell.setElementType(regions=pickedRegions, elemTypes=(elemType1, elemType2))
    myshell.generateMesh()
    myModel2 = mdb.Model(name='Model-2', objectToCopy=mdb.models['Model-1'])
    myModel3 = mdb.Model(name='Model-3', objectToCopy=mdb.models['Model-1'])
    Models=[myModel,myModel2,myModel3]
    return Models
#~~~~~~~~~~~~~~~~~~~~~~~~~~~~~~~~~~~~~~~~~~~~~~~~~~~~~~~~~~~~~~~~~~~~~~~~
def createBuckle(myModel,F,L,R,ind):
    # Create Step
    myModel.BuckleStep(name='Step-1', previous='Initial', numEigen=5,
        eigensolver=LANCZOS, minEigen=0.0, blockSize=DEFAULT,
        maxBlocks=DEFAULT)
    ### Create loads and bc
    file = open('Ind_'+str(ind)+'_Per_edgelength.txt', 'r')
    elfile = file.readlines()
    file.close()
    linelength=float(elfile[0])
    l_load=F/linelength

    a = myModel.rootAssembly
    mypartinstance=a.instances['ShellInstance']
    edges = mypartinstance.edges
    faces = mypartinstance.faces

    file = open('Nz.txt', 'r')
    Nzfile = file.readlines()
    file.close()
    Nz=int(Nzfile[0])

    nodename='Ind_'+str(ind)+'_Per_node_level_' + str(Nz) +'.txt'
```

```
file = open(nodename, 'r')
nodeFile = file.readlines()
file.close()
nodes=nodepoints(nodeFile)

edge1_1 = edges.findAt((nodes[1],)) # random point at edges
edge1_2 = edges.findAt((nodes[3],))
if edge1_1[0].index==edge1_2[0].index:
    regionload = regionToolset.Region(side1Edges=edge1_1)
else:
    edge1_3 = edges.findAt((nodes[5],))
    regionload = regionToolset.Region(side1Edges=edge1_3)

myModel.ShellEdgeLoad(name='Load-1', createStepName='Step-1',
    region=regionload, magnitude=l_load, distributionType=UNIFORM, field='',
    localCsys=None)
# Create BC
nodename='Ind_'+str(ind)+'_Per_node_level_' + str(1) +'.txt'
file = open(nodename, 'r')
nodeFile = file.readlines()
file.close()
nodes=nodepoints(nodeFile)

edge2_1 = edges.findAt((nodes[1],)) # random point at edges
edge2_2 = edges.findAt((nodes[3],))
if edge2_1[0].index==edge2_2[0].index:
    regionbc1 = regionToolset.Region(edges=edge2_1)
else:
    edge2_3 = edges.findAt((nodes[5],))
    regionbc1 = regionToolset.Region(edges=edge2_3)

myModel.DisplacementBC(name='BC-1', createStepName='Step-1',
    region=regionbc1, u1=0.0, u2=0.0, u3=0.0, ur1=0, ur2=0, ur3=0,
    amplitude=UNSET, fixed=OFF, distributionType=UNIFORM, fieldName='', localCsys=None)

nodename='Ind_'+str(ind)+'_Per_node_level_' + str(Nz) +'.txt'
```

```
    file = open(nodename, 'r')
    nodeFile = file.readlines()
    file.close()
    nodes=nodepoints(nodeFile)

    edge3_1 = edges.findAt((nodes[1],)) # random point at edges
    edge3_2 = edges.findAt((nodes[3],))
    if edge3_1[0].index==edge3_2[0].index:
        regionbc2 = regionToolset.Region(edges=edge3_1)
    else:
        edge3_3 = edges.findAt((nodes[5],))
        regionbc2 = regionToolset.Region(edges=edge3_3)

    myModel.DisplacementBC(name='BC-2', createStepName='Step-1',
        region=regionbc2, u1=0.0, u2=0.0, u3=UNSET, ur1=0, ur2=0, ur3=0,
        amplitude=UNSET, fixed=OFF, distributionType=UNIFORM, fieldName='',
        localCsys=None)
    # Output Variables
    myModel.FieldOutputRequest(name='F-Output-1',
            createStepName='Step-1', variables=('SE', 'SF' ,'U', 'RF', 'S'))

    return myModel

#~~~~~~~~~~~~~~~~~~~~~~~~~~~~~~~~~~~~~~~~~~~~~~~~~~~~~~~~~~~~~~~~~~~~

def createNonlinear_buckle(myModel,F,L,R,ind):
    # Create Step
    myModel.StaticRiksStep(name='Step-1', previous='Initial', maxLPF=500.0,maxNumInc=50, nlgeom=ON)
    ### Create loads and bc
    file = open('Ind_'+str(ind)+'_Per_edgelength.txt', 'r')
    elfile = file.readlines()
    file.close()
    linelength=float(elfile[0])
    l_load=F/linelength
```

```
a = myModel.rootAssembly
mypartinstance=a.instances['ShellInstance']
edges = mypartinstance.edges
faces = mypartinstance.faces

file = open('Nz.txt', 'r')
Nzfile = file.readlines()
file.close()
Nz=int(Nzfile[0])

nodename='Ind_'+str(ind)+'_Per_node_level_' + str(Nz) +'.txt'

file = open(nodename, 'r')
nodeFile = file.readlines()
file.close()
nodes=nodepoints(nodeFile)

edge1_1 = edges.findAt((nodes[1],)) # random point at edges
edge1_2 = edges.findAt((nodes[3],))
if edge1_1[0].index==edge1_2[0].index:
    regionload = regionToolset.Region(side1Edges=edge1_1)
else:
    edge1_3 = edges.findAt((nodes[5],))
    regionload = regionToolset.Region(side1Edges=edge1_3)

myModel.ShellEdgeLoad(name='Load-1', createStepName='Step-1',
    region=regionload, magnitude=l_load, distributionType=UNIFORM, field='',
    localCsys=None)

# Create BC

nodename='Ind_'+str(ind)+'_Per_node_level_' + str(1) +'.txt'
file = open(nodename, 'r')
nodeFile = file.readlines()
file.close()
nodes=nodepoints(nodeFile)
```

```
    edge2_1 = edges.findAt((nodes[1],)) # random point at edges
    edge2_2 = edges.findAt((nodes[3],))
    if edge2_1[0].index==edge2_2[0].index:
        regionbc1 = regionToolset.Region(edges=edge2_1)
    else:
        edge2_3 = edges.findAt((nodes[5],))
        regionbc1 = regionToolset.Region(edges=edge2_3)
    myModel.DisplacementBC(name='BC-1', createStepName='Step-1',
        region=regionbc1, u1=0.0, u2=0.0, u3=0.0, ur1=0, ur2=0, ur3=0,
        amplitude=UNSET, fixed=OFF, distributionType=UNIFORM, fieldName='', localCsys=None)

    nodename='Ind_'+str(ind)+'_Per_node_level_' + str(Nz) +'.txt'

    file = open(nodename, 'r')
    nodeFile = file.readlines()
    file.close()
    nodes=nodepoints(nodeFile)

    edge3_1 = edges.findAt((nodes[1],)) # random point at edges
    edge3_2 = edges.findAt((nodes[3],))
    if edge3_1[0].index==edge3_2[0].index:
        regionbc2 = regionToolset.Region(edges=edge3_1)
    else:
        edge3_3 = edges.findAt((nodes[5],))
        regionbc2 = regionToolset.Region(edges=edge3_3)
    myModel.DisplacementBC(name='BC-2', createStepName='Step-1',
        region=regionbc2, u1=0.0, u2=0.0, u3=UNSET, ur1=0, ur2=0, ur3=0,
        amplitude=UNSET, fixed=OFF, distributionType=UNIFORM, fieldName='',
        localCsys=None)
    # Output Variables
    myModel.FieldOutputRequest
    (name='F-Output-1', createStepName='Step-1', variables=('SE', 'SF' ,'U', 'RF', 'S'))

    return myModel
#~~~~~~~~~~~~~~~~~~~~~~~~~~~~~~~~~~~~~~~~~~~~~~~~~~~~~~~~~~~~~~~~
```

```
def analyzeBuckle(myModel,Jobname,NumCpu):
  # Create Job
  Job1 =mdb.Job(name=Jobname, model=myModel, description='', type=ANALYSIS,
        atTime=None, waitMinutes=0, waitHours=0, queue=None, memory=90,
        memoryUnits=PERCENTAGE, getMemoryFromAnalysis=True,
        explicitPrecision=SINGLE, nodalOutputPrecision=FULL, echoPrint=OFF,
        modelPrint=OFF, contactPrint=OFF, historyPrint=OFF, userSubroutine='',
        scratch='', multiprocessingMode=DEFAULT, numCpus=NumCpu, numDomains=NumCpu)

  mdb.jobs[Jobname].writeInput(consistencyChecking=OFF)
#~~~~~~~~~~~~~~~~~~~~~~~~~~~~~~~~~~~~~~~~~~~~~~~~~~~~~~~~~~~~~~~~
def analyzeNonlinear_buckle(myModel,Jobname,NumCpu):
  # Create Job
  Job1 =mdb.Job(name=Jobname, model=myModel, description='', type=ANALYSIS,
        atTime=None, waitMinutes=0, waitHours=0, queue=None, memory=90,
        memoryUnits=PERCENTAGE, getMemoryFromAnalysis=True,
        explicitPrecision=SINGLE, nodalOutputPrecision=SINGLE, echoPrint=OFF,
        modelPrint=OFF, contactPrint=OFF, historyPrint=OFF, userSubroutine='',
        scratch='', multiprocessingMode=DEFAULT, numCpus=NumCpu, numDomains=NumCpu)

  mdb.jobs[Jobname].writeInput(consistencyChecking=OFF)
#~~~~~~~~~~~~~~~~~~~~~~~~~~~~~~~~~~~~~~~~~~~~~~~~~~~~~~~~~~~~~~~~

def createInpfiles_Imperfect(Jobname_source,Jobname_imp,ind):

  Inp_source=Jobname_source+'.inp'
  file = open(Inp_source, 'r')
  sourceFile = file.readlines()
  file.close()

  Inpname_imp_pos=Jobname_imp[0]+'.inp'
  Inpname_imp_neg=Jobname_imp[1]+'.inp'

  # clear files
  Inp_impFile_pos = open(Inpname_imp_pos,'w')
  Inp_impFile_pos.close()
```

```
Inp_impFile_neg = open(Inpname_imp_neg,'w')
Inp_impFile_neg.close()

# create files
Inp_impFile_pos = open(Inpname_imp_pos,'w')
Inp_impFile_neg = open(Inpname_imp_neg,'w')
Inp_impFile_pos_Filelist=[]
Inp_impFile_neg_Filelist=[]


Ptname_pos='Ind_'+str(ind)+'_perturbation_pos.txt'
file = open(Ptname_pos, 'r')
nodeFile = file.readlines()
file.close()
perturbation_pos=nodepoints(nodeFile)


Ptname_neg='Ind_'+str(ind)+'_perturbation_neg.txt'
file = open(Ptname_neg, 'r')
nodeFile = file.readlines()
file.close()
perturbation_neg=nodepoints(nodeFile)

changeind=0
addpertstatus=-1

for i in range(0,len(sourceFile)):


    if cmp(sourceFile[i],'*Node'+'\n')==0 or cmp(sourceFile[i],'*Element, type=S4'+'\n')==0:
        addpertstatus=-1*addpertstatus

    if cmp(sourceFile[i],'*Node'+'\n')!=0 and addpertstatus==1:

        items = sourceFile[i].strip("()\n").split(",")
        numb= int(items[0])
```

```
            x = float(items[1])
            y = float(items[2])
            z = float(items[3])

            dataline_pos=str(numb)+','+str(x+perturbation_pos[changeind][0])+
            ','+str(y+perturbation_pos[changeind][1])+','+str(z+perturbation_pos[changeind][2])+'\n'
            dataline_neg=str(numb)+','+str(x+perturbation_neg[changeind][0])+
            ','+str(y+perturbation_neg[changeind][1])+','+str(z+perturbation_neg[changeind][2])+'\n'

            Inp_impFile_pos_Filelist.append(dataline_pos)
            Inp_impFile_neg_Filelist.append(dataline_neg)

            changeind=changeind+1

        else:

            Inp_impFile_pos_Filelist.append(sourceFile[i])
            Inp_impFile_neg_Filelist.append(sourceFile[i])

    Inp_impFile_pos.writelines(Inp_impFile_pos_Filelist)
    Inp_impFile_neg.writelines(Inp_impFile_neg_Filelist)
    Inp_impFile_pos.close()
    Inp_impFile_neg.close()
```

C.3 Main Functions for Reading Data from Abaqus Odb Files

```
# Do not delete the following import lines
from abaqus import *
from abaqusConstants import *
from odbAccess import *
from sys import argv,exit
import testUtils
testUtils.setBackwardCompatibility()
from abaqusConstants import *
import sketch
```

```
import part
import material
import section
import assembly
import step
import load
import regionToolset
import mesh
import job
import interaction
import connectorBehavior

import displayGroupMdbToolset as dgm
import visualization
import xyPlot
import displayGroupOdbToolset as dgo

import math
import sys
import os
import stat
import time
import shutil
import numpy as np
# Generate output data
#~~~~~~~~~~~~~~~~~~~~~~~~~~~~~~~~~~~~~~~~~~~~~~~~~~~~~~~~~~~~~~~~
def copyFile(filename1,filename2):
    print 'Copying ' + filename1 + ' to ' + filename2 + '...'
    shutil.copyfile(filename1, filename2)
    print 'done.'
def nodepoints(nodeFile):
    def node(text):
        items = text.strip("()\n").split(",")
        x = float(items[0])
        y = float(items[1])
        z = float(items[2])
```

```
        return x, y, z
    node_p = [node(line) for line in nodeFile]
    return node_p
def geteigenvalue(odbName):
    odb = openOdb(odbName+'.odb')
    step = odb.steps['Step-1']
    eigname_des='eigval_des_'+odbName+'.txt'

    out_file=open(eigname_des,'w')
    out_file.write(str(step.frames[1].description))
    out_file.close()

    out_file=open(eigname_des,'r')
    mode = out_file.readlines()
    out_file.close()
    mode_split=mode[0].split()
    eigval_cr=mode_split[-1]

    eigname='eigval_'+odbName+'.txt'

    out_file=open(eigname,'w')
    out_file.write(str(eigval_cr))
    out_file.close()
    odb.close()
    print 'First eigenvalue is', eigval_cr

def getPerturbation(odbName,A,ind):

    odb = openOdb(odbName+'.odb')
    Assembly = odb.rootAssembly
    instance = Assembly.instances['SHELLINSTANCE']

    # Displacement
    displacement = []
    dispmegn=[]
    pertub_u=[]
```

```
pertub_v=[]
displacement_append = displacement.append
Displacement = 'U'
isDisplacementPresent = 0
step = odb.steps['Step-1']

allFields = step.frames[1].fieldOutputs

if (allFields.has_key(Displacement)):
    isDisplacementPresent = 1
    dispSet = allFields[Displacement]
    for value in dispSet.values:
        u1 = value.dataDouble[0]
        u2 = value.dataDouble[1]
        u3 = 0
        pertub_u.append(u1)
        pertub_v.append(u2)
        displacement_append(u1)
        displacement_append(u2)
        dispmegn.append(sqrt(u1**2+u2**2))

odb.close()
max_dis=max(dispmegn)
print 'Maximum displacement is:', max_dis

scale= A/max_dis

purtline_pos=[]
purtline_neg=[]
for pertind in range(0,len(pertub_u)):
  dataline_pos=str(scale*pertub_u[pertind])+','+str(scale*pertub_v[pertind])+',0'+'\n'
  purtline_pos.append(dataline_pos)
  dataline_neg=str(-scale*pertub_u[pertind])+','+str(-scale*pertub_v[pertind])+',0'+'\n'
  purtline_neg.append(dataline_neg)
```

```
    Ptname_pos='Ind_'+str(ind)+'_perturbation_pos.txt'
    purtFile_pos = open(Ptname_pos,'w')
    purtFile_pos.writelines(purtline_pos)
    purtFile_pos.close()

    Ptname_neg='Ind_'+str(ind)+'_perturbation_neg.txt'
    purtFile_neg = open(Ptname_neg,'w')
    purtFile_neg.writelines(purtline_neg)
    purtFile_neg.close()

def Critical_load_nonlinear(odbName,direction,L,R):
    odb = openOdb(odbName+'.odb')
    step = odb.steps['Step-1']

    Assembly = odb.rootAssembly
    instance = Assembly.instances['SHELLINSTANCE']

    # Create force region Nodeset
    nodelabels = ()
    error=1E-5
    for node in instance.nodes:
      coords = node.coordinates
      if  abs(L-coords[2]) < error+0.001:
        nodelabels = nodelabels + (node.label,)
        break
    print  odbName
    #print    Assembly.nodeSets
    allNodeSets=Assembly.nodeSets

    if not allNodeSets.has_key('EDGENODES'):
        Assembly.NodeSetFromNodeLabels(nodeLabels=(('SHELLINSTANCE', nodelabels),), name='EDGENODES')
        Assembly.nodeSets['EDGENODES']

    displacement = []
    displacement_append = displacement.append
    critical_load=-1
```

```
recordstatus=1
LPFname='LPF_'+odbName+'.txt'
out_file=open(LPFname,'w')
out_file.close()
xyLPF = xyPlot.XYDataFromHistory(odb=odb,
outputVariableName='Load proportionality factor: LPF for Whole Model', steps=('Step-1', ) ,)
for i in range(0,len(step.frames)):
  Displacement = 'U'
  allFields = step.frames[i].fieldOutputs
  dispSet = allFields[Displacement]
  dispSet = dispSet.getSubset(region=Assembly.nodeSets['EDGENODES'])
  value=dispSet.values
  #u=value.data[direction]
  u=value[0].dataDouble[direction]
  displacement_append(u)

  out_file=open(LPFname,'a')
  data2=xyLPF[i][1]
  if data2<0:
    break

  data1=abs(u)
  out_file.write(str(data1)+','+str(data2)+'\n')
  out_file.close()
  if critical_load<=  data2 and recordstatus==1:
    critical_load=data2
  else:
    recordstatus=-1

eigname='eigval_'+odbName+'.txt'
out_file=open(eigname,'w')
out_file.write(str(critical_load))
out_file.close()
odb.close()
```